FLORIDA STATE UNIVERSITY

COLLEGE OF ARTS AND SCIENCES

UNDERSTANDING THE EVOLUTION OF CARRIERS IN TIN CADMIUM OXIDE TERNARY PLASMONIC NANOCRYSTALS

By

RAUL EDUARDO ORTEGA

A Dissertation submitted to the
Department of Chemistry & Biochemistry
in partial fulfillment of the
requirements for the degree of
Doctor of Philosophy

2024

Raul E. Ortega defended this dissertation on July 1, 2024.
The members of the supervisory committee were:

Geoffrey F. Strouse
Professor Directing Dissertation

William Oates
University Representative

Kenneth Hanson
Committee Member

Robert W. Schurko
Committee Member

The Graduate School has verified and approved the above-named committee members, and certifies that the dissertation has been approved in accordance with university requirements.

This dissertation is dedicated to curiosity, imagination, and hard work. Without these qualities, we'd be unable to become our best selves.

"The most important step a man can take. It's not the first one, is it?
It's the next one. Always the next step, Dalinar."
— Brandon Sanderson, Oathbringer

ACKNOWLEDGMENTS

Foremost, I would like to express my deepest gratitude to my advisor, **Dr. Geoffrey Strouse**, for his unwavering belief in me and for constantly pushing me to my limits. Thank you for not giving up on me throughout the years. One of my favorite parts of graduate school was our discussions, which often led to multiple Google and Bing searches, ending up with information far afield from where we started. I have learned so much from you, and I hope to continue learning in future endeavors. I would also like to extend my heartfelt thanks to **Dr. Robert Schurko** for graciously joining my committee after Dr. Albert Stiegman's retirement. Your willingness to step in and your collaboration in NMR, along with other interactions, have been a pleasure and immensely valuable. My sincere appreciation goes to **Dr. Kenneth Hanson** for being a constant source of support throughout the years. I deeply respect your work both as a scientist and a science communicator. Your Twitch science/gaming streams are an innovative medium for science advocacy, demonstrating that there is always room for fun in graduate school, even for faculty members. To my outside committee member, **Dr. William Oates**, thank you. I wish we could have spent more time discussing science, but I will always cherish our initial discussions on optical and pressure work.

I would also like to acknowledge the friends I made in Tallahassee, both inside and outside the graduate program. They made my time here much more enjoyable, and I am deeply thankful for each and every one of you. In the chemistry department, special thanks to the members of the Schurko group: **Dr. Adam Altenholf** (Canadian Jesus), **Dr. Austin Peach** (Peach), **James Kimball** (Dirty Jimmy), **Robert Smith** (GoT Guru), and **Carl Fleischer** (Goat Enjoyer). Your camaraderie and support have been wonderful. A warm thank you to my friends in the Hanson group**: Dr. Ashley Arcidiacono** for always being helpful and fun to be around**, Dr. Erica Knorr** and **Gracie McLeod** for the enjoyable times playing DnD, and to the friends in the Kennemur group, **Dr. Brianna Coia** for her vibrant personality, and **Dr. Courtney Leo** (Balls) for her sweetness. I would also like to thank **Rajarshi Acharya** for always being a welcoming and cheerful presence in the hallways.

Acknowledging the past and present members of the Strouse group, I have learned something valuable from each of you. Special thanks to **Dr. David Hardy** for showing me the ropes, **Dr. Rodney Tigaa** for his mentorship and unwavering support, **Dr. Carl Conti III**

(Carlito) for his scientific insights, and **Dr. Edward Nguyen** for his challenges and support which helped me grow. A heartfelt thank you to **Dr. Jason Kuszynski** for always being there for me as a fellow graduate student and friend. Our discussions during the day and explorations at the swamp were unforgettable. To **Dr. Isabella Bertinni**, thank you for being my companion through our struggles. Your presence has been a constant support. Special mention to the younger members of the Strouse group: **Sarah Bennett**, thank you for being so kind and for your growth as a scientist; **Ali Pazoki**, for your hard work and determination; **Andrew Cantrell**, I'm glad you chose FSU and wish you the best in your future endeavors; and **Emily Cook**, best of luck with your new journey, and remember to always believe in your ninja way. I want to also thank **Catherine Fabiano** for being such a cheerful person and a joy to have around, wish you the best on your next adventure. I would also like to acknowledge the undergraduate students I had the pleasure of working with in the Strouse group: **Lennies Kamau**, **Jonathan Rider**, **Samantha Bell**, and REU student **Corbin Frisvold**. Your dedication and curiosity are inspiring. You are all excellent and curious individuals, and I am sure you will accomplish great things. Lastly, I would like to thank **Dr. Xinsong Lin** and **Dr. Raaj Winfred** for their invaluable assistance with training and troubleshooting departmental instruments, and **Lori Henley** in the Chemistry Department for her unwavering support and ensuring we stayed on track. I want to give special thanks to **Dr. Banghao Chen**, for helping me with solid-state NMR and the time we spent working together.

I would like to extend my heartfelt gratitude to the friends I made in Tallahassee. The countless hours we spent playing various card games were some of the most enjoyable moments of my time here. As an avid card game enthusiast, I cherished every opportunity to play, share, and laugh with you all. To my friends outside of Tallahassee: **Aldo Garcia**, **Blair Hunter**, **Clinton Parmer**, **Daniel Tuzzolino**, **Eric Turner**, **Logan Stinson**, **Mi Windus**, **Oliver Hinton**, and **Tyler Stokely**, thank you for your friendship and the wonderful memories. To my friends in Tallahassee, with whom I spent most of my time: **Joel Patton**, **Andrew Roberts**, **Taylor Mauck**, **Jean Magueur**, **Marcus Lawson**, **Cody Rising**, **Jodie Watkins**, **Wesley Moir**, and **Michael James**, your companionship made my time here truly special. A special thank you to my friend **Jeremy Kuhne** for all the hours we spent together at the Villa. Your friendship and the moments we shared are deeply appreciated.

To my FAU peers, I would like to express my deepest gratitude to my undergraduate professor and PI, **Dr. Daniel T. de Lill**, for introducing me to the world of science, undergraduate research, and lanthanide chemistry. He has been an inspiration to all the undergraduate students he mentored, and he holds a special place in my heart. Without his guidance, I wouldn't have discovered my passion for research, which motivated me to pursue a Ph.D. in chemistry. I also extend my heartfelt thanks to my graduate mentor during my time in the de Lill group, **Dr. Jeffrey D. Einkauf**. His passion and patience with undergraduate students were truly remarkable. I have never met someone with such a strong work ethic and focus on science and research. I would like to thank all my friends and colleagues I made during my time at FAU: **Devin Dykes**, **Kathryn Pitton**, **Kelly Rue**, **Elyse Jutte**, and **Heather Ten Hoeve**. A special thanks to **Ryan Crichton** and **Yiro Shimabukuro** (Blossom Kitchen Factory) for their unwavering friendship and support throughout the years.

I would like to give a special thanks to Professor **Steve Brahlek** for his mentorship and contributions to the Honors College at PBSC. I spent many hours in his office discussing assignments or talking about various topics. Thank you for explaining to me what "yay big" means. As a foreigner, I was amazed that such an expression exists in English. I would also like to express my heartfelt gratitude to all the friends I made during my time at PBSC. They made my time there incredibly enjoyable and fun. My friends **Maria Ramos**, **Dominique Notare**, **Shawn Phillips**, **Liz Nuynh**, and **Amanda Alves**, your companionship was invaluable. A special thanks to **Rachel Wong** for being such an amazing friend while we studied and worked at PBSC.

I would like to give special thanks to my high school chemistry professor, **Miss Kenyon**. Without her class, I don't think I would have developed such a deep love for chemistry. I will never forget the laboratory class where we made S'mores to determine the limiting reagent in their production. I was convinced that chocolate should be the limiting reagent, but the data revealed that the crackers were the limiting reagent. I learned a valuable lesson that I still remember to this day. Plus, the S'mores were delicious! I would also like to express my gratitude to the good friends I made along the way during high school. Thank you to my dear friends **Luis Perez**, **Alvaro Lopez**, **Angelica Ochrymowicz**, **Danitza Parada**, and **Tatiana Parra** for sharing so many fun times with me during this period. Thank you very much to each and every one of you.

Thank you to all my friends in the Dominican Republic. There are so many of you that I have kept in contact with throughout the years through WhatsApp. A special thank you to some of my closest friends since childhood: **Domingo Arias**, **Andres Hipolito**, **Erick Reynoso**, **William Acosta**, **Moises Aybar**, and **Javier Mota**. I couldn't be here without you, and I am lucky to have met you. Although I didn't meet them during my childhood, I want to say thank you to **Antonio Melo** and **Rinny Vásquez**. I want to give a heartfelt thank you to **Ivan Reyes**, **Roberto Lorenzo**, **Eric Lorenzo**, and **Erik Perez** in the cousin group chat for laughing, discussing, sharing memes, and just being burlated goofballs. Thank you to all my family in the Dominican Republic. I love you all, and I am grateful to every single one of you. Thank you for supporting me through all the years, and I miss you. A special thank you to my dad **Elpidio Ortega**, my sister **Miranda Ortega**, my **grandma (Vivi)**, my grandma **Fatima Gomez**, my aunt **Lilliam Ortega**, and my uncle **Elvis Ramirez** for all the love and support throughout the years.

I want to say thank you to my beautiful girlfriend, **Kristyn Ferguson**. I love you and thank you for supporting me through so many tough times during these past four years. Thank you to my family that I love and spend most of my time with. My stepdad **Walter Rossetto**, you are a great man, and I am happy that you are part of my life. My little sister **Gabriella Rossetto** (Cookie), for being the sweetest and smartest cookie in the jar. Finally, I want to give huge thanks to my mom **Wanda Rossetto**. Without her support, I wouldn't be here today. I am greatly indebted to her, and I love her with all my heart.

TABLE OF CONTENTS

LIST OF TABLES

LIST OF FIGURES

LIST OF ACRONYMS

TCO	transparent conductive oxide
LSPR	localized surface plasmon resonance
NC	nanocrystal
CTO	cadmium stannate
PSNCs	plasmonic semiconductor nanocrystals
SSNMR	solid-state nuclear magnetic resonance
KS	Knight shifts
Sn_{Cd}	Sn antisite
V_O	oxygen vacancy
M'_M	antisite defect
pXRD	powder X-ray diffraction
EPR	electron paramagnetic resonance
fs	femtosecond
TA	transient absorption
V_M	metal vacancy
M_i	interstitial metal
HOMO	highest occupied molecular orbital
LUMO	lowest occupied molecular orbital
3D	3-dimensional
VB	valence band
CB	conduction band
K	Kelvin
E_g	bandgap
SC	semiconductor
E_F	Fermi level
e^-	electron
h^+	hole
m^*	effective mass
DOS	density of states
$\boldsymbol{k}$	wavevector
$\hbar$	reduced Planck constant $6.582\,119\ldots \times 10^{-16}$ eV s
$E(\boldsymbol{k})$	energy of carriers as a function of $\boldsymbol{k}$
μ	carrier mobility
O_h	octahedral
T_d	tetrahedral
NP	nanoparticle
SA/V	surface area-to-volume ratio
QD	quantum dot
ε	permittivity
E	electric field
ε_r	dielectric constant
SPR	surface plasmon resonance
$\epsilon'(\omega)$	real part dielectric constant

$\epsilon''(\omega)$	imaginary part dielectric constant
ω	frequency of light
Ln	lanthanide
SERS	surface enhanced Raman scattering
n	carrier density
e	charge of the carrier
ε_0	permittivity of free space
ω_{LSPR}	plasmon frequency
ω_p	plasma frequency
ω_∞	high frequency dielectric constant
UV	ultraviolet
Vis	visible
IR	infrared
A	absorbance
α	molar extinction coefficient
l	optical path length
c	concentration of particles
FTIR	Fourier transfer infrared
B_0	magnetic field
ΔE	energy difference
γ	gyromagnetic ratio
RF	radio frequency
FID	free induction decay
PPM	parts per million
MAS	magic-angle spinning
T_1	spin–lattice relaxation time
T_2	spin–spin relaxation time
CS	chemical shift
T	temperature
k_B	Boltzman constant
γ_n	nuclear gyromagnetic ratio
CPMG	Carr-Purcell Meiboom-Gill
FS	frequency-swept
WURST	wideband uniform-rate smooth truncation
λ	wavelength
MO_x	metal oxide
DFT	density functional theory
MCD	magnetic circular dichroism
$NOBF_4$	nitrosonium tetraluoroborate
SDA	simplified Drude approximation
3-SDA	3-mode simplified Drude model
SXDA	extended Drude approximation
GPC	gel permeation column
XPS	x-ray photoelectron spectroscopy
HAADF	high-angle annular dark-field
STEM	scanning transmission electron microscopy

Q-factor	quality factor
E_z	Zeeman splitting energy
EELS	electron energy loss spectroscopy
Γ_L	low frequency damping
Γ_H	high frequency damping
Γ_X	crossover region
Γ_W	crossover width
χ_s	electron spin susceptibility
el-ph	electron-phonon
ph-ph	phonon-phonon

ABSTRACT

This dissertation focuses on understanding the plasmonic properties of novel transparent conductive oxides (TCOs), more specifically the family of binary and ternary Sn-Cd-O containing materials. The first chapter introduces the background, fundamental knowledge, concepts, and techniques necessary for the understanding and study of the localized surface plasmon resonances (LSPRs) in nanocrystals (NCs).

The second chapter introduces the novel synthesis of a well-faceted cadmium stannate (CTO) inverse spinel plasmonic semiconductor nanocrystals (PSNCs). The use of Sn(II) in the colloidal reaction for CTO results in reproducible octahedral PSNCs. Correlating extinction spectra with magnetic circular dichroism allows the calculation of carrier density and carrier effective mass. ^{113}Cd and ^{119}Sn solid-state NMR (SSNMR) experiments show clear evidence of metallic-like carriers in CTO NCs based upon the observation of Knight shifts (KS). These data suggest that carrier formation in CTO arises from Sn antisite occupation of octahedral Cd sites (Sn_{Cd}). From a broader perspective, the results point to wide band gap spinels as being an important but understudied class of plasmonic PSNCs.

The third chapter studies the evolution of the carrier properties in the Sn-Cd-O system. The defect evolution from an oxygen vacancy (V_O) to an antisite (M'_M) is underexplored and the nature of the optical properties from different types of defects is not fully understood. This Sn-Cd-O family provides the perfect system to study these changes. The evolution of the structure and optoelectronic properties is investigated through powder x-ray diffraction (pXRD), NMR, and electron paramagnetic resonance (EPR), and femtosecond (fs) transient absorption (TA).

The fourth chapter tries to understand the annealing effects on the plasmonic properties of CTO. Annealing is a physical process in which a material is heat up at a specific temperature for a certain amount of time to "anneal" crystallographic defects such as V_O, metal vancancies (V_M), and metal interstitials (M_i). This happens because atoms diffuse through the crystal during the annealing process, which allows for recrystallization of the crystal lattice into a more "perfect" configuration. Annealing as a technique has a rich history in metallurgy, solid state materials, and thin-film fields.

The fifth chapter explores the optical properties of CTO made from SnF_2 instead of $SnOAc_2$. By employing a tin(II) fluoride source instead of the acetate, there are significant

improvements to frequency of the LSPR, the Q-factor, NMR Knight-shift, and hot carrier dynamics of the final FCTO product. These observations demonstrate significant improvements to the optoelectronic properties by virtue of having an effective mass one order of magnitude lower than the one measured in CTO.

Finally, chapter 6 explores some of the future work and some of the relevant questions that are still of much interest to the plasmonic field. These topics present exciting opportunities for future students and researchers to explore.

CHAPTER 1

INTRODUCTION

1.1 Motivation for Transparent Conductive Oxides

Wide bandgap metal oxides (MO_x) have high carrier densities ($> 10^{19}$ cm^{-3}), transparency in the visible spectral region, and in an nanocrystal can possess a tunable localized surface plasmon resonance (LSPR) frequency.[1,2] Reflecting the plasmonic properties, many plasmonic semiconductor nanocrystals (PSNCs) have been investigated as alternatives to noble metals for photocatalysis,[3,4] chemical and biological detectors,[5,6] electrochromic windows,[7–9] and quantum computing.[10,11]Unlike noble metals,[12–14] MO_x PSNCs exhibit a tunable plasmon dependent on carrier density (Drude Model) when the carrier density surpasses the Mott metal-insulator threshold.[15–19] Surpassing the Mott threshold leads to population of delocalized electrons at or above the conduction band minimum.[20,21] Interest in PSNCs can be traced to an initial report of a plasmonic feature in n-type $Sn:In_2O_3$ nanocrystals,[22] leading to many subsequent publications rapid exploration of intrinsically and extrinsically doped PSNCs to establish a clear correlation for PSNC between the dopant and carrier mobility, particle size, plasmon frequency (ω_{LSPR}), and carrier density (n) being identified.[23–26]

1.2 Brief History of Transparent Conductive Oxides

Every technology around us relies on the discovery and understanding of fundamental physical and chemical principles. The discovery of transparent conductive oxides (TCOs) has led to development of optoelectronic devices (LEDs, detectors, and photovoltaic devices),[27] solar energy conversion (solar panels),[28] display technologies (cellphones/touch screens), and many other technologies that rely in coupling materials with high transparency and good electrical conductivity. Highly conductive materials such as gold, silver, or copper are opaque materials because high carrier (electrons in this case) concentrations lead to scattering centers that absorb or reflect light. As technology progressed through the 20th century, the motivation to couple materials that are both transparent, but also conductive, pushed chemistry research into the synthesis and discovery of new materials that possess these properties.

The work on what could be considered the "first" TCO was done by Dr. Karl Bädeker in 1907 where he reported the conductivity of oxidized Cd thin films transitioning into CdO.[29,30] In his work he observed that these films kept their transparency while still being conductive. The first step towards feasible TCOs was the discovery of SnO_2 as a TCO material with decent conductivity, transparency in the visible region, chemical stability, and wide-band gap limiting the number of optical processes.[31,32] Although promising, SnO_2 thin films properties were limited, which in the late 1940s and early 1950s incentivized the research to improve this material by doping Sb[33] or F[34] to improve conductivity while maintaining high transparency in the visible region. While SnO_2 was not yet considered a state-of-the-art material, its development led the way to keep improving and studying other TCO materials such as CdO[35,36] and ZnO.[37–39] This effort led to the breakthrough that happened in the 1970s where Sn (IV) doped In_2O_3 oxide (ITO) became the state-of-the-art TCOs, followed by an explosion of publications reporting the properties of ITO thin films.[40–42] Since then, ITO has become the staple TCO currently used in touch screens and cellphones.

While ITO has established itself as the industry standard, a plethora of other TCOs exist with high conductivity and transparency, have been overlooked or received insufficient attention in the field. An example is the recent rise in interest regarding Al(III) and Ga(III) doped ZnO[43–45] as a cheaper alternative to ITO, driven by increasing concerns over the availability and cost of In on the global stage. In addition, the plasmonic and nanoscale properties of these alternative TCOs remain relatively unexplored and poorly understood. The work presented here delves into the structure property relationship of plasmonic TCOs at the nanoscale and how they can be manipulated to further future and current technologies.

1.3 Band Theory of Solids

1.3.1 What is Band Theory?

When describing bonding and electronic transitions in molecules, it is advantageous to explain and describe these events in terms of molecular orbital theory. Where the highest occupied molecular orbital (HOMO) and lowest unoccupied molecular orbital (LUMO) levels play a key role in the understanding of photophysical events such as the absorption and emission of light. Band theory was developed to explain the electronic properties of solids, rather than

molecules, similar to how quantum mechanics was developed to explain the behavior observed in quantum confined materials that do not follow classical Newtonian physics.

In a crystalline solid, atoms are confined into lattices that form 3-dimensional (3D) networks. These atoms are so close to each other that their atomic orbitals start to overlap with one another. This overlap starts creating a "band", rather than discrete energy states. This new behavior is the reason why it is more useful to describe the behavior of charge carriers in terms of these bands rather than discrete energy levels.[46–48]

1.3.2 Metals, Insulators, and Semiconductors

The first two concepts to introduce are the conduction band and valance band (Figure 1). The valence band (VB) is the highest energy level where electrons are found at 0 K temperature. These electrons are within the material and are not very mobile, meaning that they do not contribute to the conductivity of the material. The conduction band (CB) is composed of higher energy states that are empty at 0 K. When electrons occupy the CB, they are highly mobile and are highly delocalized throughout the material, leading to electrical conductivity.

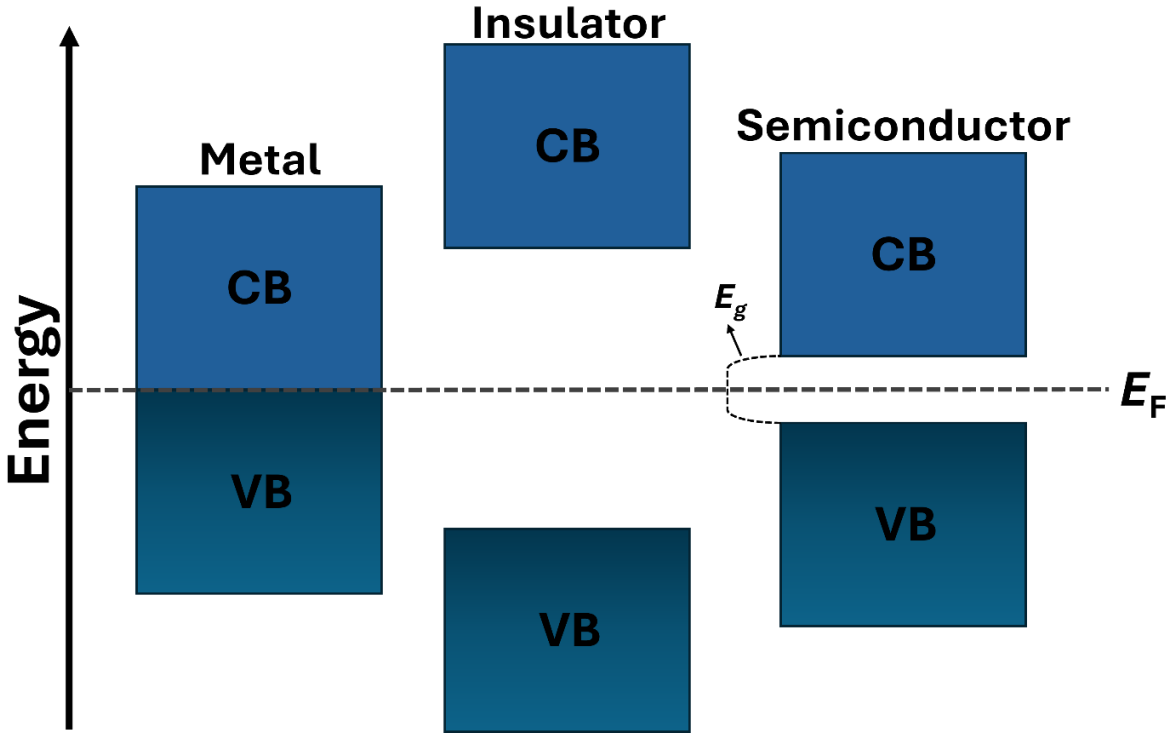

Figure 1. Representation of band diagrams for a metal, insulator, semiconductor, and the tentative position of the Fermi level (E_F). The bandgap (E_g) is shown to denote the separation between CB and VB.

The bandgap (E_g) of the material denotes the amount of energy that needs to be introduced into the system to promote and electron from the VB to the CB. The size of the E_g allows the material to be classified into three distinctive categories: metals, insulators, and semiconductors (SC). In a metal, there's no bandgap and the carriers are free to flow from the VB to the CB. In an insulator, the E_g is so large (> 4 eV) that the amount of energy required to promote an electron to the conduction band is not accessible through visible light (1.60 to 3.26 eV), therefore insulators tend to not conduct electricity. A SC lies somewhere in between the two where it behaves as an insulator, but can also act as a conductor if external energy is applied. A SC does have E_g much lower than an insulator (< 4 eV), but requires external stimuli, usually in the form of light, with enough energy to overcome the bandgap and promote an electron from the VB to the CB.[46–48]

1.3.3 The Fermi Level and Types of Semiconductors

Depending on where the Fermi level (E_F) resides in a SC, it is possible to have a n-type (negative/e^-) or p-type (positive/h^+) charge carriers (Figure 2). The E_F is an energy level where the probability of finding an electron is 50% at absolute zero, in other words, it represents the highest occupied energy level in a SC. In metals the E_F is found in the VB/CB continuum, while in undoped SCs is found somewhere within the E_g. In the case for a doped SC, the E_F can be controlled to reside within the CB or the VB, generating free charge carriers in the process.

As stated above, these charge carriers are quasi-particles that can be either electrons (e^-) or holes (h^+), each be having and having their own unique properties and behavior. Any defect that requires the crystal lattice to compensate charge imbalance will do so by introducing extra e^-, resulting in an n-type system, such as in the presence of oxygen vacancies. Similarly, missing metal atoms induces the creation of h^+, resulting in a p-type system. In n-type doping donor atoms lead to the raise of the E_F to the CB, while in p-type system the E_F lowers into the VB. In reality, the CB and VB shift in energy while the E_F remains static, although colloquially both behaviors are used interchangeably in literature (E_F moves vs. band movement). As the E_F moves deeper into the VB or the CB, the concentration of free carriers increases, and so does the conductivity of the material. Manipulation of the E_F is an important concept in SC field as the optoelectronic properties of the material are heavily influenced by the E_F. [46–48]

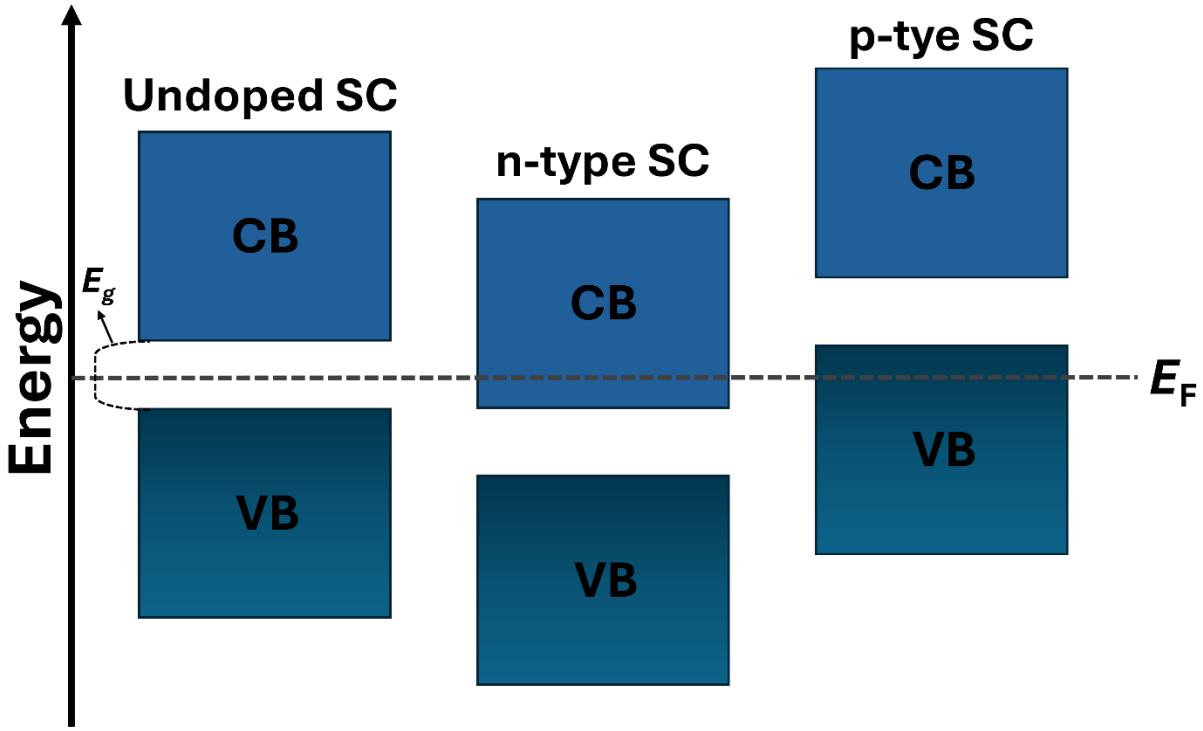

Figure 2. Representation of band diagrams for an undoped, n-type, and p-type semiconductor with tentative position of the Fermi level (E_F). The bandgap (E_g) is shown to denote the separation between CB and VB.

1.3.4 Carrier Effective Mass

Effective mass (m^*) is an important concept in SC physics that simplifies the behavior of charge carriers in a crystal lattice. It describes the deviation of the carrier mass when propagating through a crystal lattice, from the mass without any other interactions, *i.e.*, the mass of the charge carrier in vacuum. This deviation arises from all the possible interactions that the free carrier experiences as it travels through the crystal. The effective mass is obtained from the density of states (DOS) energy band structure of the SC. It is related to the curvature of the energy vs. the wavevector (k) relationship in the CB and VB. It is defined as:

$$\frac{1}{m^*} = \frac{1}{\hbar^2}\frac{\partial^2 E(\boldsymbol{k})}{\partial \boldsymbol{k}^2} \quad (1)$$

Where, $\hbar$ is the reduced Planck constant, $E(\boldsymbol{k})$ is the energy of the carrier as a function of the wavevector $\boldsymbol{k}$.[49]

In many SCs, it has been theorized that the effective mass is anisotropic, meaning it is not the same in all directions. This can be rationalized as the carrier travelling through different directions in a crystal, which corresponds to different projections in k-space. This phenomenon

has been observed and discussed more recently to account for discrepancies on m^* in some materials.[50] The m^* dictates a lot of properties that are key to developing electronic devices and understanding carrier behavior in SCs. The carrier mobility (μ) is a measure of how fast the carriers move through a material, which is an important property for electrical devices. The μ is related to m^* by: $\mu \propto 1/m^*$.[49] The electrical conductivity, thermal conductivity, DOS, Seebek coefficient, cyclotron resonance, and carrier lifetimes are all dependent on m^*. The m^* of a material can be theoretically calculated from the curvature of the bands in the DOS plot. There are multiple ways to obtain a m^* values experimentally, the most accurate one relies on the measurement of cyclotron resonance ω_c, where the cyclotron resonance is related to the m^* by: $\omega_c \propto 1/m^*$.

1.4 Defect Types: Origins of Charge Carriers

1.4.1 Doping

Doping is a general strategy where a small amount of impurity is purposely introduced into a SC crystal lattice to produce a defect that generates either n-type or p-type charge carriers. Si is a classic example of a SC with a narrow E_g that can be doped with very small amounts of dopants to induce n- or p-type conductivity, making it a crucial material for electronic applications. To produce n-type Si, group V elements, such as P, can be introduced into the crystal lattice to add an extra electron (e^-) per P atom, thus increasing carrier concentration. In a similar vein, group (III) atoms, usually B, can be doped into Si to produce holes (h^+) that induce p-type conductivity.[51] These are examples of extrinsic doping, which are dopants that are added purposely through substitutional doping (Figure 3). Intrinsic dopants are native crystals defects that form as the crystal grows. These native intrinsic dopants can induce carrier densities, and the density of defects can be controlled through synthetic conditions.

1.4.2 Oxygen Vacancies

In metal oxide SC materials, oxygen vacancies (V_O) are one of the most common intrinsic defects that lead to charge carriers. These vacancies arise from missing O atoms in the crystal lattice, where the lattice compensates by introducing two extra e^- into the system to keep

overall charge (Figure 3). These types of defects are very common and are responsible for the conductivity in ZnO, CdO, and SnO_2. This type or vacancy is usually associated with high effective mass due to increase scattering contributions that leads to rapid carrier recombination.[52,53]

1.4.3 Metal Vacancies

Metal vacancies (V_M), also known as cation vacancies, are crystal lattice defects where the metal atoms are missing from the regular positions (Figure 3). This type of defect can also introduce charge carriers into the system. Contrary to V_Os, these V_Ms induce h^+ into the lattice because the positive charge needs to be compensated to keep overall crystal charge. Due to the generation of h^+ from metal vacancies, Cu_2O, NiO, and $ZnMn_2O_4$ exhibit p-type conductivity.[54,55]

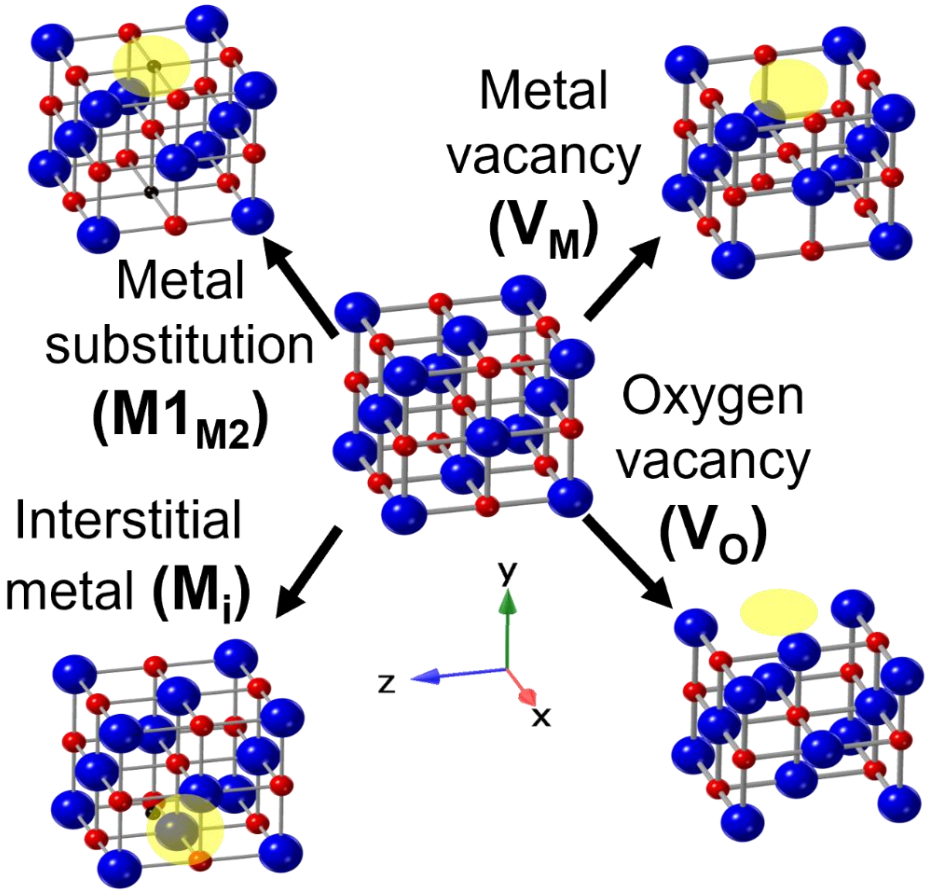

Figure 3. Intrinsic doping schemes that lead to carrier generation.

1.4.4 Interstitial Defects

Interstitial metal (M_i) is a rare case of doping because the dopant must be small enough to be able to slip into an interstitial position without perturbation of the crystal lattice (Figure 3). A practical example of this is Li-doped Al alloys, where the Li atom can fit within the Al lattice without disturbing the crystal structure. This Li interstitial addition has been observed to improve electrical conductivity.[56]

1.4.5 Antisite

An antisite defect is a crystallographic defect in which an atom of one type occupies a lattice site intended for a different type of atom. This defect occurs when atoms are displaced from their normal positions within the crystal lattice, leading to a deviation from the ideal atomic composition. An example of an antisite driven TCO is Cd_2SnO_4 (CTO) inverse spinel. In the inverse spinel CTO lattice, the octahedral (O_h) site is occupied by both Cd(II) and Sn(IV), and the other half of Cd(II) occupies the tetrahedral site (T_d). The true stoichiometry of the inverse spinel can be expressed as $Cd_{2-x}Sn_{1+x}O_4$, where the extra Sn(IV) population in O_h the site leads to free carrier generation.[57,58]

1.5 From Bulk to Nanomaterials

1.5.1 Transitioning from Bulk to Nano-sized Materials

When bulk materials transition to nanoparticles (NPs), several new properties arise due to the reduction in size and the increase of surface to volume ratio. These changes lead to unique physical and chemical properties that are not observed in the same bulk materials. For example, NPs exhibit new optical properties either by quantum size effects or plasmon resonances.

Quantum confinement effects occur when the nanomaterials are below the Bohr radius, leading to confinement of charge carriers in one or multiple dimensions. This confinement leads to the reduction of the band continuum into discrete energy levels, site dependent E_g, and altered DOS from their bulk counterparts. Quantum confined semiconductors are referred to as quantum dots (QDs), which show size tunable absorption and emission of light.[59,60]

The surface area to volume ratio (SA/V) in nanomaterials is a critical property that influences their properties at the nanoscale, and one of the reasons why nanomaterials possess such a plethora of applications. The majority of atoms in a nanomaterial reside at the surface, this leads to increased sensitivity to the medium surrounding them, which makes understanding of the surface environment key to grasp properties at the nanoscale, while in a bulk material the majority of atoms reside within the core. Because of this increased SA/V, nanomaterials exhibit higher density of active sites for reactions to take place, which makes nanomaterials great catalysts. This increased SA/V also improves the absorptivity, which is beneficial for sensor and filter applications.[59,60]

1.5.2 Surface Effects on Charge Carriers

At the nanoscale, size effects influence the behavior of charge carriers. Reduced carrier mobility is expected because of increased scattering at the surface. The high SA/V translates to the carriers having higher probability of encountering scattering centers that reduce carrier concentration and mobility. Surface defects can create localized electronic states that serve as traps, pinning down carriers and decreasing their degree of freedom. It is also possible for quantum confinement effects to affect the *m**of charge carriers, leading to lighter values than expected.

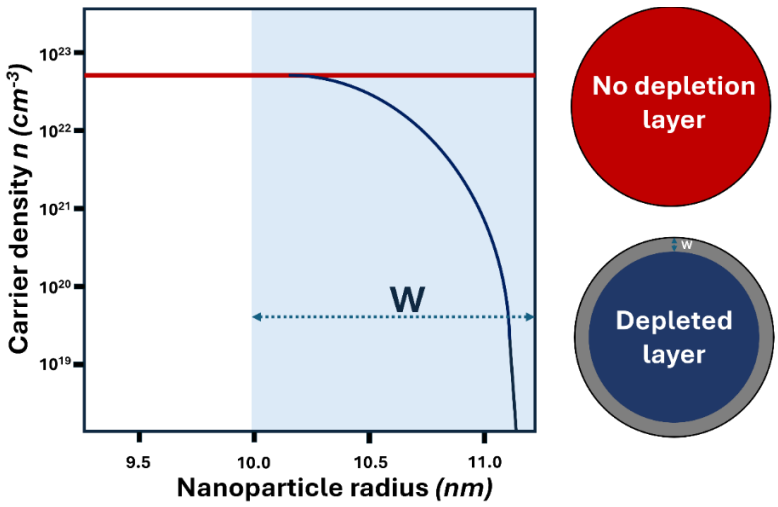

Figure 4. Plot showing how the carrier density changes as a function of particle radius due to the existence of a depletion layer. The behavior of depleted vs. non-depleted layer is shown in the plot.

An important concept that has become prevalent in the field of plasmonics is the depletion layer. The depletion layer in PSNCs is a region near the surface where the charge carrier density is significantly reduced compared to the core of the PSNC. The carriers in this depletion layer can be thought of as "non-activated carriers", meaning that they do not contribute to the LSPR response. This depletion region forms because of all the possible interactions between the PSNC surface and the surrounding environment, including defects, charge transfer events, absorbed molecules at the surface, solvent interactions, chemical reactions, and ligand electron density. Because the depletion layer acts as an insulating barrier, surface depletion reduces near-field enhancement effects and the sensitivity of the LSPR to the solvent dielectric. In a perfect crystal with no depletion layer, the carrier density will be constant regardless of surface depletion. When depletion layers exists, they change as a function of the nanocrystal size depending on the thickness of the layer (Figure 4).[61–63]

1.6 Plasmonic Effects

1.6.1 Permittivity and Dielectric Materials

The concept of permittivity plays a crucial role in the behavior of plasmonic materials. The permittivity (ε) is a measure of how much an electric field (**E**) is reduced inside a material compared to vacuum. Dielectrics are insulating materials that do not conduct electricity but can support an **E**. The permittivity of a dielectric material determines how it interacts with an electric field. Polarization occurs when an electric field is applied to a dielectric, the particles create an internal dielectric field to oppose the external one. The dielectric constant (ε_r) is the ratio of the permittivity of the dielectric to the permittivity of a vacuum. This relationship dictates how much electrical energy can be stored in the material as compared to a vacuum.[64]

1.6.2 Surface Plasmon Resonance

A plasmon at the surface of a material is known as a surface plasmon resonance (SPR), which is formed through collective oscillation of free electrons (free carriers) at the interface between the material and a dielectric medium (Figure 5). The dielectric function ($\epsilon(\omega)$) of a material dictates a lot of the plasmon behavior, and is expressed as a complex quantity,

$$\epsilon(\omega) = \epsilon'(\omega) + i\epsilon''(\omega) \quad (2)$$

where $\epsilon'(\omega)$ is the real part of the dielectric function, $\epsilon''(\omega)$ is the imaginary part of the dielectric function, and ω is the frequency of the incoming light. To form a plasmon, the real part of the material's $\epsilon'(\omega)$ must be negative and bigger than the dielectric constant of the surrounding medium, and $\epsilon''(\omega)$ should be as small as possible to enhance propagation length. The maximum plasmon extinction occurs when the $\epsilon'(\omega)$ crosses zero giving rise to a surface plasmon resonance.[2]

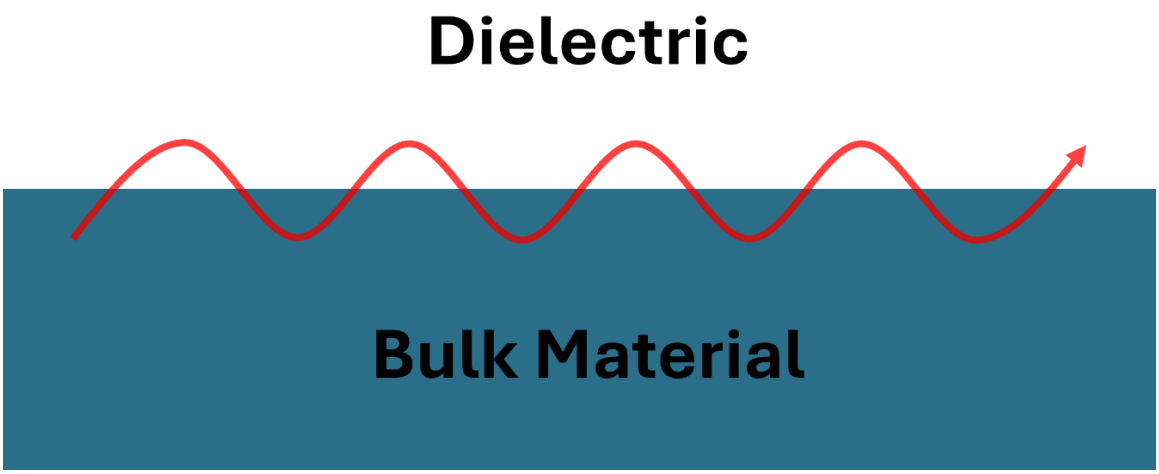

Figure 5. Illustration of plasmon resonance at the surface of a bulk material.

1.6.3 Localized Surface Plasmon Resonance

When a material transitions from bulk to a nanoparticle, the surface plasmon resonance cannot travel freely through the material and becomes a localized surface plasmon resonance (LSPR) that oscillates back and forward with incoming light (Figure 6). This localization occurs because the nanoparticles are smaller than the wavelength of light, and thus, the free charge carriers can only oscillate on the nanoparticle surface, with a frequency matching that of the incoming light. Because of the localization of the plasmon frequency to the nanoparticle surface, the LSPR properties are heavily dependent on the nanoparticle surface, shape, size, ligands, and overall chemical environment.[2]

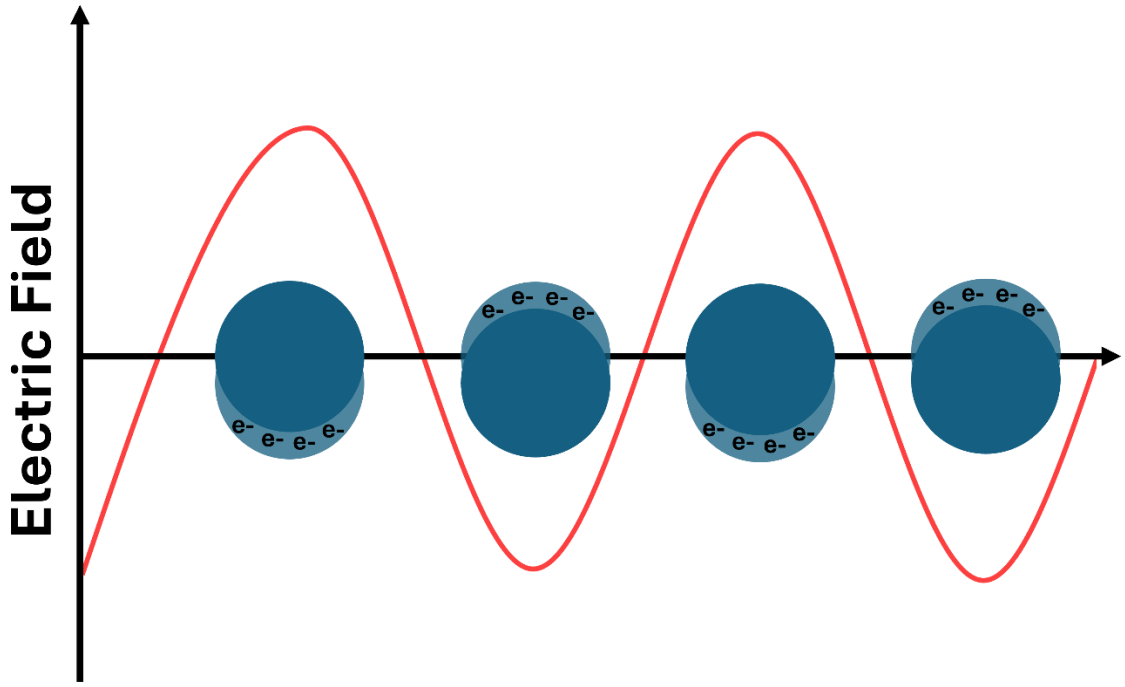

Figure 6. Charge carriers in a nanoparticle in resonance with upcoming electric field demonstrating the formation of a localized surface plasmon resonance.

1.6.4 LSPR Optical Response

LSPRs are highly sensitive to changes in the surrounding dielectric environment. Because the changes in LSPR are easily measurable, they are easily correlated to changes to the surrounding dielectric. This enhanced sensitivity allows LSPRs to be used as accurate optical rulers to measure changes in dielectric environments. To verify that extinction features are indeed due to LSPRs, a common method uses their sensitivity to changes in the dielectric environment. The LSPR is tested by obtaining the extinction spectra of the same material in solvents with different refractive indexes. If the feature in question is a LSPR, there is a linear shift in the plasmon energy as a function of solvent refractive index. Research groups are trying to understand the different effects of ligands with electron donating and withdrawing groups, and how they affect both band bending and the depletion layer. The LSPR can be tuned post-synthetically by utilizing a simple ligand exchange scheme to swap oleate ligands on the surface of In:CdO (ICO) nanocrystals for these electron donating/withdrawing ligands, which adds another avenue for tuning LSPR frequencies.[62]

Like other extinction features, LSPRs also possess an extinction coefficient, which is a measure of how well a species absorbs light, and it's a good metric to determine and compare

materials that absorb light. To put some perspective into how good some species are at absorbing light, the range extinction coefficient for the following species is: lanthanide (Ln) ions (1 to 10^3 $M^{-1}cm^{-1}$),[65] dyes (10^6 – 10^7 $M^{-1}cm^{-1}$),[66] and gold can reach values of up to 10^9 $M^{-1}cm^{-1}$ for spherical nanoparticles. This suggests that plasmonic nanoparticles are excellent materials for light harvesting applications.

Another well-known effect of LSPRs is their ability to enhance Raman spectroscopy, known as surface-enhanced Raman scattering (SERS). By adding the species to a gold substrate, the LSPR from the gold enhances the electric field that interacts with the sample, thus increasing their Raman scattering cross-section in the process. The Raman signal is enhanced, which allows for single molecule detection. This effect is very localized and allows for the detection of molecules that are close to the plasmonic substrate. Because Raman spectroscopy relies on inelastic scattering, which is a very small fraction of the scattered photons, SERS has allowed Raman to become a more feasible and powerful technique for sample analysis.[67]

1.7 The Drude Model

1.7.1 How to Utilize the Drude Model

The Drude model is a commonly used theory that allows to describe the electronic properties of SC materials. It is very useful because it describes the behavior of charge carriers in a simple and effective way, but relies on key assumptions to explain the behavior of free charge carriers.[68] The Drude model assumes that: (i) free charge carriers are affected by an electric field, (ii) free charge carriers interact with impurities, other charge carriers, and quasi-particles such as phonons, and (iii) the motion of these free charge carriers can be described by classical mechanics.

The Drude model can be used to solve for the frequency dependent dielectric function $\epsilon'(\omega)$ as given by:

$$\in(\omega) = \in_{\infty} - \frac{\omega_p^2}{\omega^2 + i\gamma\omega} \qquad (3)$$

where the ϵ_∞ is the high frequency dielectric constant, γ is the damping constant, ϵ_0 is the permittivity of free space, ω_p is the plasma frequency. The γ describes all the possible scattering

mechanisms, which dictate the lifetime and quality factor of the plasmon. When the frequency (ω) is held constant the equation can be rewritten as follows:

$$\omega_p = \sqrt{\frac{ne^2}{\varepsilon_0 m^*}} \quad (4)$$

where *n* is the number of free carriers, *e* is the charge of the carrier, ε_0 is the permittivity of free space, and *m** is the effective mass of the charge carrier. It states that the plasma frequency is dependent on the carrier density and inversely proportional effective mass of the carriers. This is the most used method for describing the plasma frequency of LSPRs. Manipulation of these two variables is what allows the fine tuning of LSPRs in plasmonic semiconductor nanocrystals (PSNCs).[1,3,25,26,69].

1.7.2 Plasma vs. Plasmon Frequency

The terms "plasma frequency (ω_p)" and "plasmon frequency (ω_{LSPR})" are often used interchangeably in the literature, but this usage is frequently incorrect. The observed ω_{LSPR} is related ω_p to by the following relationship:

$$\omega_{LSPR} = \frac{\omega_p}{\sqrt{\varepsilon_\infty + 2}} \quad (5)$$

where ε_∞ is the high frequency dielectric constant of the material. This occurs because the plasmon is no longer free (localized), opposite to the SPR where the plasmon is free to propagate over the surface of the material. These two values are not identical, and utilizing this relationship incorrectly can lead to incorrect reported values.[2]

1.8 Semiconductor and Metal LSPRs

1.8.1 Differences Between Semiconductors and Metals

Using SCs instead of metals for plasmonic applications offers several advantages. Metals are opaque in the visible region due to scattering and other possible optical transitions; therefore, they are heavily limited for optoelectronic applications. A good number of SCs do not have optical transitions in the visible range which makes them optically transparent. Utilizing wide bandgap semiconductor materials with high carrier concentrations (either extrinsic or intrinsic)

ensures that there are no other optical pathways available, thus improving transparency in the visible.

Current technological demands require plasmonic materials to have extinction features throughout the infrared side of the electromagnetic spectrum to target light harvesting in solar cells,[70] telecommunications,[71] medical field,[6] and many other applications. Metals cannot host infrared plasmons because of their usually high carrier densities, and SCs can be tuned all the way from the infrared to the visible side of the electromagnetic spectrum. Most common plasmonic SCs rely on abundant elements such as Zn, Cd, Sn, and are usually binary or ternary oxides of these elements making them cheap to manufacture. In addition, oxides tend to be relatively stable, which makes them easier to produce and work with in an industrial setting for device manufacturing.

1.8.2 Tunability of Carrier Density in SCs

The main advantage of utilizing SCs instead of metals is in the ability to tune the carrier concentration, thus manipulating the frequency of the LSPR. The most common way to achieve this is by using extrinsic dopants into a host lattice to induce free charge carriers. The most famous example is Sn (IV) doped In_2O_3 (ITO) where the LSPR frequency can be tuned as a function of Sn (IV) content. The LSPR frequency can also be tuned by changing the density of intrinsic dopants. The most common examples of these are the manipulation of V_Os in TiO_2,[72] WO_3,[50] ZnO,[73] and CdO[74] through annealing conditions, thus increasing carrier concentration with increasing V_O content.

1.8.3 Tunability of Effective Mass

Carrier density is usually the simplest way of manipulating the frequency of the LSPR in PSNCs. Recalling the Drude model, it is also possible to tune the LSPR energy by manipulating the m^* of a material. The m^* of the charge carrier is tied to the intrinsic nature of the carrier. For example, free charge carriers coming from a V_O have higher scattering and a more polaronic nature, leading to higher m^* values in SC oxides.[75,76] The m^* of the material can be tuned a through doping schemes that can bend the curvature of the conduction band, thereby changing the m^* as a function of dopant.[77]

1.9 Instrumentation Techniques

1.9.1 Spectroscopy and Structural Techniques

The plasmonic properties of PSNCs can be analyzed through different spectroscopic techniques. Simultaneously, the structure and size of PSNCs can be probed through X-ray diffraction methods to correlate structure to carrier density and behavior. This section will discuss some of the techniques that are utilized to explore and understand PSNCs using a very large range of light frequencies spanning from X-rays to radio waves.

1.9.2 Ultraviolet-Visible-Infrared Spectroscopy

A UV-Vis-IR spectrometer (Figure 7) is an instrument used to measure the absorbance (transmittance) of light across the ultraviolet (UV), visible (Vis), and infrared (IR) regions of the electromagnetic spectrum. This range usually spans wavelengths from 200 to 3500 nm. The measured absorbance can be understood through the Beer-Lambert law:

$$A = \alpha l c \quad (6)$$

Where A is the absorbance of the material, α is the molar extinction coefficient of the sample, l is the path length that the light travels through the sample, and c is the concentration of particles in solution.[78]

A UV-Vis-IR spectrometer consists of several key components. The light source typically includes a deuterium lamp for the UV region (200 – 400 nm) and a tungsten-halogen lamp for the visible (400 – 700 nm) and IR (700 – 3300) regions. A monochromator disperses the light into different wavelengths using a diffraction grating or prism, selecting a specific wavelength to be collected and pass through the sample. The light is transmitted through the sample where it travels and hits a detector. The detector measures the intensity of light that passes through the sample, with common detectors including photodiodes for UV-Vis regions and InGaAs detectors for the IR regions. Finally, the data collected by the detector is sent to a computer where is converted into readable format and displayed as a spectrum plot. The difference in carrier density between samples can be monitored through a shift in the LSPR frequency and it's a key

technique to investigate plasmonic materials.[78]

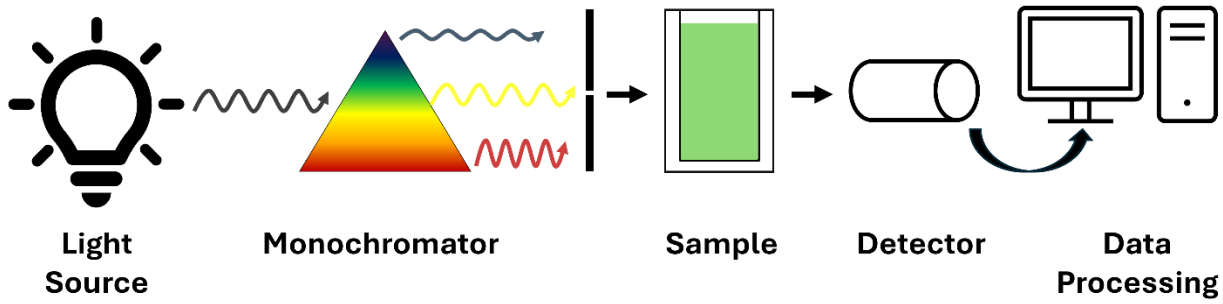

Figure 7. Schematic diagram of a typical UV-Vis-IR absorption spectrometer

1.9.3 Fourier Transfer Infrared Spectroscopy

Fourier transfer infrared (FTIR) spectroscopy is an optical technique that that relies on interferometry, and is used to measure an infrared absorption spectrum of a material. An interferometer splits a beam of light into two paths, reflects them back, and recombines them to produce interference patterns. The most common interferometer set up that most instruments use is the Michelson type interferometer

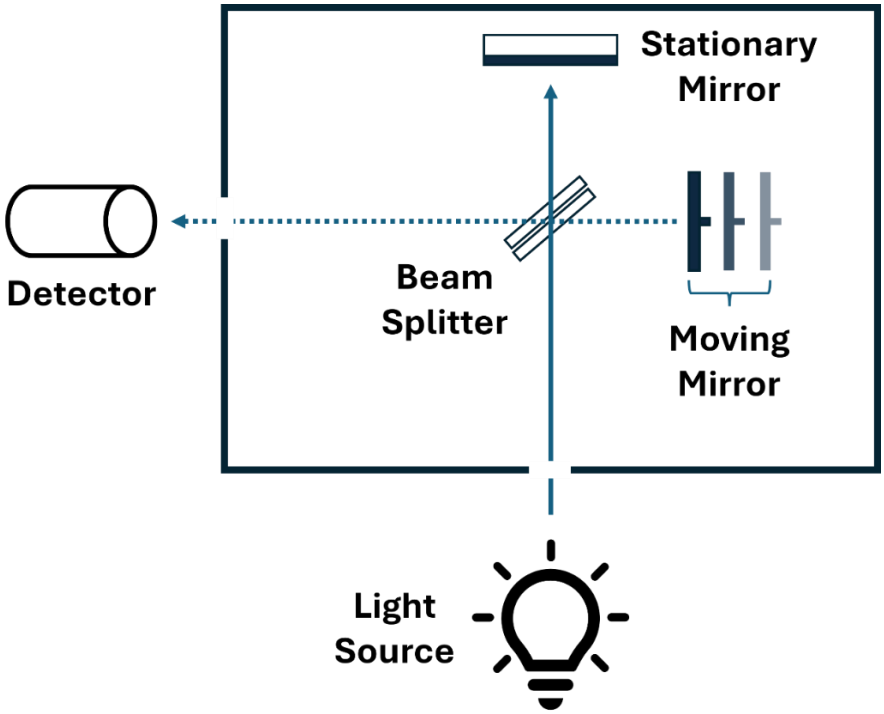

Figure 8. Typical FTIR set-up demonstrating the Michelson interferometer.

The typical FTIR set-up using the Michelson configuration (Figure 8) includes a beam splitter that divides the incoming light into two beams, which are then reflected towards the beam splitter by the mirrors. One of these mirrors is a moving mirror that moves back and forth to create a variable path length difference. The recombined beams travel to a detector and produce an interference pattern known as an interferogram, which results from the difference in the measured optical paths. The interferogram is transformed using a Fourier transform that converts the signal from time domain to frequency domain. This new spectrum shows the intensity of light as a function of frequency. This set up has revolutionized IR spectroscopy by making it fast and reliable. This technique is typically used to analyze organic samples and try to identify them through the vibrations of different functional groups, but it can also look at bonding/structure, polymorph structures, loading levels in thin films.[78]

1.9.4 Nuclear Magnetic Resonance Spectroscopy

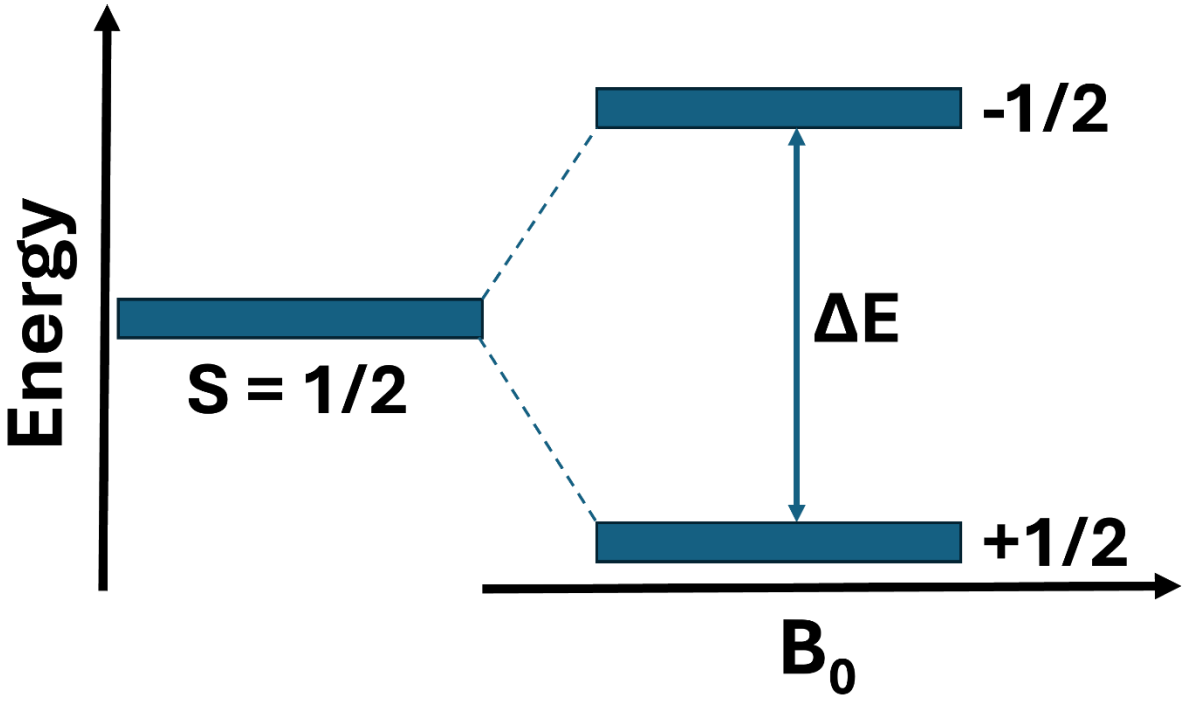

Figure 9. Zeeman splitting of a nucleus with a ½ spin under a magnetic field B_0.

Nuclear magnetic resonance (NMR) spectroscopy is a powerful analytical technique used to understand the structures, dynamics, and chemical environments of atoms and molecules.

NMR spectroscopy is one of the lowest-energy spectroscopies relying upon the absorption of radiofrequency (RF) band radiation. The main advantage of NMR spectroscopy is its element-specific nature, allowing it to provide detailed information about the environments of specific atoms. This contrasts with the aforementioned spectroscopy techniques, which do not offer this level of element-specific insight.[79]

In the absence of a magnetic field, nuclear spins have the same energy. However, when a magnetic field (B_0) is applied, this degeneracy is lifted and the energy level splits. The energy difference (ΔE) between the two states is given by the following equation:

$$\Delta E = \gamma \hbar B_0 \quad (7)$$

where γ is the gyromagnetic ratio, $\hbar$ is the reduced Plank's constant, and B_0 is the magnetic field strength. For a nucleus with a spin of ½ such as ^{1}H, this results in two distinct energy levels, a lower level aligned with m = +½ and a higher energy level with m = -½ aligned against the field. The transition between these two levels happens when the nucleus absorbs RF radiation that matches the ΔE between the two energy levels (Figure 9). The transitions in NMR are only allowed if the nuclei have a non-zero nuclear spin. If S = 0, such as ^{4}He, ^{12}C, ^{16}O and ^{32}S, no signal is observed in NMR. Elements with S = ½ (^{1}H, ^{13}C, ^{19}F) have a single transition, which makes them easy to analyze through NMR spectroscopy. Nuclei with S > ½ are referred as quadrupolar, and the number of possible transitions increases.[79,80]

The NMR experiment (solution in this case) begins with dissolving the sample in deuterated solvent such as D_2O or $CDCl_3$. Deuterated solvents (^{2}H) are used in ^{1}H NMR to stabilize the magnetic field, and so the solvent peaks do not overlap with the sample's signal. The solution is transferred to a glass NMR tube, and inserted into the NMR spectrometer. Inside the spectrometer, the NMR tube is carefully put in between a uniform magnetic field generated by a superconducting magnet ranging from 1 to 35.2 T (50 MHz to 1.5 GHz for ^{1}H). This B_0 aligns the nuclear spins in either parallel or anti parallel configurations (low vs. high energy configurations). A RF transmitter sends a short pulse of RF radiation at the Larmor frequency, matching the energy difference between the nuclear spins states and creates a non-equilibrium state by flipping some of the spins from the low energy state to the higher energy state. The most common pulse sequence is a Bloch decay, which is simply a single 90° pulse that aligns the spins perpendicular to B_0. After the RF pulse, the excited nuclei relax to their lower energy state, and emit an RF signal. This emitted RF signal, also known as a free induction decay (FID), which is

detected by a receiving coil in the probe. The FID is transformed into a frequency-domain signal using a Fourier transform, which results in the familiar NMR spectrum that displays intensity vs frequency/chemical shift. The position of each feature in the NMR spectrum is measured in parts per million (PPM), which denotes the chemical shifts reflecting the chemical environments that the nuclei experience. The peaks can split (J-coupling) depending on the number of interactions between surrounding nuclei, which gives a lot of important information that allows for determination of further information about the environments of the nuclei. The area under each peak is proportional to the number of nuclei responsible for that feature, which is taken advantage of in ^{1}H solution NMR to determine the relative numbers of protons.[79]

Solution state NMR is the most common type of NMR, and is readily used to analyze ^{1}H and ^{13}C in solutions, making it an indispensable tool for organic chemists when it comes to the analysis of molecules for purity and structure. In solution, molecules are free to rotate and move freely, which eliminates the anisotropic effects of the NMR interactions. In nanoparticle research, solution NMR is frequently employed to identify ligands bound to the surface of nanoparticles. The binding of these ligands causes a broadening of the observed peaks, distinguishing them from free ligands in solution. In practice, solution NMR is not used to study NPs because they are semi-solids with poor solubility and lack of free tumbling motion present in molecules. For these reasons, it is better to analyze NPs through solid-state NMR (SSNMR) rather than solution NMR.[81]

In SSNMR, the principles are the same, but the sample is not dissolved in deuterated solvent, rather, the samples are usually fine powders that are packed into a small rotor. As previously mentioned, one of the challenges of SSNMR is that the molecules are not free to move/tumble and the anisotropic interactions are not averaged out. This results in much broader spectral patterns that are more challenging to interpret than those obtained through solution NMR. However, these patterns contain valuable information that can be useful depending on the system being studied. Another important aspect of SSNMR is the utilization of the magic-angle spinning (MAS). This technique works by spinning the rotor holding the sample at an axis of 54.74° to replicate some of the effects that tumbling that happens in solutions to average the anisotropic interactions. Rotors can spin at rates from 1 to 100 kHz, but usually require specialized NMR probes and rotors to be able to go to rates higher than 40 kHz. To effectively average dipolar couplings in SSNMR, the spinning rate must exceed the magnitude of the dipolar

coupling. If the spinning rate is too low, it may not average these interactions, potentially yielding no significant improvement in any signal acquisition. The ability to change the spinning rate during the MAS experiment allows to determine the anisotropic shift from spinning side bands.[80]

Most NMR experiments are performed on diamagnetic samples, but samples with unpaired electrons (paramagnetic nuclei, SCs, and metals) can be studied, but sometimes can prove challenging. SSNMR spectra of these samples often show distortions and line broadening due to nuclei coupling with unpaired electrons. The presence of unpaired electrons can significantly affect the T_1 and T_2 relaxation time constants. This can sometimes speed up NMR experiments by reducing the necessary recycle delays.

Measurements on wide band gap semiconductors have revealed that the NMR signal breadth is dependent on the elemental environment (chemical shift, CS) and on contributions from the hyperfine nuclear-magnetic interactions with conduction band electrons (Knight shift, KS). While CS and KS is impacted by *n*, both are field dependent, and KS is proportional to $n^{1/3}$ and to frequency (KS $\propto \vec{B}$). [82–85] Thus, the breadth of the KS in the NMR spectrum for a PSNC will depend on *n* and on the experimental NMR magnetic field, which allows for the discrimination of CS vs. KS effects by using high field magnets. [86] KS can be distinguished from CS through temperature dependent T_1 measurements via the Knight-Korringa relationship. Knight-Korringa behavior arises from interaction of conduction electrons with the nuclear spin leading to a temperature dependent T_1 relaxation, such that $(KS)^2 = 1/[T_1T[(4\pi k_B/\hbar)(\gamma_n/\gamma_e)^2]]$, [87,88] where T_1 is the spin-lattice relaxation, T is temperature, k_B is the Boltzman constant, γ_n is the nuclear gyromagnetic ratio, and γ_e is the free electron gyromagnetic ratio. KSs in bulk semiconductors (PbTe, PbSe, P:Si, CdO, GaAs, and GaN) have been reported in the past While KSs are not typically observed in wide band gap semiconductors, KS has been reported as a shift in the NMR resonance in PSNCs through KS and Knight-Korringa behavior. [76,89,90] The ability to distinguish carrier induced changes in CS and KS in CdO and CTO is reasonable based on the literature report for single crystal ^{113}CdO where a carrier density of 2.6 x 10^{19} cm^{-3} yields a KS of 8 MHz with a Korringa correlation of T_1T = 168 $s^{-1}K^{-}$.[191]

1.9.4.1 Pulse Sequences. The quality of NMR spectra can be further enhanced by utilizing different pulse sequences other than a regular Bloch decay, The Hahn echo and Carr-Purcell Meiboom-Gill (CPMG) experiments have become standards in the acquisition of

wideline SSNMR spectra. The Hahn echo pulse sequence has the form of $\pi/2 - \tau - \pi - \tau -$ acquisition, where the pulse is centered between two equal delays, τ, to refocus spin polarization. The CPMG pulse sequence is a variation of the Hahn echo, consisting of a series of π-refocusing pulses that repeatedly refocus dephasing magnetization, structured as $\pi/2 - \tau - \pi - (\tau -$ acquisition$)_N$. The number of refocusing pulses, N, is limited by effective T_2 relaxation, which determines the number of echoes that can be acquired. The CPMG sequence, initially created for T_2 measurements in solution NMR, is now extensively utilized in SSNMR to enhance signal quality.[92–94]

CPMG experiments use bandwith-limited rectangular pulses, which are inadequate for acquiring spectra with powder patterns extending several hundred kHz or more. Frequency-swept (FS) pulses, which modulate phase and/or amplitude to span a range of frequencies, can excite and refocus spin polarization across a wider bandwidth. FS wideband uniform-rate smooth truncation (WURST) pulses, often employed in conjunction with CPMG (referred to as WURST-CPMG or WCPMG), provide the dual benefits of signal enhancement and the capability to manage large pattern bandwidths.[95–98]

1.9.5 Powder X-Ray Diffraction

Powder X-ray Diffraction (pXRD) is a powerful analytical technique that allows identification of crystal phases, structural parameters, quantification of phases in mixed materials, size, and strain. Samples in powder form are used which consist of small crystals oriented randomly. When X-rays (Cu Kα = 1.5406 Å) are directed at this powdered sample, they interact with each crystal plane within each nanosized crystal in accordance with Bragg's law (Figure 10). According to Bragg's law, constructive interference occurs when the path difference between X-rays scattered by successive crystal planes is an integer multiple of the X-ray wavelength, given by the equation,

$$n\lambda = 2d \sin\theta \tag{8}$$

where n is an integer, λ is the wavelength of X-rays used, d is the d-spacing between lattice planes, and θ is the angle of incidence and reflection of the X-rays. When the X-rays interact with the sample they scatter based on Bragg's law and create a constructive interference that creates peaks at specific 2θ angles based on the d-spacing of the specific crystal phase. Each 2θ peak in the powder pattern represents a unique crystallographic plane in the sample. In

conjunction to the random orientation of the crystals, these peaks allow the creation of a fingerprint pattern that can be used to identify the sample by comparing it to other powder patterns from crystallographic databases.[99]

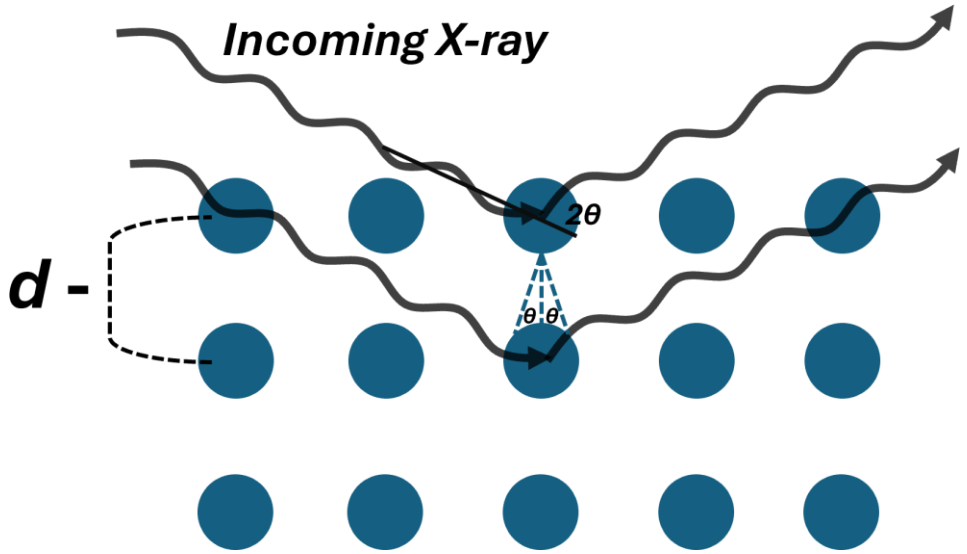

Figure 10. Diagram that shows application Bragg's law in a pXRD experiment where the constructive interference is produced when the Bragg condition is met.

In addition of collecting a powder diffraction patterns, pXRD can be used for phase identification and quantification, crystallite size and microstrain analysis, lattice parameter determination, residual stress measurement, structure solution and refinement, in-situ and operando studies, amorphous content identification, compositional analysis, phase transition studies, and crystallinity quantification. These capabilities make pXRD a powerful tool for comprehensive characterization both in the bulk and nano-sized materials[99]

CHAPTER 2

EXAMINING HIGHLY MOBILE FREE CARRIERS IN PLASMONIC CADMIUM STANNATE INVERSE SPINEL NANOCRYSTALS

2.1 Introduction

Plasmonic nanomaterials are observed to enhance photocatalysis,[4] photovoltaics,[70] sensors,[100] telecommunications,[71] night vision,[101] and photothermal therapy.[102] While the mechanistic origins of these enhancements are still under discussion, developing new cost-effective plasmonic nanomaterials that have high carrier densities and tunable plasmon features is critical to future implementation of these findings. Not surprisingly, the development of plasmonic semiconductor nanocrystals (PSNCs) using wide band gap, metal oxide (MO_x) semiconductors is beginning to replace noble nanometals for plasmonics research, reflecting their lower cost, high carrier densities ($> 10^{19}$ cm^{-3}), transparency in the visible spectral region, and the possession of a tunable localized surface plasmon resonance (LSPR) frequency.[103–107] MO_x PSNCs are an important class of n-type plasmonic materials shown to exhibit high conductivity and mobility in thin films and form the basis of transparent conducting oxide industrial technology.[43,108–112] The LSPR frequencies of MO_x PSNCs are predictable using dielectric modeling of the carrier effective mass (m^*), carrier density (n), band parabolicity, and degree of compensation centers arising from lattice defects.[69,104,113–118] The most heavily studied n-type MO_xs rely on oxygen vacancies (V_O) to induce carriers in the conduction band (CB); however, the presence of V_O's is associated with rapid carrier trapping following LSPR excitation in PSNCs.[119] Recently, it has been theorized that antisite occupation in inverted spinels can lead to n-type doping in non-stoichiometric phases without the involvement of V_O[120]Traditional spinels formed from A^{2+}/B^{3+} cations are often employed as optical host materials,[121–123] while spinels formed from A^{2+}/B^{4+} are much less explored. Spinels are a chemically resistant ternary line phase that can form as a normal AB_2O_4, inverted $A(AB)O_4$, or a combination $(A_{1-x}B_x)[A_{x/2}B_{1-x/2}]_2O_4$ of the two phases. In the normal spinel, the A-cation occupies a tetrahedral (T_d) site while the B-cation occupies an octahedral (O_h) site. In the inverted spinel, the A-cation occupies both the T_d and O_h lattice sites, while the B-cation occupies only the O_h site. In inverted spinels, antisite occupation can occur, where one cation is

located on a lattice site that would normally be occupied by the other cation. Increased carrier densities have been reported in thin films for these types of systems, suggesting antisite populations may play an effect.[57,124,125] Further study on inverted spinel MO_x PSNCs and the nature of the carriers' parentage can open new frontiers for the discovery of semiconducting materials for applications in photonics and electronics.

The n-type CTO and n,p-type Ga_2FeO_4 (GFO) NCs have been reported to exhibit absorption features tentatively assigned to plasmons by fitting to the Drude model.[103,126] Density functional theory (DFT) calculations on CTO, GFO, and n,p-type $FeAl_2O_4$, support the hypothesis that CTO and GFO are able to support high carrier densities without V_O formation.[127] CTO is an important wide band gap (E_g) semiconductor, as its carrier properties do not depend on V_O, and it is very chemically stable. CTO is non-magnetic with carrier densities on the order of 10^{19} - 10^{20} cm^{-3} and carrier effective masses ranging from 0.33 to 0.028m^*/m_e, depending on synthetic conditions.[35,103,128–132] CTO has been of interest since the 1970s, following reports that thin film CTO is a potential transparent conducting oxide competitive with the well-known $Sn:In_2O_3$.[131–133] In thin film CTO, it was unclear whether the observed carriers were attributable to V_O, typically observed in n-type MO_xs, or antisite formation from the non-stoichiometric Sn to Cd ratio. Siegel later revealed that CTO crystallizes in the inverse spinel structure rather than the orthorhombic structure in thin films, leading to improved optoelectronic properties attributable to self-doping by antisite population of the Cd O_h site (Sn_{Cd}).[134] In CTO, the population of Sn(IV) is greater than Cd(II) at the O_h site, deviating from the stoichiometric formula ($Cd_{2-x}Sn_{1+x}O_4$), and leading to carrier formation by introducing electrons into the CB from the Sn(IV) atoms. The role of antisite occupation in CTO was theoretically supported by Zang et al.,[125] and charge carriers in CTO at the nanoscale were reported to generate a feature in experimental NIR spectra that were assigned as an LSPR. The reported CTO thin film results suggest CTO PSNCs are a promising material for antisite carriers lacking V_O. A recent study suggests that CTO nanocrystals are plasmonic; however, direct evidence of the carrier effective mass, electron *vs.* hole doping, and metallic-like carriers expected for a PSNC have not yet been reported.

In this work, direct evidence of metallic character in highly faceted CTO PSNCs is provided by the observation of large Knight shifts in ^{113}Cd and ^{119}Sn solid-state NMR (SSNMR) spectra, which can be correlated with the appearance of an LSPR in the NIR. The 19 ± 2 nm CTO PSNCs are passivated by oleic acid and exhibit an octahedral motif consistent with the

cubic crystal structure observed in powder X-ray diffraction (pXRD). The LSPR feature centered at 0.52 eV (2384 nm) is observed to be trimodal due to octahedral faceting of the CTO PSNCs (i.e., corner, edge, and face contributions to the LSPR). Using m^* determined from magnetic circular dichroism (MCD), the LSPR extinction can be fit to a 3-mode simplified Drude approximation (SDA) to extract n. The LSPR and E_g are observed to shift to lower energy with the addition of nitrosonium tetrafluoroborate ($NOBF_4$), corresponding to free carriers being titrated from CTO. The observed bathochromic shift in LSPR is consistent with the Drude model,[135] while the E_g shift to lower energy is consistent with Burstein-Moss behavior.[136,137] The corroborating data provides direct evidence that the carrier population in CTO is antisite driven, confirming the earlier speculation by Ye and coworkers.[103] From a broader perspective, this study of highly-faceted CTO PSNCs suggests that further research on inverted spinels may lead to the discovery of new nanomaterial spinels for plasmonic materials and applications.

In addition, the study establishes a powerful toolset to interrogate carrier behavior in PSNCs: when MCD and SSNMR measurements are deployed, the role of n-type dopants can be analyzed. There are relatively few reports of SSNMR spectroscopic characterization of PSNCs, despite its ability to measure both isotropic and anisotropic (i.e., orientation dependent) NMR interactions, which provide insight into local atomic environments in their cores and on their surfaces, nanoparticle (NP) size, coordination chemistry, surface characteristics, and electronic structure.[81,138] Aside from the potential influences of isotropic chemical shifts and chemical shift anisotropies (CSAs) that impact the SSNMR spectra of spin-1/2 metal nuclides like ^{113}Cd and ^{119}Sn in NPs, it is sometimes possible to observe Knight shifts (KS) and Knight shift anisotropies (KSAs),[139–141] which arise from the presence of conduction electrons in metallic NPs[142,143] or free carriers in semiconducting NPs.[144] KS and KSA typically manifest in SSNMR spectra as large frequency shifts (positive or negative) and extreme broadening, respectively, and are very often observed in the SSNMR spectra of conducting metals,[145,146] as well as other solid materials that conduct electricity (like semiconductors).[147] Of relevance to the current work is the measurement of Knight shifts from ultra-wideline SSNMR spectra (i.e., powder pattern breadths > 250 kHz),[98,148] and their correlation to band gap structure and the locations of free carriers in the NPs.[149] SSNMR spectroscopy adds to the tools available to PSNC researchers for unravelling the properties of this important class of materials with a broad range of technologically relevant applicability.

2.2 Experimental Methods

2.2.1 Synthesis of CTO Inverse Spinel PSNCs

The CTO PSNCs are synthesized following a modified method from the one reported by Ye and co-workers,[103] where the original Sn(IV) source is substituted for a Sn(II) acetate precursor. In a 3-neck round bottom flask fitted with a condenser and a thermocouple, cadmium acetylacetonate ($Cd(acac)_2$, 1.2 mmol) and tin(II) acetate ($Sn(OAc)_2$, 0.3 mmol) are combined with OA (7.5 mmol) and ODE (25 mL). The solution is degassed at 120 °C for 1 hour, and then rapidly heated to 319 °C where is kept refluxing for 100 minutes until the solution turns dark black/grey indicating the nucleation of CTO PSNCs. The PSNCs are isolated by addition of IPA, followed by selective precipitation of the smaller TCO in toluene from bigger metallic Cd particles that form as a byproduct. The isolated TCO NCs are then passed through a toluene gel permeation chromatography (GPC) column to remove excess ligand following published procedure.[150] The NCs are kept in toluene or TCE for storage.

2.2.2 General Characterization

Powder X-ray Diffraction (pXRD) patterns were collected with a Rigaku MiniFlex powder X-ray diffractometer using a Cu Kα source. The pXRD patterns were collected using a zero-background micro-powder plate. Scans were collected from 15 to 70° at a rate of 7°/min and a 0.05 step size.

X-ray photoelectron spectroscopy (XPS) was obtained on CTO powder deposited on carbon tape using a PHI 5100 X-ray photoelectron spectrometer. The XPS has an excitation source of Mg Kα, with a pass energy of 22.36 eV to minimize linewidth. All samples were calibrated to the aliphatic carbon assignment (C1s 284.8 eV).

UV−Vis−NIR absorbance of purified TCO are dissolved in TCE for all optical measurements. The optical data were collected in a PerkinElmer Lambda 950 spectrometer. A 1 mm path length NIR quartz cuvette was used for all absorbance measurements. Spectra were corrected using TCE.

High-angle annular dark-field scanning transmission electron microscopy (HAADF-STEM) and EDX measurements were performed at 300 kV on an FEI Titan Themis3 (scanning) transmission electron microscope.

Chemical titrations were performed with one electron oxidant ($NOBF_4$) in a similar manner to Conti et al.[69] A known concentration of purified CTO crystals was flushed under N_2 and brought into an inert atmosphere glovebox. A known concentration of the $NOBF_4$ in MeCN (acetonitrile) was slowly titrated into the CTO solution, shaken, then left to react for 30 min. The sample is then transferred to a 1 mm quartz cuvette transparent in the NIR region and loaded into the PerkinElmer Lamba 950.

2.2.3 Computational Details and Modeling of CTO PSNCs

Modeling of CTO octahedrons NCs is generated using the NanoCrystal software tool.[151] DFT + U calculations were performed using a plane augmented wave pseudopotential for O atoms and ultrasoft pseudopotentials for Cd and Sn atoms selected from the SSSP database[152,153] *via* QuantumESPRESSO.[154] The unit cells used for calculations are prepared by taking an initial bulk unit cell of CTO ($Fd\bar{3}m$, a = 9.174 Å, ICSD-69299),[155] symmetry reducing using SeeK-path,[156] and then atomically relaxing, resulting in three representative unit cells of $Cd_{4-x}Sn_{2+x}O_8$ (x = 0, 1, 2) to simulate increasing [Sn_{Cd}] behavior on the electronic band structure. The resulting lattice parameters are kept constant for all unit cells, where a cubic structure ($Fd\bar{3}m$, a = 4.587 Å) was used, matching half the lattice parameter of ICSD-69299. The kinetic energy cutoff for charge density and wavefunctions are 600 and 75 eV respectively, while a Monkhorst k-point mesh of 4 × 4 × 4 was used to perform even sampling across the dielectric field of the Brillouin zone.[157] A non-self-consistent field calculation of 12 × 12 × 12 is used to obtain the projected density of states (DOS) and band diagrams. Hubbard U parameters are applied to Cd 4*d* (10 eV), Sn 4*d* (9 eV), and O 2*p* (8 eV) orbitals to better approximate the experimental E_g for CTO, as performed previously in literature.[158]

2.2.4 Magnetic Circular Dichroism Measurements

Thin films of CTO PSNCs were prepared by drop-casting from a colloidal solution with TCE onto a quartz substrate. The concentration was mediated by monitoring the CTO band gap absorption using a Cary 50 Bio UV-Vis spectrophotometer until absorption units of no more than

0.5 was obtained. Afterwards, VGE-7031 varnish was applied to adhere the quartz substrate onto the optical probe for use in the cryostat.

Variable Field (+ 6 T at 40 K) Magnetic Circular Dichroism (VH-MCD*)* is performed on a home-built system and is more thoroughly described in a previous report.[118] Deviations and critical components are described herein. After sample adhesion, the dropcast CTO was dried under vacuum prior to insertion into an Oxford Instruments HelioxTL Superconducting Spectromag. A Newport Xe Arc Lamp is used as the light source in combination with a ThorLabs Glan-Taylor linear polarizer (GLB-10) to linearly polarize incident light, followed by the use of a HINDS Instruments photoelastic modulator (PEM-100) for subsequent circular polarization. A Hamamatsu PMT amplified with a Femto current amplifier (LCA-200K-20M) is used to measure the UV-Vis spectra from 4.4 – 2.5 eV. Temperature was monitored and controlled through a Keck-Clamp fiber cable routed through the sample probe and mounted adjacent to the sample substrate. A positive and negative field sweep scan from 0 - 6 T was performed for the stannate samples at 40 ± 0.5 K in 2 T intervals. The collected spectra were corrected by subtracting the 0 T scan to reduce artifacts from polarization effects, magnetic field inhomogeneity, and other anomalies during spectral measurements.

2.2.5 Multinuclear Solid-state NMR (SSNMR) Characterization

^{113}Cd and ^{119}Sn SSNMR experiments were performed using a Bruker NEO console with an Oxford 18.8 T ($\nu_0(^1H)$ = 800 MHz) magnet operating at $\nu_0(^{113}Cd)$ = 177.545 MHz and $\nu_0(^{119}Sn)$ = 298.325 MHz, respectively. A home-built 3.2 mm HXY MAS probe was used for all NMR experiments performed at 18.8 T. Pulse width calibrations and chemical shift reference frequencies for all nuclei were calculated using their respective solid-state standards. ^{113}Cd and ^{119}Sn chemical shifts are reported with respect to $Cd(ClO_4)_2$ and $Sn(CH_3)_4$ (δ_{iso} = 0 ppm) using $Cd(NO_3)_2{\cdot}4H_2O$ (δ_{iso} = −102 ppm) and solid SnO (δ_{iso} = 121 ppm), respectively, as secondary references. The experimental conditions and acquisition parameters for each class of experiments, which include basic ^{1}H-X CP/MAS,[159] ^{1}H-X CP/CPMG,[160,161] and direct excitation WURST-CPMG are summarized in Tables 1 and 2.

Table 1. NMR parameters used in the acquisition of ^{113}Cd SSNMR spectra.

	WURST-CPMG	CP-CPMG	CP/MAS
MAS Rate (kHz)	–	–	15
Number of Transients	4,096	4,096	16,384
Recycle Delay (s)	6	1.25	1
Dwell Time (μs)	1	1	1
Spectral Window Width (MHz)	1	1	0.5
Number of Meiboom-Gill loops	75	50	–
Acquisition Time (ms)	16	9	1.02
^{1}H Continuous-Wave Decoupling Power (kHz)	35	50	50
WURST Pulse Length (μs)	50	–	–
WURST Sweep Range (kHz)	600	–	–
WURST Pulse Power (kHz)	28	–	–
Spin Echo Length (μs)	100	100	–
^{1}H Excitation Pulse Length (μs)	–	5	8
^{1}H Excitation Pulse Amplitude (kHz)	–	50	50
Contact Pulse Length (ms)	–	4	–
^{1}H Spin-lock power (kHz)	–	50	50
Refocusing Pulse Width (μs)	–	16	–
Refocusing Pulse Power (kHz)	–	15.6	–

Table 2. NMR parameters used in the acquisition of ^{119}Sn SSNMR spectra.

	WURST-CPMG	CP-CPMG
Number of Transients	2,048	2,048
Recycle Delay (s)	4	2
Dwell Time (μs)	1	1
Spectral Window Width (MHz)	1	1
Number of Meiboom-Gill loops	50	50
Acquisition Time (ms)	10.8	8.6
^{1}H Continuous-Wave Decoupling Power (kHz)	35	50
WURST Pulse Length (μs)	50	–
WURST Sweep Range (kHz)	600	–
WURST Pulse Power (kHz)	28	–
Spin Echo Length (μs)	100	100
^{1}H Excitation Pulse Length (μs)	–	3.5
^{1}H Excitation Pulse Amplitude (kHz)	–	71.4
Contact Pulse Length (ms)	–	3
^{1}H Spin-lock power	–	50
Refocusing Pulse Width (μs)	–	7
Refocusing Pulse Power (kHz)	–	35.7

2.3 Results and Discussion

2.3.1 Optical & Structural Analysis of Cadmium Stannate

In Figure 11, characterization data is provided for highly faceted octahedral CTO PSNCs achieved by adapting the method of Ye and co-workers.[103] The highly faceted CTO is prepared through the use of Sn(II) acetate as the precursor instead of Sn(IV) acetate to encourage formation of the inverted spinel by coupling the chemical reduction of Cd(II) → Cd(0) with concomitant oxidation of interstitial Sn(II) → Sn(IV). Evidence for nucleation and growth of CTO by formation of Cd metal but not CdO, Sn, SnO, or SnO_2 is evidenced by analysis of the isolated nanoparticles from the raw batch vs selective isolation of the Cd and the CTO by sequential centrifugation steps (Figure 12).

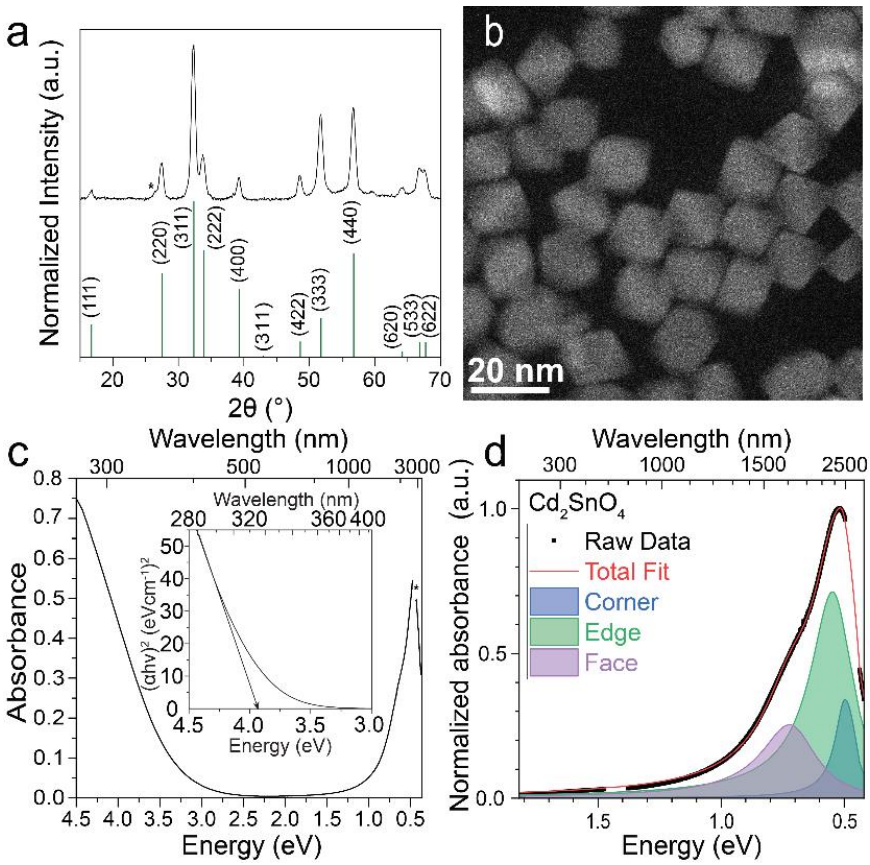

Figure 11. Optical and structural characterization of CTO nanocrystals. (a) pXRD of CTO PSNCs with corresponding inverse spinel Cd_2SnO_4 reflections. (b) HAADF-STEM of CTO PSNCs showing octahedron-like shape. (c) UV-vis-NIR absorption spectrum with a Tauc plot inset showing a calculated optical E_g of 3.89 eV. (d) Extinction spectrum of the LSPR fitted to a 3-mode simplified Drude approximation illustrating the corner, edge, and face contributions.

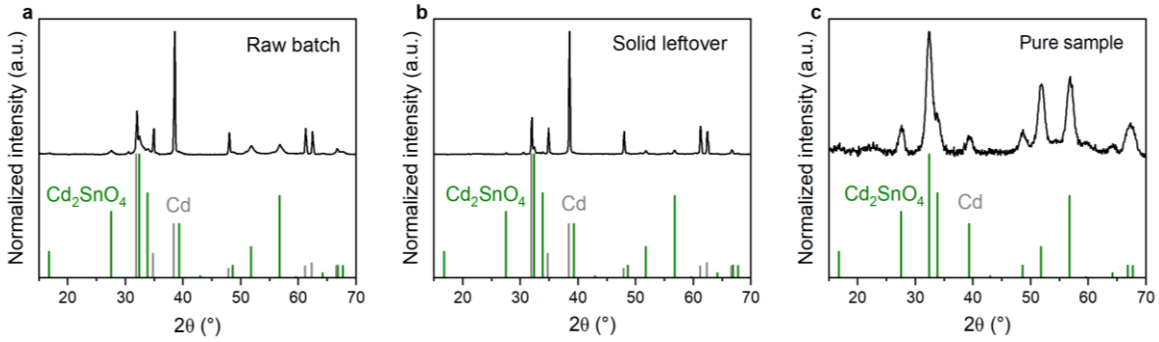

Figure 12. (a) pXRD pattern for initial isolation of all nanocrystals from the reaction mixture. (b) Selective isolation of Cd metal from the reaction mixture via centrifugation at 3000 RPM, and (c) isolation of Cd_2SnO_4 line phase by addition of IPA to the supernatant followed by centrifugation 6000 RPM

The Sn(IV) and Cd(II) oxidation states in the CTO sample, following Ar^+ beam sputtering to remove surface ligands, are confirmed by X-ray photoelectron spectroscopy (XPS) (Figure 13).

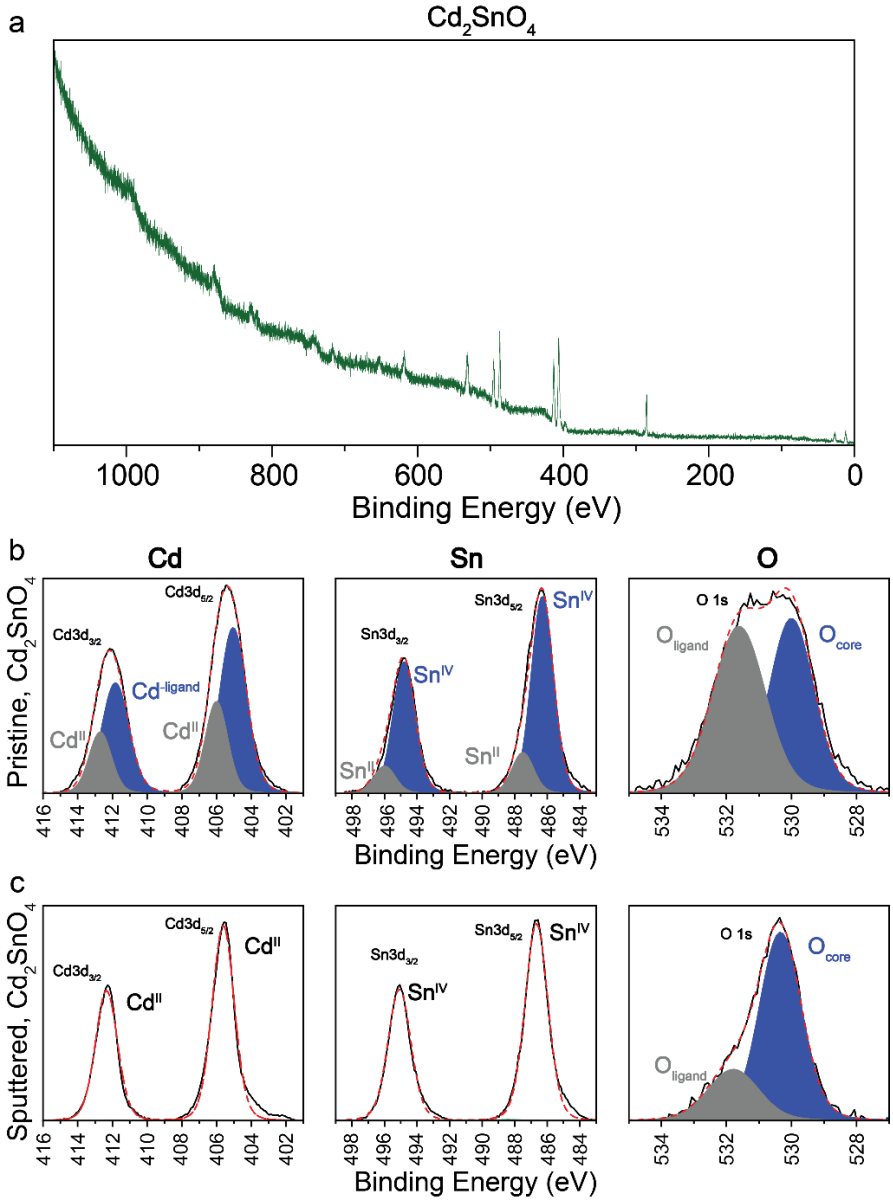

Figure 13. XPS data of CTO nanocrystals. (a) XPS survey scan for CTO nanocrystals from 0 to 1200 eV. The CTO nanocrystals were Ar^+ sputtered for 5 min to remove ligand. XPS data focusing on Cd $3d_{3/2}$, $3d_{5/2}$; Sn $3d_{3/2}$, $3d_{5/2}$; and O 1s areas of Cd_2SnO_4 before (b) and after sputtering (c). The Cd $3d_{3/2}$, $3d_{5/2}$ XPS shows a prevalent Cd signal assigned to Cd(II) (413 eV) and Cd-ligand (412 eV) which later disappears after sputtering. The Sn $3d_{3/2}$, $3d_{5/2}$ XPS data before and after sputtering suggests that there are leftover Sn(II) (496 eV) species, most likely unoxidized Sn(II) ligands at the NC surface. The lower intensity 532 eV O 1s signal after sputtering signifies the removal of carboxylate ligands, which is commonly observed after the sputtering process.

Table 3. Elemental % of Cd and Sn from EDS analysis on CTO NCs. Different areas analyzed on the same sample.

Measurement #	Cd %	Sn %	Cd/Sn ratio
1	63.16	36.84	1.71
2	57.84	42.16	1.40
3	64.01	35.99	1.78
4	64.39	35.61	1.81
5	61.65	38.35	1.61
6	61.13	38.87	1.57

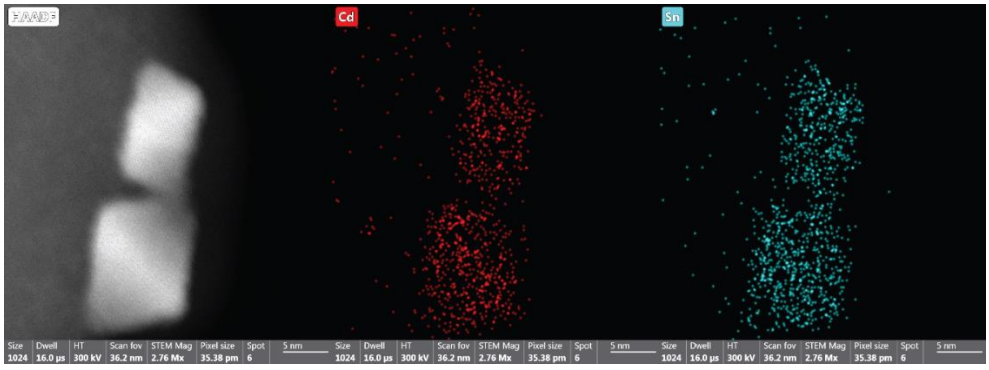

Figure 14. HAADF-TEM of CTO NCs and corresponding EDS images of Cd and Sn distributions on two different size particles

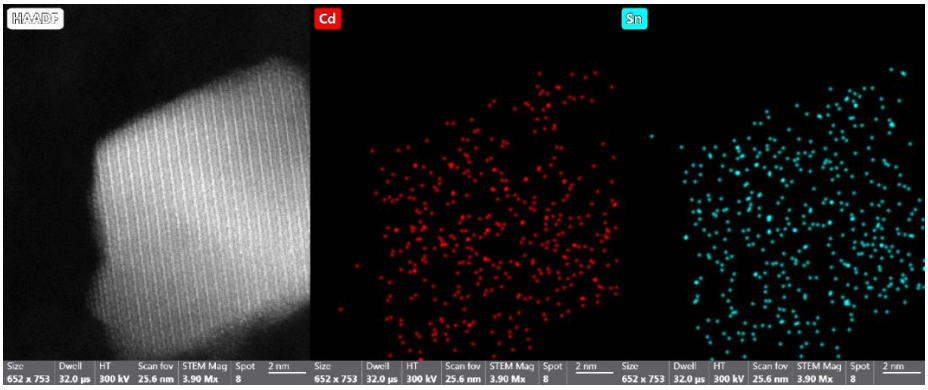

Figure 15. HAADF-TEM of single CTO NC (left) and corresponding EDS images of Cd and Sn atom distributions.

The reaction drives efficient formation of the desired CTO inverted spinel line phase with higher reproducibility than the previously described route. The Cd to Sn ratio of the isolated

CTO nanocrystals measured by energy dispersive X-ray spectroscopy (EDS) analysis is 1.0:1.2, leading to an average composition of $Cd_{1.86}Sn_{1.14}O_4$ (Table 3, Figure 14, and 15). The isolated oleic acid-passivated colloid that is emerald green in color (Figure 16).

Figure 16. Picture of CTO PSNC solution in TCE (left) showing emerald color compared to a less soluble NC solution (right) demonstrating the difference in scattering between the two solutions.

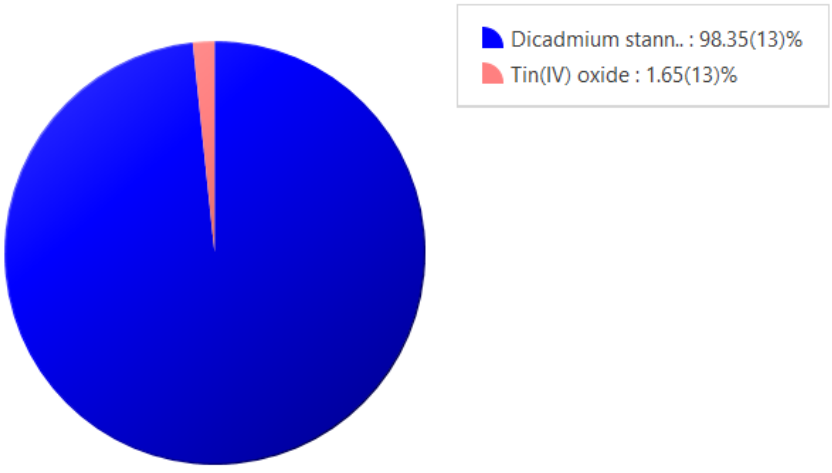

Figure 17. Whole-powder-pattern fitting (WPPF) results of CTO PSNCs using the inverse spinel structure (calc. PDF 01-080-1468) and the SnO_2 rutile structure.

In Figure 11b, pXRD data is shown for the CTO PSNCs compared to the PDF 01-080-1468 card for cubic CTO inverse spinel, where * indicates the presence of trace SnO_2, <1.5% based on whole-powder-pattern fitting analysis (Figure 17). In the pXRD pattern the (111) reflection is clearly observed in the isolated CTO samples consistent with a high degree of crystallinity and/or a high degree of faceting on the isolated CTO PSNC samples. In Figure 11b, high-angle annular dark-field scanning transmission electron microscopy (HAADF-STEM) images of the ensemble of CTO PSNCs clearly show an octahedral topology, with an octahedral aspect ratio of 1.30 and dimensions of 18.9 nm (long) × 14.5 nm (short) (Figure 18 and 19). The long axis has an 8% length distribution with an 11% width distribution along the short axis.

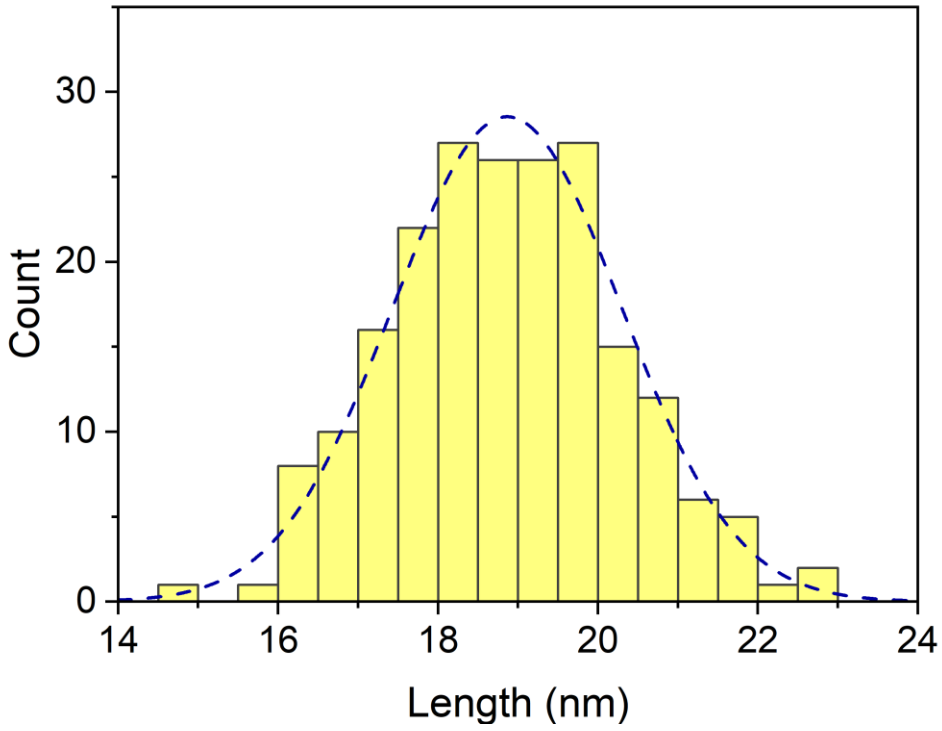

Figure 18. Histogram measuring the tip-to-tip length of CTO PSNCs with an average size of 18.9 nm with an 8% size distribution.

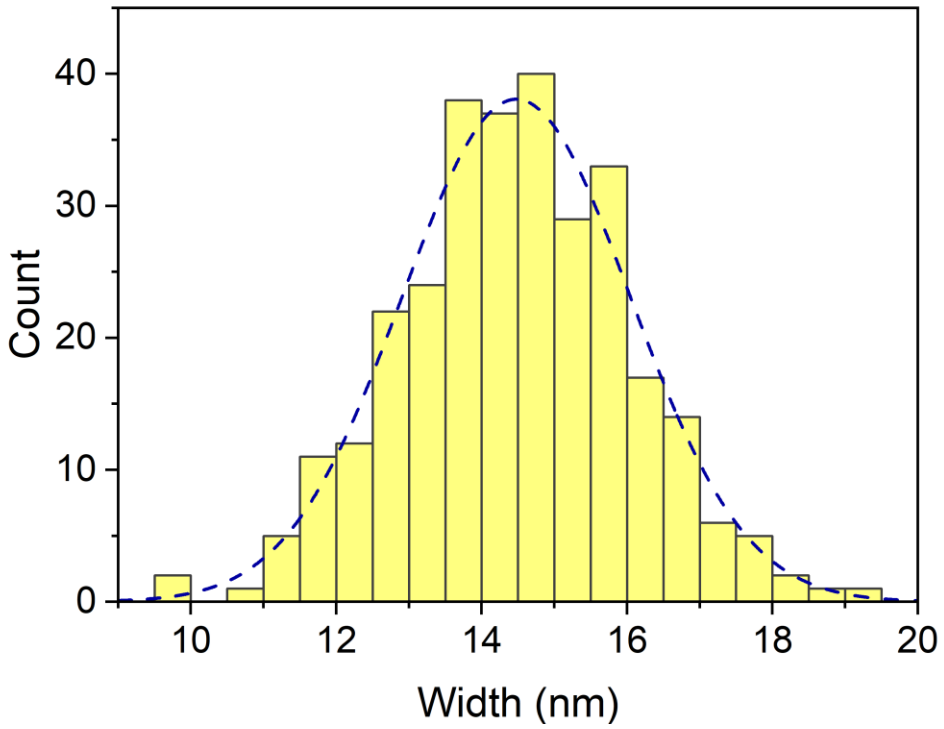

Figure 19. Histogram measuring the width of CTO PSNCs with an average size of 14.5 nm with an 11% size distribution.

The quality of the octahedra can be assessed by high HAADF-STEM images in Figure 11b and Figure 20. The isolated CTO PSNCs form as highly faceted 19 ± 2 nm octahedra, exhibiting truncated vertices along the z-direction. In Figure 20a, tilt-dependent images (+30°, 0°, –30°) confirm the truncated octahedral morphology assignment. In Figure 20b, two adjacent CTO PSNCs are observed demonstrating different morphology depending upon orientation. High resolution and tilt-dependent HAADF-STEM allows the lattice fringe patterns to be indexed to the (220) ($d_{(220)}$ = 3.24 Å), (222) ($d_{(222)}$ = 2.65 Å) and (111) ($d_{(111)}$ = 5.30 Å) planes. A facet angle of 109.5° is measured for the PSNC facet edges, consistent with the expected dihedral angle for octahedral morphology. The HAADF TEM can be directly compared to a 3D atom reconstruction (Figure 20 c-f) for CTO imaged as top down along the z-direction, (001) facet, and laying on a (111) facet for the octahedra tilted on their sides. The presentation of the large (111) facet in a controlled PSNC growth condition is expected, as the (111) facet in CTO is the lowest energy surface for the cubic spinel structure.[162] The implementation of Sn(II) as the

reactant to control Cd reduction appears to regulate CTO growth rates, allowing well-faceted octahedral PSNCs to be isolated, which has not been previously reported.

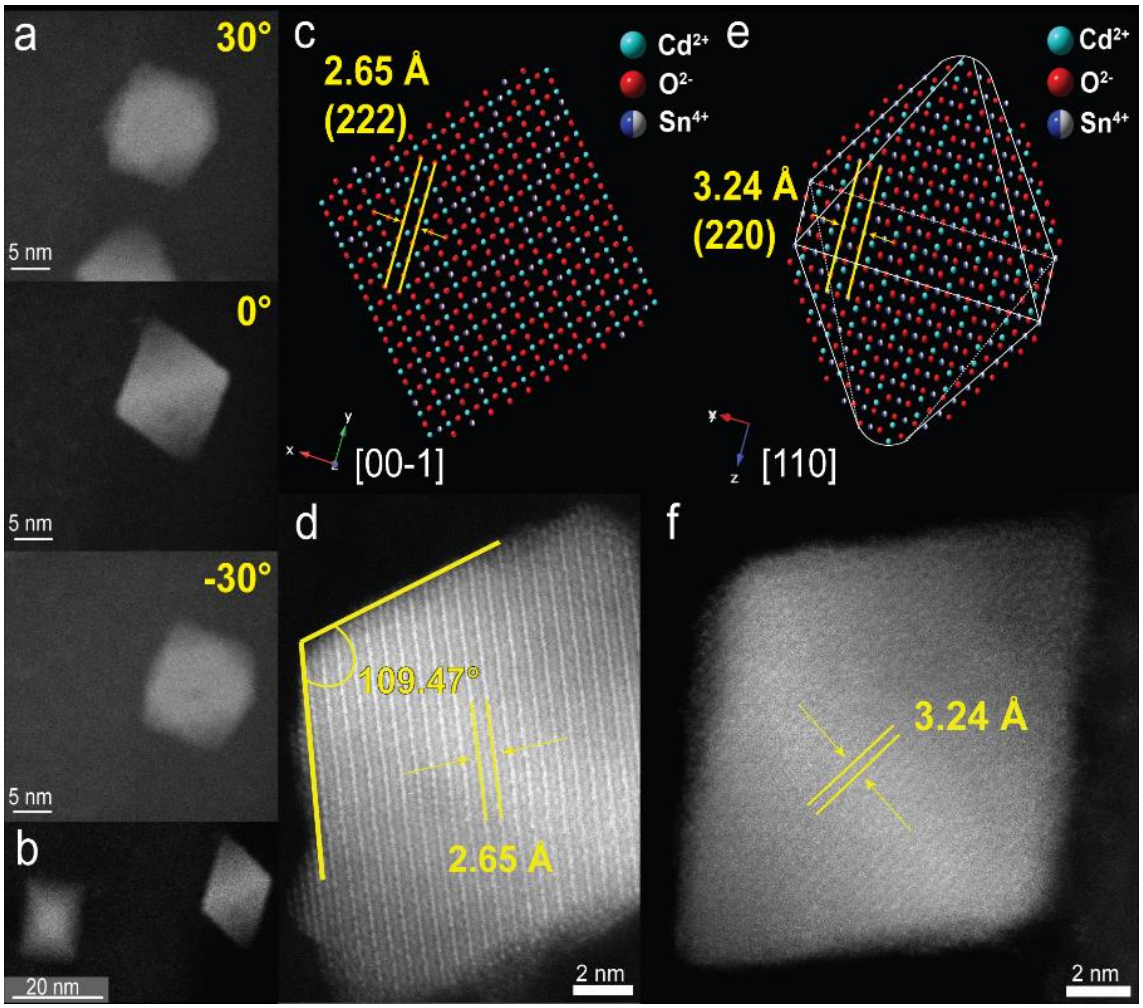

Figure 20. HAADF-STEM experiments of CTO PSNCs. (a) Tilting images at 30°, 0°, and –30° probing different NC orientations showing octahedron-like shape. (b) Two neighboring NCs expressing different morphologies depending on the NC orientation relative to the electron beam. (c,d) Simulated and HAADF-STEM of CTO PSNCs showing *d*-spacing of 2.65 Å (222). An obtuse angle of 109.47° is drawn to illustrate the dihedral angle for an octahedron shape. (e,f) Simulated and HAADF-STEM of CTO NCs showing *d*-spacing of 3.24 Å (220).

In Figure 11c, the E_g absorption and LSPR extinction spectra are plotted. The intense emerald color of the CTO is assigned as arising from the SWIR (short wave infra-red) LSPR extinction. The observed absorption edge in the optical spectra at > 3.0 eV (333 nm) is assigned to the onset of E_g, while the feature at 0.47 eV (2638 nm) is assigned to the LSPR. In Figure 11c inset, a Tauc plot is plotted to yielding an E_g = 3.89 eV (319 nm), which is in good agreement

with previously reported values for spherical CTO NCs (E_g = 3.81 eV) and thin films (E_g = 3.60 eV).[163]

The LSPR exhibits three modes, with peaks at 0.73 eV (1698 nm), 0.55 eV (2264 nm), and 0.50 eV (2480 nm) that are attributed to face, edge, and corner contributions to the LSPR, respectively, as seen in Figure 11d.[20,6] The distinct modes are expected based on the octahedral shape observed by TEM, leading to the separation of the LSPR into three different modes corresponding to the face, edge, and corner contributions. While the tip and face contributions of the LSPR are usually observed experimentally, the edge is typically observed only in theoretical models.[115,164,165] The face, edge, and corner contributions to the LSPR yield quality factors (Q-factor) of 3.00, 2.98, and 4.70 respectively, comparing well with reported values for ITO and ICO.[166,167] The previously reported Q-factor for spherical CTO PSNCs is 1.92.[103] The volume corrected LSPR extinction scales with $n^{2/3}$.[168] Following the procedure of Jain et al.,[168] the volume corrected extinction value for CTO is 9.67 μm^{-1} (10^{19} carriers cm^{-3}). For comparison, extinction values between 15 and 55 μm^{-1} are reported in ITO for carrier densities of ~10^{20} carriers cm^{-3}, while $Cu_{2-x}Se$ (~10^{21} carriers cm^{-3}) has an extinction of 23.50 μm^{-1}.[64]

The assignment of the 0.5-0.73eV feature to a LSPR is supported by a dielectric solvent shift study, with an extracted sensitivity of 5.29 × 10^6 nm^2/RIU^2 (Figure 21), which is the same order of magnitude observed in ITO PSNCs.[115] The observed sensitivity reflects changes in solvent refractive index, which correlates with PSNC depletion layer thickness and doping concentration.[169]

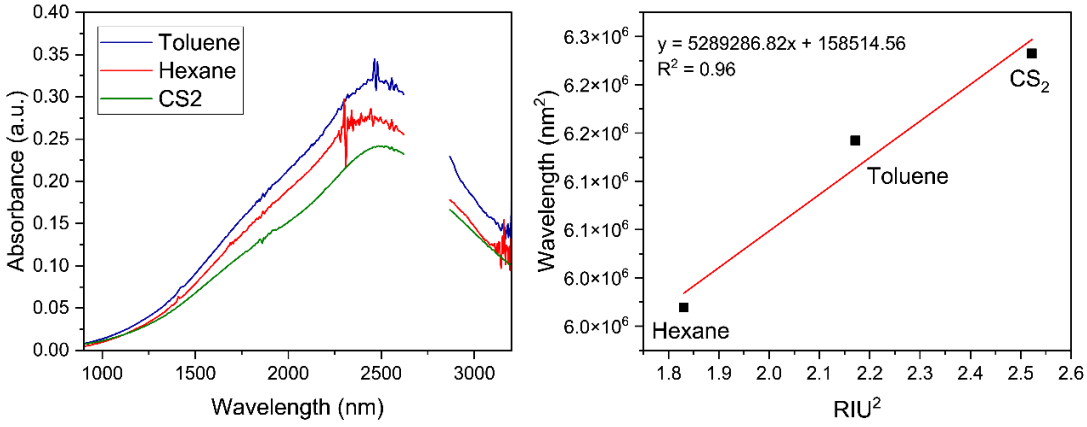

Figure 21. LSPR NIR extinction spectra of CTO NCs (left) in toluene, hexane, and carbon disulfide (CS_2). The wavelength squared is plotted against the squared solvent refractive index (RIU) (right). The plot demonstrates the linearity of LSPR frequency as a function of solvent dielectric. A LSPR sensitivity of 5.29 x 10^6 nm^2/RIU^2 is obtained from the slope of the linear fit.

The change in UV-VIS-NIR LSPR and E_g features following chemical titration of a micromolar CTO trichloroethylene solution by the one-electron oxidant, $NOBF_4$, is shown in Figure 22. Fitting of the LSPR frequency shift as a function of $NOBF_4$ concentration to a linear function [linear portion < 3 µmol] provides confirmation of the LSPR assignment and an estimate for the concentration of $NOBF_4$ for total carrier titration by extrapolation. It is important to note that use of strong oxidants does not allow accurate assessment of carrier density in a PSNC, since $NOBF_4$ is known to oxidize not only the introduced carriers, but also surface states and compensation centers in PSNCs.[107,170]

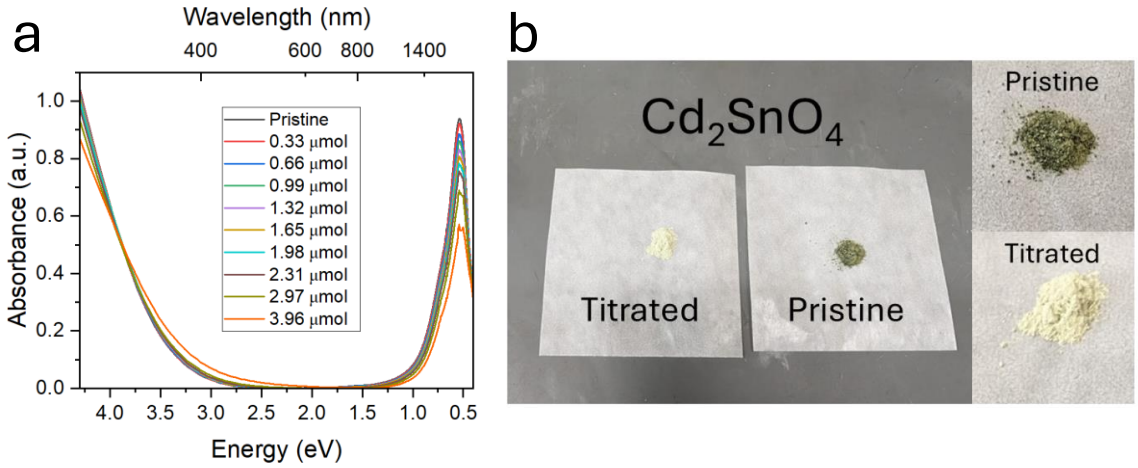

Figure 22. Chemical titration of Cd_2SnO_4 solution (a) to evaluate carrier density. The change in UV-Vis-NIR spectra for the LSPR and E_g on a Cd_2SnO_4 solution (~7.5 mg in 3 mL TCE) in a 1 mm NIR optical cell is shown. A shift in frequency and decrease in LSPR intensity is observed with increasing $NOBF_4$ concentration. The LSPR frequency decreases linearly with $NOBF_4$ concentration up to 2.97 mmol $NOBF_4$, followed by precipitation of the Cd_2SnO_4. Fitting of the chemical titration yields a slope of -0.0051, and a x-intercept of 110 µmol corresponding to full carrier titration. (b) The SSNMR sample (110 mg) prior to titration, where the green color arises from LSPR, and following titration (white powder) with excess $NOBF_4$ added.

The observed band edge shift with increasing occupation of Sn_{Cd} on the Cd_{Oh} site can be interpreted by inspection of density functional theory (DFT)-derived density of states (DOS) for CTO with varying Sn occupation (Figure 23). In the DOS, the valence band (VB) is comprised primarily of O 2*p* orbitals, while the CB is a mixture of Cd 5*s* and Sn 5*s* orbitals. As the concentration of Sn_{Oh} (Sn_{Cd}) in $(Cd_{1.00})_{Td}(Cd_{1.00-x}\ Sn_{1.00+x})_{Oh}$ increases from x = 0 to x = 1, both VB and CB energies decrease with respect to the E_F. It is also important to note that in the CB, the ratio of Cd to Sn 5*s* orbitals change as expected as a function of Sn incorporation. For the

pristine structure (Cd_2SnO_4), the Cd 5*s* contributions dominate the CB in comparison to the Sn 5*s* orbitals. When the Sn concentration increases to yield the $Cd_{1.5}Sn_{1.5}O_4$ structure, the Sn 5*s* orbitals become the main contributors to the CB DOS. As the concentration of Sn further increases leading to the formation of the $CdSn_2O_4$ structure, the conduction band (CB) is predominantly formed by Sn 5*s* orbitals, with a minimal contribution from Cd 5*s* orbitals. Inspection of Figure 23d illustrates the calculated optical E_g for the experimental stoichiometry $(Cd_{1.00})_{Td}(Cd_{0.86}\ Sn_{1.14})_{Oh}$ with a value of 3.84 eV in good agreement with the experimentally obtained optical E_g of 3.89 eV from Tauc plot analysis in Figure 11c.

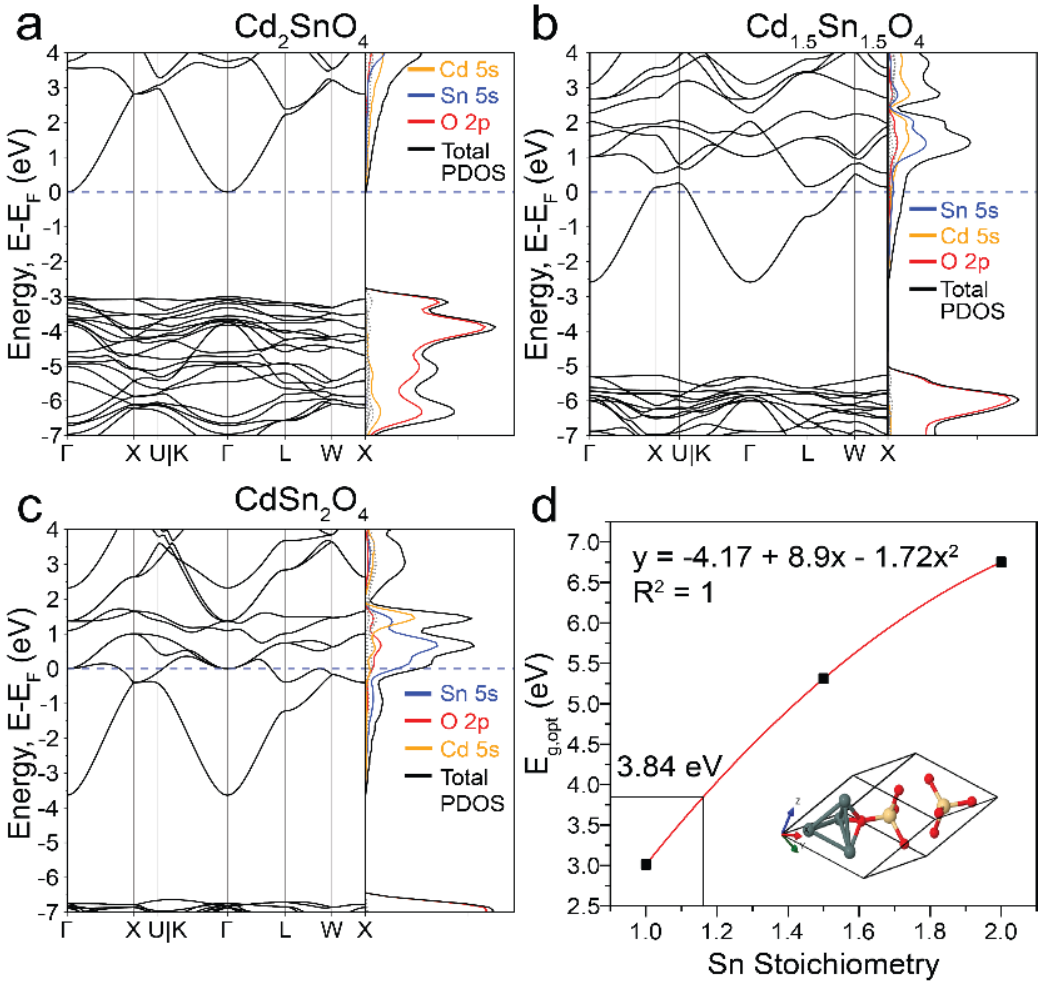

Figure 23. Overall density of state (DOS) and detailed orbital makeup of (a) Cd_2SnO_4, (b) $Cd_{1.5}Sn_{1.5}O_4$, (c) $CdSn_2O_4$. (d) Quadratic fit of the optical band gaps calculated from the DOS as a function of Sn stoichiometry with an inset showing the representative unit cell for $Cd_{2-x}Sn_{x+1}O_4$ used for calculations. The fit yields an optical band gap of 3.84 eV for a NC with a $Cd_{1.86}Sn_{1.14}O_4$ composition.

2.3.2 Evaluation of *n* and *m** in Cadmium Stannate

While *n* can be estimated from Drude model fits, this requires m^* to be known. The value of *n* is evaluated by fitting the observed plasma frequency (ω_p) to the Drude model, such that $\omega_p \propto \sqrt{(n/m^*)}$. The Drude model requires m^* to be assumed constant with size and defect densities, which has implicit bias, or experimentally measured. Assuming A-term behavior, (MCD) can be used to extract m^* from the Zeeman splitting energy (E_z) of the LSPR extinction due to the cyclotron resonance phenomenon (Equation 1 and 2).[171–173] Combining the selection rules of left- and right-circularly polarized (LCP, RCP) light with a rigid-shift approximation, the cyclotron resonance effect experienced by free carriers is used to extract E_z and m^* for LSPR free carriers,

$$E_z = \omega_B^{RCP} - \omega_B^{LCP} \quad (9)$$

$$\omega_B^{LCP/RCP} = \omega_0 \pm \frac{qB}{2m^*} \quad (10)$$

where ω_B is the field dependent plasma frequency, ω_0 is the field independent plasma frequency, *q* is the elementary charge, *B* is the applied magnetic field, and m^* is the effective mass of an electron. The charge carrier (*e*– vs. *h*+) is determined from the effective charge (*q*) observed in the signage of the ΔA spectrum (MCD intensity). While measuring the LSPR is more accurate, Radovanovic and coworkers showed that E_z, and subsequently m^*, can be evaluated by performing MCD on the E_g band edge, reflecting that a Burstein-Moss shift of the band edge (ΔEBM) occurs due to E_F changes directly associated with LSPR free carriers ($\Delta E^{BM} = (E_g^{CTO} - E_g^0) \propto \frac{n^{2/3}}{m^*}$).[174] In Equation 9 and 10, the *n* dependent band edge shift can be related to the value of m^* by considering the magnetic field dependent shift in the band gap E_g^{LCP} vs. E_g^{RCP} absorption or E_z. For the n-type semiconductor, only E_g RCP is observed (as has been previously reported) and is consistent with delocalized free electrons expected from LSPRs,[175]

$$E_z = E_g^{CTO\,LCP/RCP} = E_g^{CTO} \pm \frac{qB}{2m^*} \quad (11)$$

$$m^* = \frac{qBc}{2\pi(E_z)m_e} \quad (12)$$

thus, the field-dependent shift relative to the linear absorption E_g value (σ) allows E_Z to be estimated ($E_Z = 2\sigma$). Using the rigid-shift approximation, experimental linear absorption and MCD spectra are combined to extract E_Z and calculate m^* using equation 12.

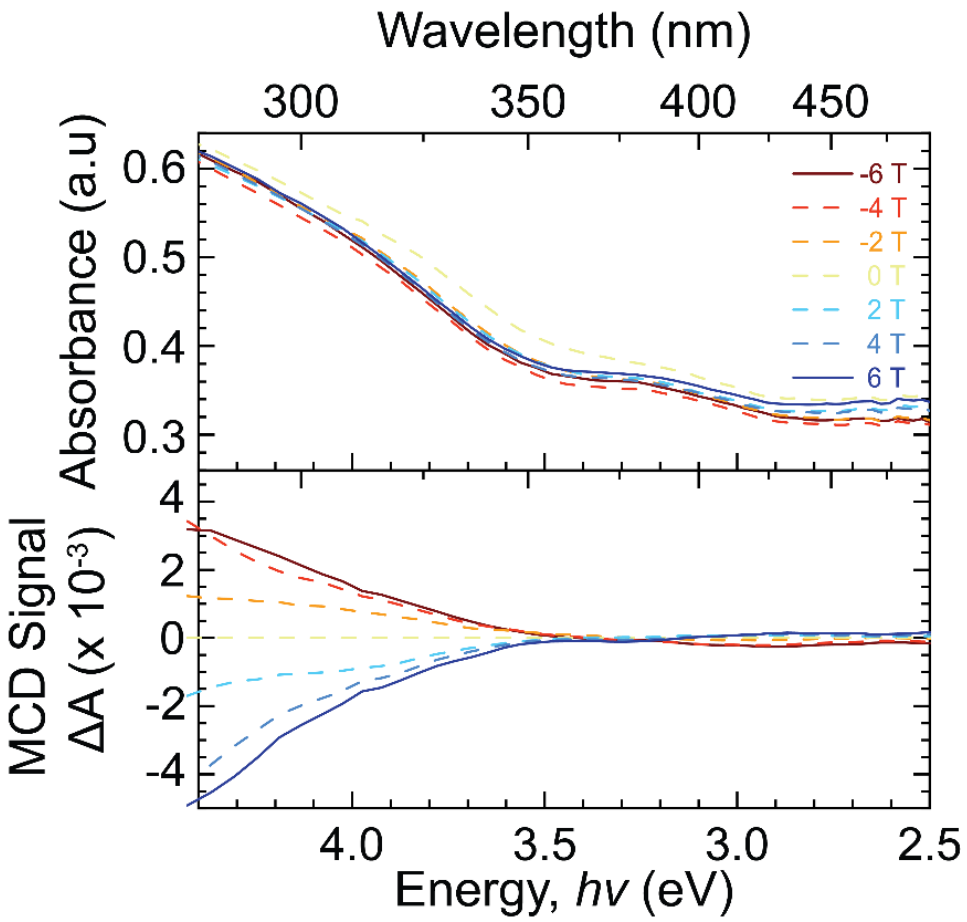

Figure 24. Dropcasted Cd_2SnO_4 on quartz substrate was measured through magnetic field dependent extinction (top) and VH-MCD spectroscopy (bottom) of the E_g band edge respectively

In Figure 24, variable field (VH)-MCD spectra measured at 40 K from +6 to –6 T are shown for drop cast CTO PSNC samples deposited from TCE onto a quartz substrate. The MCD ΔA spectra are plotted as LCP minus RCP for both 0 T to 6 T and 0 T to –6 T. The collection of data at ± 6 T allows background rejection and improves signal-to-noise, reflecting the inversion of ΔA. In the linear absorption spectra for the drop cast sample, two absorption features in the band gap region are identifiable: a UV continuum region beginning at 3.50 eV assigned to the E_g edge, and a broad, weak feature at 3.22 eV. Only the E_g edge is observable in solution for the sample, as previously reported.[7] The broad, weak absorption feature at 3.22 eV observed in the thin film has been previously reported but not assigned in literature for CTO thin films[176,177] and

other n-type inverse spinel structures such as Zn_2SnO_4.[178] The origin of this feature likely arises from either a V_O population leading to a donor state near the band edge or a surface bound Sn(II) complex to Sn(IV) charge transfer, as Sn(II) is observed as part of the surface passivating layer by XPS (Figure 13). Further studies are underway to assign the feature which is only observable in the thin film configuration.

In Figure 24, negligible magnetic field dependence for the linear absorption spectra is observed. Using the linear absorption and MCD data from Figure 24 and equation 12, m^* is calculated to be 0.022 ± 0.004 consistent with a report on doped CTO thin films.[128] In Equation 13 and 14, an alternative approach to extract m^* suggested by Gamelin and coworkers uses the Gaussian width and height of the linear absorption band edge (σ and A_0) and the MCD intensity ($\Delta A'$).[179] E_z is extracted from the MCD spectra, where $\Delta A'$ is obtained at an energy $E = (E_0 + \frac{\sigma}{\sqrt{2}})$ eV away from the Gaussian center (E_0).

$$E_Z = \frac{\sqrt{2e}}{2}\sigma\frac{\Delta A'}{A_0} \tag{13}$$

$$(E) = A_0 \exp\left(-\left(\frac{(E-E_0)}{\sigma}\right)^2\right) + y_0 \tag{14}$$

The value of E_z approximated by comparing MCD signal intensity to linear absorption peak properties obtained from a simple Gaussian fit yields an m^* of 0.020 ± 0.005, which is within statistical agreement with results obtained from the first method. The extracted values of m^* are comparable to those obtained by EELS for n-type CTO thin films, where m^* was calculated to be 0.02765 at the bottom of the CB.[128] While the results in this work show lower m^* than previously thin film results, it is not unreasonable due to the high crystallinity, symmetry perturbation, removal of observable V_O, and well-shaped PSNC morphology.[180]

The evaluation of m^* allows a value of n to be calculated from the Drude model by fitting the extinction spectra with $0.022m^*/m_e$ using a 3-mode simplified Drude model to account for the octahedral shape (Figure 11d). The three-mode SDA model provides an average $n = 5.19 \times 10^{19}$ carriers cm^{-3}. For completeness, comparisons were made for the 3-mode simplified Drude Model (3-SDA); single mode SDA (1-SDA); the simplified, extended Drude approximation (SXDA), which takes into consideration the LSPR dampening terms. The fits are in good agreement with the average carrier density calculated through the 3-mode model with the single mode SDA has a value of 3.56×10^{19} carriers cm^{-3}, and the SXDA has a value of 3.55×10^{19} carriers cm^{-3}. The

fitting parameters are available in Table 4.[181] As a final note, consistent with earlier reports in MO_x PSNCs, chemical titration of CTO with $NOBF_4$ is non-linear, yielding an overestimated n of 1.68 x 10^{22} carriers cm^{-3} (Figure 22). The titration experiment in this work supports the earlier conclusion by Milliron and coworkers that chemical titration can yield unrealistic values for n due to untargeted oxidative damage.[107,170]

Table 4. Tabulated parameters from SDA, SXDA, and 3-SDA fits.

	N_e (cm^{-3})	%Vol Fraction	ω_p (cm^{-1})	Γ_L (cm^{-1})	Γ_H (cm^{-1})	Γ_X (cm^{-1})	Γ_W (cm^{-1})
SDA	3.56 x 10^{19}	0.0104888	12039.4	2501.06	N/A	N/A	N/A
SXDA	3.55 x 10^{19}	1.05E-02	12033.5	2629.09	100	15817.5	1741.46
3-SDA							
Peak 1 (corner)	3.95 x 10^{19}	0.00195873	12692.5	769.571	N/A	N/A	N/A
Peak 2 (edge)	4.81 x 10^{19}	0.00741325	14000	1696.03	N/A	N/A	N/A
Peak 3 (face)	8.36 x 10^{19}	0.00197831	18466.7	2213.23	N/A	N/A	N/A

N_e, carrier concentration; ω_p, plasma frequency; Γ_L, low frequency damping; Γ_H, high frequency damping; Γ_X, crossover region; Γ_W, crossover width.

2.3.3 SSNMR Analysis of Charge Carriers

SSNMR spectroscopy provides resolution of atomic sites within a semiconductor nanocrystal,[182] where the observed frequency shift of the nucleus is dependent upon the site's coordination number, bonding (e.g., crystal field), and oxidation state. In the case of diamagnetic samples, this is reported as the chemical shift (CS). It is anticipated that as carrier densities increase in PSNCs, charge carriers will become metallic-like above the Mott threshold.[183,184] The onset of metallic-like character can generate observable Knight shifts (KS) in the SSNMR spectra.[149] The KS is a shift of the resonant frequency that occurs because of a local magnetic field produced at the nucleus due to the induced magnetization of conduction electrons. The magnitude of the KS is determined by several factors, including the DOS at the E_F, the local electron density, the nucleus, and the hyperfine coupling constant.[185] An increased number of electrons in the CB *s* orbitals tend to increase Knight shifts, since they have an increased probability of being located near the nucleus (increasing hyperfine interactions) and they tend to increase the DOS due to CB broadening and E_F contributions. Evidence for metallic behavior can be extracted from SSNMR measurements as KS $\propto \chi_s$, where χ_s is the electron spin susceptibility ($\chi_s \propto n^{1/3}$).[186]

Previous studies on PSNCs have reported small KS shifts in SSNMR spectra that are correlated to carrier density. For instance, Millstone and coworkers reported a KS and observation of the Korringa relationship for plasmonic $Cu_{2-x}Se$ PSNCs.[187] Additionally, Milliron and coworkers also described a KS for F:In_2O_3 PSNCs,[76] and the Strouse group reported a slight NMR frequency shift in ITO PSNCs.[69] A ^{113}Cd SSNMR study of bulk samples of CTO by MacKenzie and coworkers led to speculations that ^{113}Cd spectra had contributions from both KS and CS due to free electrons in the CTO samples.[188] It was suggested that the CS in the different CTO samples will be proportional to the conductivity, yet no correlation was observed between this and the apparent Knight shifts.[188] Finally, direct observations of KS have been reported for noble metal nanoparticles and bulk narrow gap (E_g < 2.5 eV) semiconductors.[189–192] Hence, the presence of a KS in the SSNMR spectra of PSNCs can provide evidence of free carriers; however, several factors are necessary for such observations, including a high *n*, low m^*, minimal magnetic susceptibility, and the presence of NMR-active isotopes.

In the cases of the CTO PSNCs, ^{113}Cd (S = ½) and ^{119}Sn (S = ½) SSNMR experiments can be used to measure potential KS, especially since the CBs of Cd and Sn have significant

contributions from their respective 5*s* orbitals, where plasmonic-free electrons are expected to reside (Figure 23). In Figure 25, ^{113}Cd and ^{119}Sn SSNMR spectra are shown for pristine CTO (i.e., not titrated) and titrated CTO PSNC samples. The former has conduction electrons, and the latter contains only a minimal or negligible number of carriers; as evidenced by the disappearance of the green color of the CTO powder after titration (Figure 22). Upon removal of free carriers by addition of $NOBF_4$, the LSPR is lost and E_g shifts to lower energy consistent with carrier removal (Figure 22). In addition, no difference in the pXRD patterns is observed for the pristine and titrated samples (Figure 26).

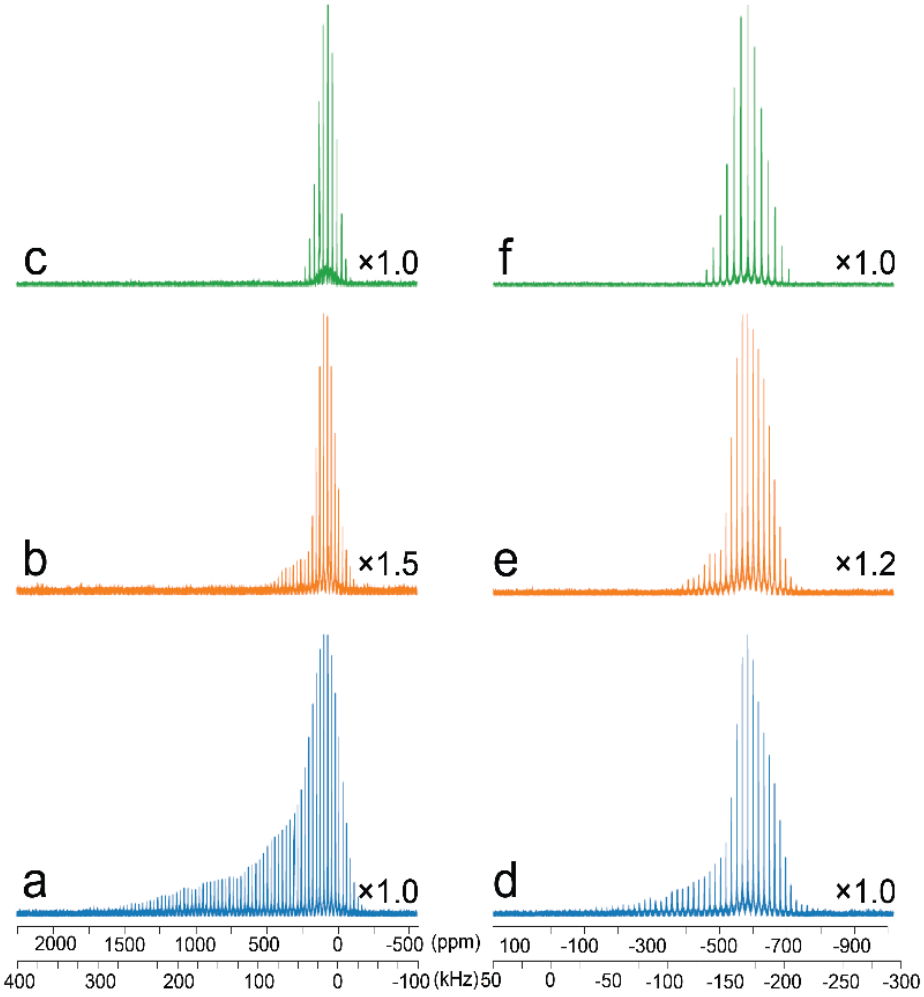

Figure 25. ^{113}Cd and ^{119}Sn NMR of pristine (a,d) and titrated (b,e) CTO nanocrystals collected using a WURST-CPMG pulse sequence. ^{113}Cd and ^{119}Sn NMR of pristine CTO samples (c,f) acquired using a CP-CPMG pulse sequence. All data acquired at 18.8 T under static conditions.

Comparison of the ^{113}Cd WURST-CPMG NMR spectra of stationary samples of the pristine (Figure 25a) and titrated (Figure 25b) CTO PSNCs exhibit distinct breadths of 345 kHz

(1940 ppm) and 115 kHz (640 ppm), respectively. Though the patterns share similar features on their low frequency ends, the much broader range of chemical shifts in the former is thought to arise from distribution of Knight shifts. Below, the rationale for this observation is explained by first considering the ^{113}Cd NMR spectra of the titrated samples (which in principle should have no conduction electrons), followed by those of the pristine sample.

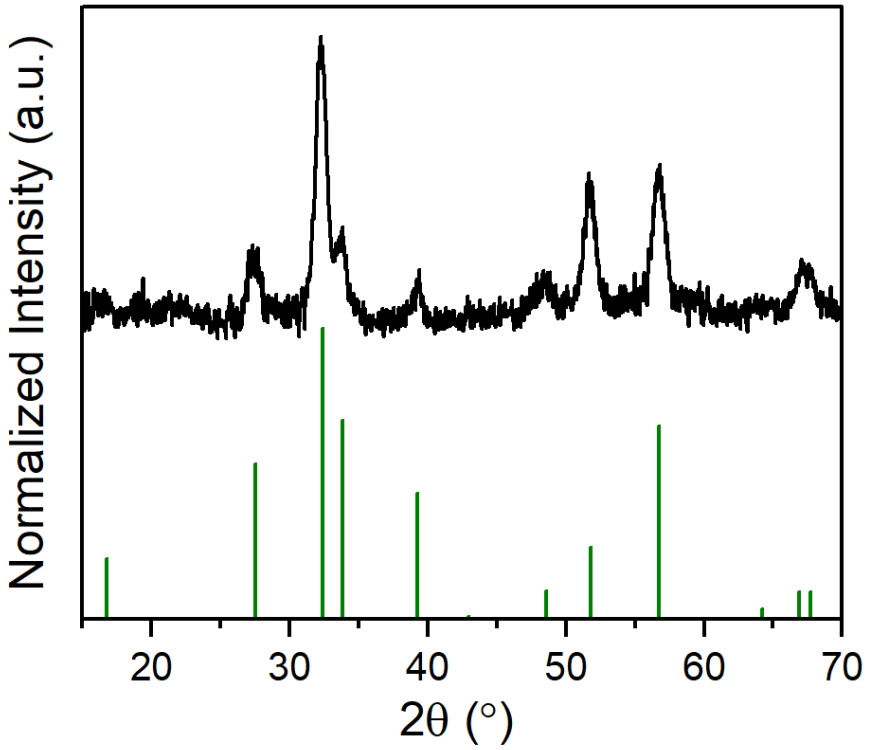

Figure 26. pXRD of CTO NCs after titration. The CTO NCs retain the inverse spinel pattern after titration consistent with no changes in structure.

The centers of gravity of the high- and low-intensity patterns for the titrated sample are at *ca.* δ_{CG} = 150 ppm and δ_{CG} = 225 ppm, respectively (Figure 25b). The distribution of chemical shifts arises due to the small size of the NCs, with Cd sites in their cores possessing shifts most resembling those of bulk CTO, and those near the surface having greater variation due to an increased number of defects and potential interactions with surface ligands.[182,193,194] On first sight, it is tempting to assign these two powder patterns to Cd sites with six-coordinate (Cd(O_h)) and four-coordinate (Cd(T_d)) environments, since these are known to have values of δ_{iso} ranging from 150 to –100 ppm[195] and from 80 to 800 ppm, respectively.[182,196] However, if this was the

case, both patterns would be visible in the corresponding ^{1}H-^{113}Cd CP-CPMG spectrum – in fact, only the pattern with δ_{CG} = 150 ppm is observed. This suggests that (i) the ^{113}Cd NMR patterns for the two sites in CTO may overlap in the static spectrum and (ii) the pattern with δ_{CG} = 225 ppm has some other origin.

This first point is addressed via examination of ^{1}H-^{113}Cd CP/MAS NMR spectra acquired with contact times of 3 and 8 ms (Figure 27). Two broad peaks at δ_{iso} = 86 and 46 ppm are clearly visible in each spectrum, with intensities that do not substantially change with different contact times. This suggests that these peaks do not arise from distinct chemical shifts of core and surface Cd species, since very different peak intensities would be observed for different contact times. One possibility is the tentative assignment of these peaks to the Cd(T_d) and Cd(O_h) sites, respectively (though quantum chemical calculations will likely be necessary to confirm this assignment). This assignment is provisional, since if Cd(T_d) sites are present, it is possible that they may have very long T_1 and/or very short T_2 values that prohibit their observation, which would require experiments of great lengths. It is also noted that high-frequency peaks arising from KSs are not observed in these CP/MAS spectra; this is in part to the extraordinarily low S/N that is often observed in MAS NMR spectra of ultra-wideline NMR patterns, and in part due to the inefficiency of CP transfer to the core of the PSNCs (18.9 nm by 14.5 nm dimensions) where the Cd sites impacted by KSs likely exist (*vide infra*).

The second point is addressed by first considering the attribution of the broadening in the ^{113}Cd NMR spectra of the pristine samples to KSs, as well as the magnitude and field dependence of the KS. The powder pattern in the static ^{113}Cd NMR spectrum of the pristine sample (Figure 25a) has a total breadth of *ca*. 345 kHz (1940 ppm), with its highest detectable shift at *ca*. 1740 ppm. The high frequency shift is far beyond the reported chemical shifts for non-metallic Cd compounds.[197] Furthermore, since the four- and six-coordinate Cd sites are extremely unlikely to lead to cadmium chemical shift anisotropies in excess of 300 - 400 ppm,[197] the broadening is attributed to a distribution of KSs. The maximum KS value is estimated by referencing to the ^{113}Cd secondary standard $Cd(NO_3)_2{\cdot}4H_2O$, $\nu_0(^{113}Cd)$ = 177.632 MHz which corresponds to δ_{iso} = –102 ppm with respect to the primary standard of 0.1 M $Cd(ClO_4)_2$ at δ_{iso} = 0 ppm).[195] From this, a maximum Knight shifted frequency of K_{iso} = 0.309 MHz (1740 ppm) yields the percent Knight shift as $\Delta K = K_{iso}/\nu_0(^{113}Cd) \cdot 100\%$ = 0.174%. This value is nine times the magnitude of that reported from ^{113}Cd SSNMR spectra of CdO (ΔK = 0.016%).[198] Additional

confirmation of the observation of a distribution of KSs is provided by comparison of ^{113}Cd WURST-CPMG NMR spectra acquired at 14.1 T and 18.8 T (Figure 28), since the magnitude of the KS is proportional to the magnetic field strength. The broadening attributed to KSs is more pronounced in the 18.8 T spectrum (spectra on the kHz scale have distinct breadths, whereas those on the ppm scale are identical), where the ratio of the maximum KSs is K_{iso}(18.8T)/K_{iso}(14.1T) = 306 kHz/230 kHz = 1.33, matching the ratio of the higher and lower field strengths.

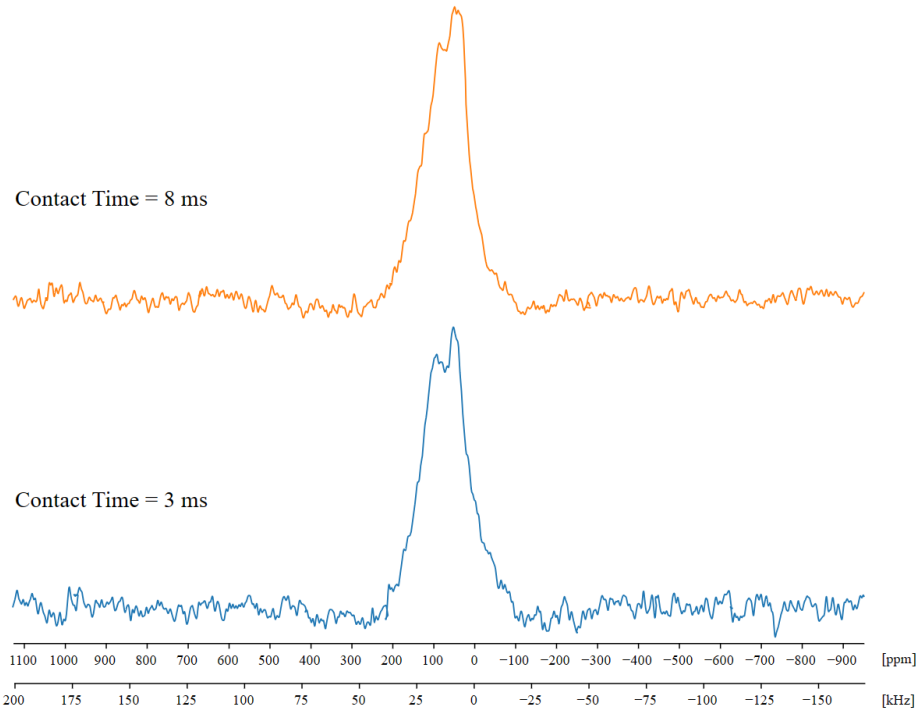

Figure 27. ^{1}H-^{113}Cd CP/MAS spectra of pristine Cd_2SnO_4 NCs acquired using different contact times (ν_{rot} = 15 kHz).

The contributions of atomic- and nano-level structure to the observed distribution of KSs are now considered. The range of the KSs is attributed to a distribution of distinct Cd environments, which vary in their nature from the core to the surface, by analogy to chemical shift distributions, *vide supra.* The dependence of the magnitudes of KSs in relation to the size and shape of NPs, locations of atoms within the NPs, and surface-ligand interactions is well known, especially for NPs comprised of conducting metals like Pt, Cu, and Ag,[81,143,199] allowing us to draw several tentative conclusions. The highest-frequency, Knight-shifted region of the pattern corresponds to nuclei of atoms in the core/interior of the PSNCs, since these are likely to have the most Cd 5s conduction electrons (due to a reduced number of defects). By contrast, Cd

sites near the surface, which are in the depletion region of the CTO, have reduced or negligible KSs due to the presence of vacancies, defects, interactions with ligands/solvents, and surface reconstruction arising from Cd-ligand passivation.[200] This is confirmed by ^{1}H-^{113}Cd CP/CPMG spectra (Figure 25c), where the ^{113}Cd signal arises solely from ^{1}H spin polarization transferred from the oleic acid ligands on the surface of the PSNCs, yielding a spectrum resembling that of the titrated sample (*cf.* Figure 25b). Hence, returning to the second point above, the absence of extreme broadening in the ^{113}Cd NMR spectrum of the titrated sample, along with the presence of a small "tailing" to high frequency, likely indicates a small distribution of KSs, perhaps arising from residual conduction electrons after titration.

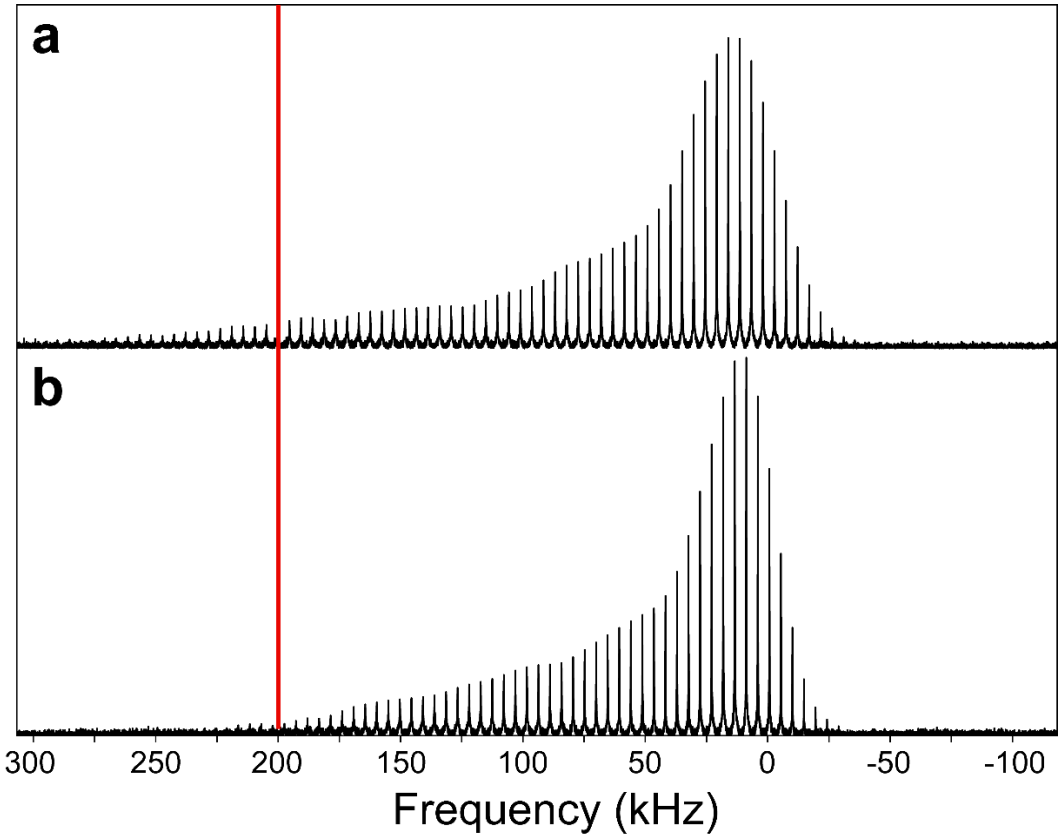

Figure 28. ^{113}Cd WURST-CPMG NMR spectra of CTO NCs at 18.8 T (a) and 14.1 T (b). Red line drawn (200 kHz) for better comparison of the field dependent tailing of Knight shifts.

The corresponding set of ^{119}Sn SSNMR spectra for the pristine and titrated CTO samples (Figure 25d, 25e) reveal pattern breadths of 215 kHz (720 ppm) and 107 kHz (360 ppm), respectively. Analogous to the ^{113}Cd spectra, the narrow, low-frequency portions of the ^{119}Sn patterns exhibit chemical shift distributions, with values of δ_{CG} = -580 ppm (from the titrated sample), corresponding to a single Sn(O_h) site.[80] Broadening in the ^{119}Sn WURST-CPMG spectra

attributable to a KS distribution is prevalent for the pristine samples (again, tin CSAs for six-coordinate sites are not expected to produce the degree of observed broadening.)[197] However, the degree of broadening is less than that in the corresponding ^{113}Cd pattern (*cf.* Figure 25a, 25d). In the case of the pristine CTO PSNC sample (Figure 25d), the observable signal with the highest Knight shift is at *ca.* –110 ppm. If $\nu_0(^{119}\text{Sn})$ = 298.471 MHz corresponds to the secondary chemical shift reference of δ_{iso} = 121 ppm of solid SnO (with respect to the primary reference of $SnMe_4$ at δ_{iso} = 0 ppm), the maximum Knight shifted frequency of K_{iso} = 32832 Hz (110 ppm), gives ΔK = 0.011% (significantly smaller than the ΔK observed in the corresponding ^{113}Cd NMR spectra). Finally, the ^{1}H-^{119}Sn CP-CPMG SSNMR spectrum (Figure 25f) reveals that the low-frequency end of the pattern largely corresponds to surface cites, in line with the analogous ^{113}Cd data (*cf.* Figure 25e), confirming that KS signals arise from ^{119}Sn nuclei in the cores of the PSNCs. It is noted that the ^{119}Sn NMR spectra reveal no evidence of Sn(T_d) sites (the δ_{iso} = –200 ppm for SnO, Figure 25d), which confirms the absence of Sn^{2+} oxide sites in the sample.[201]

A comparison of the KSs from the ^{113}Cd and ^{119}Sn SSNMR data infers of a higher number of free carriers in the CB from the Cd 5*s* orbitals than from those of the Sn 5*s* orbitals, especially given that the ratio of the ^{119}Sn and ^{113}Cd Larmor gyromagnetic ratios is $\gamma(^{119}\text{Sn})/\gamma(^{113}\text{Cd}) \approx 1.7$, which would imply larger frequency shifts for ^{119}Sn if the contributions were equivalent. The development of a quantitative relationship between the ΔK values and carrier densities is challenging and beyond the scope of the current work, since it is possible that there are nuclei experiencing even higher KSs, which also may result in rapid T_2 relaxation that would render them unobservable in CPMG-type experiments – though this could be addressed with variable-temperature measurements of KSs and T_1 values.

2.4 Conclusions

In this work, direct evidence for metallic-like carriers in highly-faceted, octahedral shaped CTO PSNCs are grown by high-temperature colloidal methods using a Sn(II) source. The use of Sn(II), which has not been previously reported for CTO, appears to control growth and nucleation in CTO, allowing reproducible isolation of highly faceted PSNCs with low densities of V_O defects. The octahedral shaped CTO exhibiting (111) faceting has a 1.30 aspect ratio. The

morphology of the PSNC leads to a 3-mode LSPR assignable to face, edge, and corner contributions of the dielectric function. The observation of a correlating band edge shift, attributed to carrier-induced Burstein-Moss behavior, corroborates the presence of free electrons in the CTO PSNC. Fitting the MCD for m^* allows the LSPR spectra to be fit to the Drude approximation. A value of n of ~10^{19} cm^{-3} with an m^* of $0.022m^*/m_e$ is extracted from the spectral data. The low m^* can be interpreted as electrons in the CB possessing higher mobility due to the absence of donor-acceptor states arising from non-carrier-contributing defects in the PSNC sample. The value of m^* is consistent with reports for CTO in thin films prepared by chemical vapor deposition.

The low m^* value suggests metallic like behavior for the n-type carriers in CTO, likely reflecting the low trap densities in the inverted spinel. The metallic character is confirmed by the observation of large Knight shifts for ^{113}Cd and ^{119}Sn SSNMR spectra. The differences in KS in the ^{113}Cd and ^{119}Sn spectra indicate that more free carriers originate from the Cd 5*s* orbitals than the Sn 5*s*, which is consistent with DOS CB calculations. The distributions of chemical shifts and Knight shifts in the ^{113}Cd and ^{119}Sn spectra of pristine and titrated samples suggest that the free carriers reside in the core of the PSNCs; this is reinforced by ^{1}H-^{113}Cd and ^{1}H-^{119}Sn CP/CPMG experiments, which yield signals corresponding only to Cd and Sn sites near or on the surface, none of which exhibit Knight shifts. The NMR results indicate surface ligation, and the presence of a surface depletion region may result in carrier damping. A comprehensive conclusion of the difference NMR results between the pristine and titrated samples can be found in Figure 29.

While CTO PSNCs are not new, the manuscript illustrates the importance of fully characterizing PSNCs to elucidate the carrier behavior in colloidally prepared plasmonic materials. The correlation of optical, structural, and computational methods suggests low V_O defect densities in the inverted spinel CTO grown by colloidal methods can lead to highly mobile free electrons. DFT calculations of DOS support the experimental results and illustrate that in CTO, Sn_{Cd} is the major contributor to carrier generation. The combination of MCD and UV-vis-NIR allow extraction of PSNC parameters without requiring the assumption of the value of m^*, with MCD also providing clear evidence of plasmonic and n-type behavior.

The NMR-resolved KS measurements represent some of the first examples of KS being observed in wide band PSNCs. SSNMR provides a powerful tool for structural and electronic

analysis of these materials that further support the presence of metallic-like electrons in the CTO system. Further studies are underway to elucidate size, aspect ratio, and antisite population effects, especially within the quantum confined regime where surface states may impact carrier mobility due to increased scattering contributions.

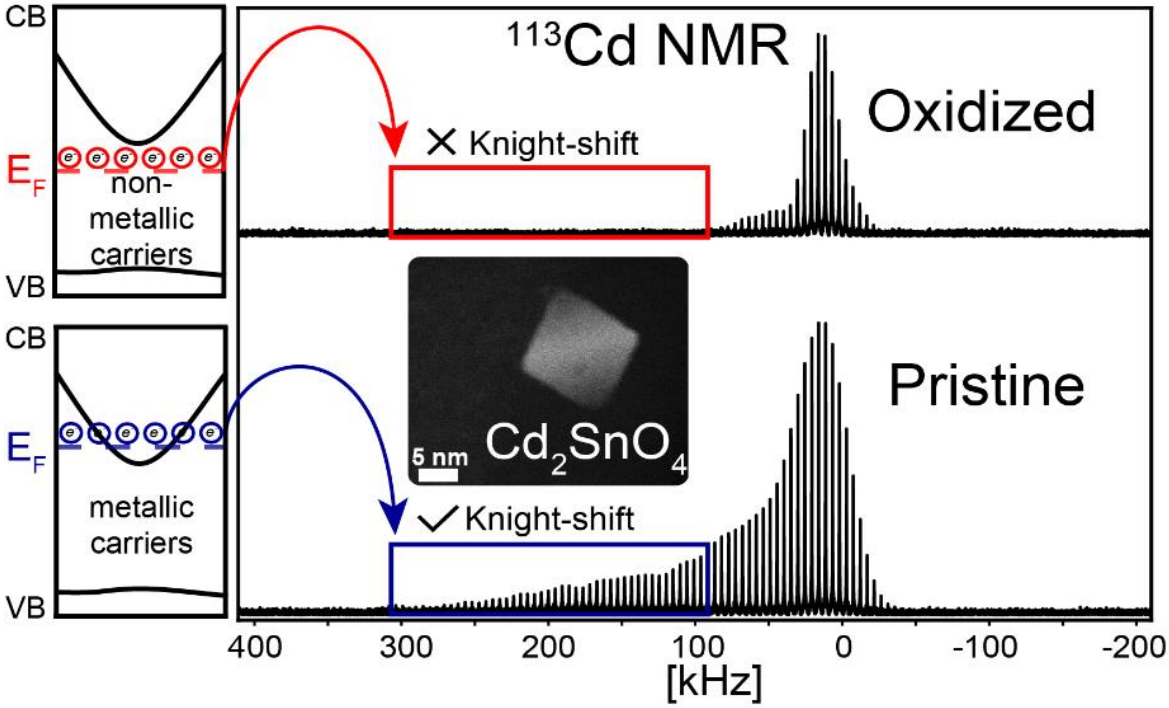

Figure 29. ^{113}Cd NMR spectra of the pristine and oxidized samples. In the pristine sample the E_F resides within the CB, which leads to a Knight-shift in the spectra due to the highly mobile metallic-like carriers. In the oxidized samples the carriers are removed, lowering the E_F, thus reducing the conductivity of the CTO leading to the removal of the KS part of the spectrum.

CHAPTER 3

DEFECT EVOLUTION IN CADMIUN-TIN-OXIDE PLASMONIC SEMICONDUCTOR NANOCRYSTALS

3.1 Introduction

The evolution of carrier properties in the tin-cadmium-oxygen (Sn-Cd-O) series plasmonic semiconductor nanocrystals (PSNCs) is investigated to understand the interplay of carrier parentage and extrinsic dopant site occupation on the evolution of metallic character (high mobility, low m^*, s-character). The experimental results on a well-controlled, highly crystalline system provides insight into Sn-Cd-O thin film semiconductor characteristics. MO_x PSNCs allow the role of V_O and M'_M to be evaluated in a highly faceted, size controlled, and shape dispersity system with controlled chemical composition. The plasma frequency (ω_p) plasmon frequency (ω_{LSPR}), carrier density (n), carrier effective mass (m^*), and damping (Γ) can be evaluated across the Cd-Sn-O ternary PSNCs.

In metal oxides (MO_x), oxygen vacancies (V_O) and antisite (M'_M) occupation are known to generate carriers and play a critical role in determining the photonic and electronic properties of SCs.[202–204] As a defect that increases electron scattering, the role of V_O and M'_M on carrier self-trapping and the impact on applications utilizing MO_x semiconductors remains a fundamental question. Understanding carrier parentage in MO_x represents one of the leading questions in the field, since the type of defect will impact carrier relaxation dynamics due to introducing unique scattering pathways.[205–207]

Carriers in n-type MO_x are typically associated with V_O that induce carriers in the CB.[208,209] While SCs that are V_O driven dominate the literature, the parentage of the carriers in MO_x can arise from several origins including metal vacancy (V_M), metal interstitial (M_i), and antisite (M'_M). DFT calculations have shown that V_O is generally the lowest energy defect; however, in an inverted spinel, a line phase in the Sn-Cd-O system, theoretical calculations predict that in CTO the M'_M antisite is the dominant carrier contributor.[125] The theoretical predictions suggest vastly different carrier properties exist across the Sn-Cd-O series even though the carriers arise from the introduction of the same Sn(IV) dopant. As such, MO_x PSNCs in the Sn-Cd-O series offer an opportunity to unravel the mysteries of carrier parentage by using

a highly tunable and reproducible synthetic route to explore the evolution of the structure-function relationship.

CdO is a small band gap (E_g) semiconductor with reported bandgaps around 2.0 eV. Density of states (DOS) calculations have shown that it is a direct bandgap semiconductor. CdO has a cubic lattice, where both the Cd(II) and O atoms occupy an octahedral site (O_h). On the other side, CTO is a wide bandgap semiconductor with a E_g value of 3.9 eV, and it is a cubic lattice that possess the inverse spinel structure where the Sn (IV) atoms occupy the octahedral site (O_h), Cd(II) occupies the O_h and tetrahedral (T_d) sites, and O occupies the T_d sites. Although these two structures are completely different, they are formed from the same line phase as a function of Sn concentration. The site occupation is anticipated to impact the *k*-space band projections, valence and conduction band widths and parabolicities, and the presence and energies of donor-acceptor levels.

An advantage of the Sn-Cd-O series is the ability to utilize advanced spectroscopic techniques such as multinuclear SSNMR (^{113}Cd, ^{119}Sn, ^{17}O), Electron Paramagnetic Resonance EPR (V_O vs Sn_{Cd} EPR responsive), and MCD,[172,210,211] to evaluate structure-function correlation in CTO. Insight into carrier relaxation can be probed in CTO through NMR (T_1, T_2) measurements based upon Knight-Korringa correlations, as shown in ITO,[89] MZO,[45] and CuSe.[90] Transient absorption (TA) spectroscopy allows the investigation of carrier relaxation dynamics following LSPR excitation, as we have demonstrated in WO_{3-x} and Cu_xFeS_4.[212,213] While there have been preliminary studies on CdO, Sn:CdO, and CTO nanocrystals, there has not been a thorough investigation to correlate *n*, m^*, and Γ across the Cd-Sn-O ternary family.

The effective mass (m^*) of CdO has been reported in literature in the range of $0.2 – 0.3m_e$ through theoretical calculations and conductivity measurements,[35,214] and the effective mass of CTO has been reported in thin films to be 0.33,[215] while a recent study in CTO PSNC reported through MCD measurements an effective mass of ($0.022\ m_e$). The low m^* value, in conjunction with a large Knight shift, is attributed to the presence of antisite defects, rather than the presence of V_O. The carrier property evolution for the Sn-Cd-O series from Sn:CdO to inverse spinel $CdSn_2O_4$ (CTO) PSNCs is interrogated to understand the competition between V_O and Sn_{Cd} that produce an observable plasmon between 1000 to 3300 nm. It is expected that for the Cd-Sn-O ternary semiconductor series, Sn(IV) aliovalent doping will produce oxygen vacancies (V_O) in Sn:CdO and antisites (Sn_{Cd}) in $CdSn_2O_4$. It is reasonable to assume as [Sn(IV)] increases a

competition between antisite and V_O will be observed as the inverse spinel begins to form local inclusions. The hypothesis is based on observations of the impact of aliovalent doping in II-VI semiconductors and M:ZnO (M=Al, Ga, In).[45] Due to the lattice change from rock salt to the inverted spinel, the value of m^* is anticipated to change, since m^* depends on the conduction band parabolicity and bandwidth. To date, there are no systematic studies evaluating the plasmon progression and carrier parameters across the entire Sn-Cd-O series. To date the reported studies on Sn:CdO and CTO PSNCs have shown that the ω_{LSPR}, and by inference n (assuming no change in m^*), shift with increasing Sn (IV) incorporation.[216,217]

3.2 Experimental Methods

3.2.1 Synthesis of Sn doped Cd-Sn-O PSNCs

The Sn:CdO (5, 10, 15%) PSNCs are synthesized following a modified method from the one reported by Murray and co-workers,[216] and the CTO PSNCs synthesis was done according to recent published work,[103] where the original Sn(IV) source is substituted for a Sn(II) acetate precursor. In a 3-neck round bottom flask fitted with a condenser and a thermocouple, cadmium acetylacetonate ($Cd(acac)_2$, 1.5 - x mmol) and tin(IV) fluoride (x = 0.075, 0.15, 0.225 mmol) are combined with OA (7.5 mmol) and ODE (50 mL). The solution is degassed at 120 °C for 1 hour, and then rapidly heated to 319 °C where is kept refluxing for 40 – 120 minutes (Sn content dependent) until the solution turns dark gray/green indicating the nucleation of Sn:CdO PSNCs. The CTO PSNCs are synthesized by employing 0.3 mmol to reach enough Sn content to induce the formation of the CTO phase. The PSNCs are isolated by addition of IPA, followed by selective precipitation of the smaller Sn:CdO PSNCs in toluene from bigger metallic Cd particles that form as a byproduct. The CTO PSNCs are synthesized in a similar manner as described in recent published synthesis in section 2.2.1 where the original Sn(IV) source is substituted for a Sn(II) acetate precursor. The isolated CdO PSNCs are then passed through a toluene gel permeation chromatography (GPC) column to remove excess ligand following published procedure.[150] The PSNCs are kept in toluene or TCE for storage.

3.2.2 General Characterization

Powder X-ray Diffraction (pXRD) patterns were collected with a Rigaku MiniFlex powder X-ray diffractometer using a Cu Kα source, using a zero-background micro-powder plate. Scans were collected from 15 to 70° at a rate of 7°/min and a 0.05 step size.

Size, size dispersity, morphology, and lattice fringe analysis were obtained by transmission electron microscopy (TEM). TEM images were collected of a Tecnai Osiris TEM/scanning TEM operating at 200 kV. Samples were sonicated for 5 minutes and drop-casted onto lacey carbon-coated copper TEM grids (Ted Pella 01896).

The ^{113}Cd SSNMR experiments were performed using a Bruker NEO console with an Oxford 18.8 T ($\nu_0(^1H)$ = 800 MHz) magnet operating at $\nu_0(^{113}Cd)$ = 177.545 MHz. A home-built 3.2 mm HXY MAS probe was used for all NMR experiments performed at 18.8 T. Pulse width calibrations and chemical shift reference frequencies were calculated using the respective solid-state standards. ^{113}Cd chemical shifts are reported with respect to $Cd(ClO_4)_2$ and (δ_{iso} = 0 ppm) using $Cd(NO_3)_2{\cdot}4H_2O$ (δ_{iso} = −102 ppm) as secondary references.

EPR measurements at X-Band ~9.8 GHz performed on a Bruker ELEXSYS E500 spectrometer fitted with an ER4102ST resonator at room temperature using a 4 mm quartz sample holder.

3.2.3 Optical Characterization

The UV−Vis−NIR Spectroscopy was obtained by taking purified PSNCs (CTO, Sn:CdO) dissolved in TCE. The optical data were collected in a PerkinElmer Lambda 950 spectrometer. A 1 mm path length NIR quartz cuvette was used for all absorbance measurements. Spectra were corrected using TCE.

The Transient Absorption (TA) of CTO PSNCs were prepared the same as previously discussed for extinction spectroscopy. Femtosecond (fs) TA measurements were performed at Florida State University (FSU) using a commercial HELIOS Fire system with a 1024-pixel CMOS sensor for UV-vis measurements and an expected probe pulse width of ~200 fs using a CaF_2 crystal as a blue probe source. Each spectra collected was averaged for 0.5 s and obtained in triplicate in addition to background subtraction and probe chirp correction methods. Pump energy was kept constant at 1600 nm for all samples while ensuring LSPR excitation occurred

for all Cd-Sn-O samples. All measurements were performed at room temperature and under ambient conditions.

3.3 Results and Discussion

3.3.1 Origins of Charge Carriers in Cd-Sn-O Series

In Figure 30, Sn (IV) doped CdO is comprised mainly of V_Os with additional carrier contributions from each Sn(IV) dopant. Each oxygen vacancy donates 2 e^- towards the overall charge carrier concentration. Carriers originating from oxygen vacancies are more polaronic in nature because e^- the gets "trapped" in this type of defect. This trapping of the charge carrier leads to an increase of m^* and a subsequent decrease in conductivity. The presence of V_Os and carrier trapping on these defects has been studied in conductive oxides,[218–220] where it was reported that the presence and concentration of V_Os heavily impact the charge transport properties of these materials. Due to the coupling of the carriers to V_Os, i.e., polaron formation, are associated with rapid hot carrier recombination, which is expected as the *e*-phonon coupling is higher than other defect types. The reported values of m^* for common TCOs such as ZnO, ITO, and CdO depend on synthetic conditions, but are reported to be approximately 0.23,[172] 0.35,[172] and 0.21[214] respectively, which all can be associated to carriers that experience a degree of trapping due to the presence of V_Os.

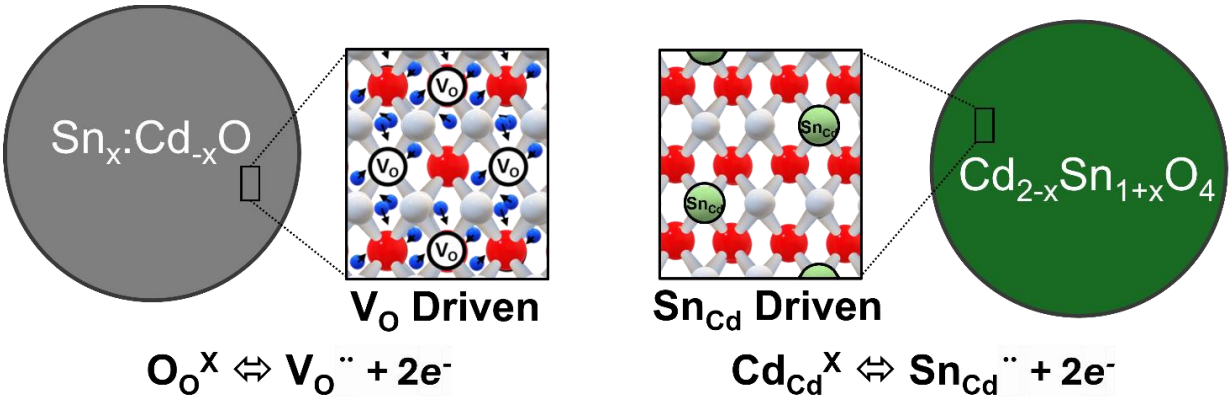

Figure 30. Figure showing the difference between Sn:CdO (V_O major contributor to carrier density) and Cd_2SnO_4 (antisite major contributor to carrier).

On the other hand, CTO (Figure 30) is driven by antisite defects, where "driven" means that the defect type in question is the major contributor to carrier density, as originally predicted by theoretical methods,[125] and later experimentally proposed by Strouse and coworkers.[221] Each Sn_{Cd} antisite creates 2 e^- similar to a V_O, yet these carriers are not associated with a trap center and act as if truly free. This is reflected in the high conductivity values that were observed in CTO thin films which garnered great interest in the development of these films. CTO has been previously thought to be V_O driven, and have conflicting m^* values ranging from 0.35,[215] which is closer to similar oxides, to 0.04[132] The recent work by the Strouse group has reported a value of m^* of 0.022 in well-faceted NCs consistent with the previously values observed by Nozik and the notion that the carriers in these materials are antisite, rather than V_O driven.

In Figure 31, the crystal structures of Sn-doped CdO and CTO are compared. When CdO is doped with 5, 10, and 15% Sn(IV), it retains its rock salt structure. In this structure, Sn(IV) acts as an aliovalent dopant, substituting for Cd(II) atoms at O_h sites and donating two electrons to the crystal lattice. Sn(IV) can be incorporated into the CdO structure up to levels just below 20% without altering the rock salt configuration. However, when the Sn content reaches 20% or higher, the material transitions to the CTO inverse spinel phase to accommodate the excess Sn. In this CTO structure, Sn(IV) atoms occupy octahedral O_h sites, while Cd(II) atoms are found in both O_h and T_d sites.

The transformation from Sn-doped CdO to CTO can be explained by considering the ionic radii of the involved species: 0.95 Å for O_h Cd(II) and 0.75 Å for O_h Sn(IV). Despite the size difference, the O_h sites in CdO can accommodate Sn(IV). As Sn is introduced into the CdO lattice, the carrier concentration (n) increases as expected for an aliovalent dopant. To incorporate more Sn into the CdO lattice, a structural reconfiguration occurs. Half of the O_h Cd(II) atoms are displaced into empty T_d sites within the CdO lattice, becoming T_d Cd(II) atoms in the CTO structure. This displacement leaves the newly introduced Sn(IV) and the remaining Cd(II) atoms in the O_h positions. The resulting CTO structure exhibits distinct electronic, crystallographic, and carrier properties compared to the original Sn-doped CdO.

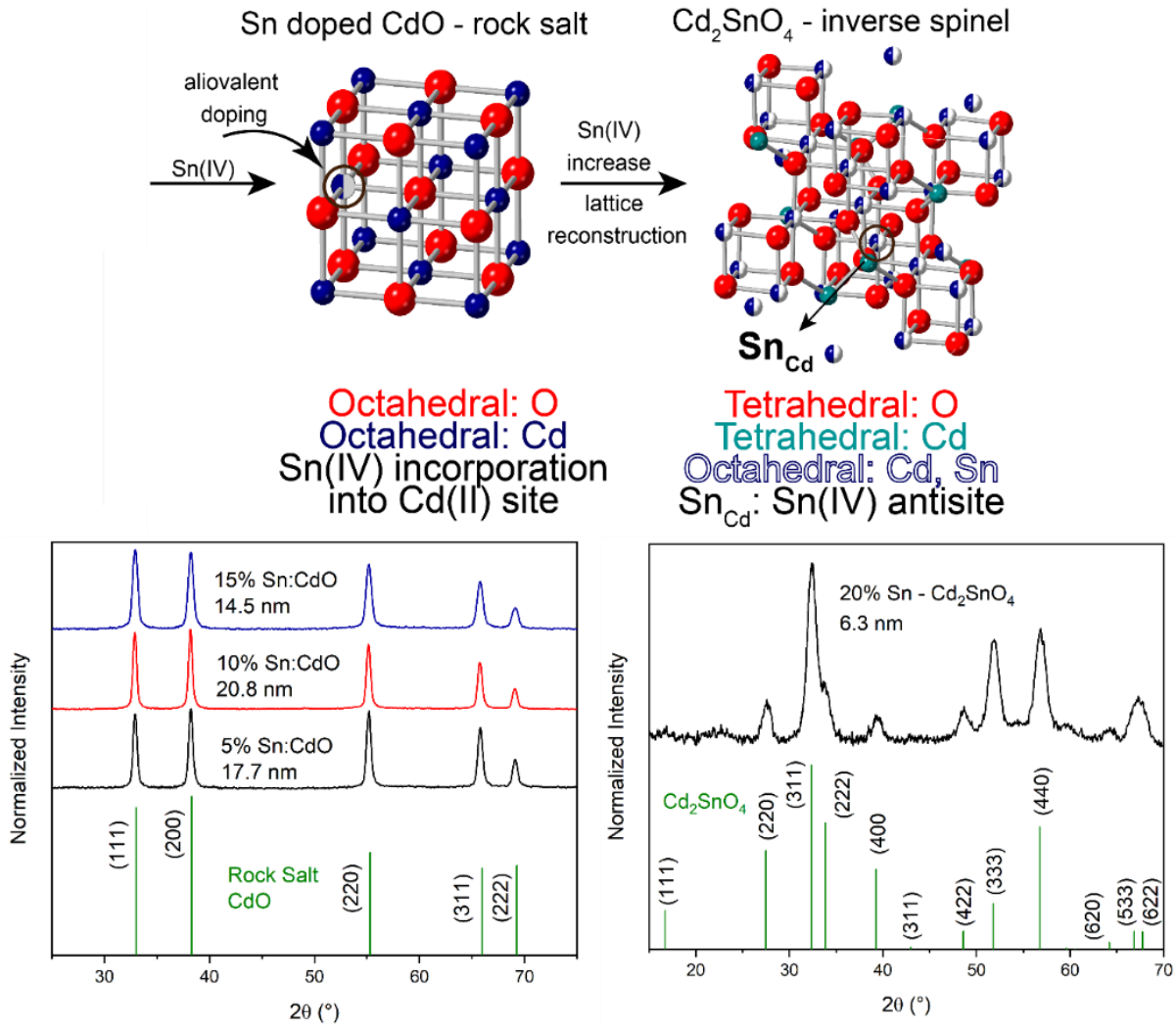

Figure 31. Evolution of the crystal structure, pXRD, and sizes of rock salt Sn (IV) doped CdO and inverse spinel Cd_2SnO_4.

To further elucidate structural information of the Sn:CdO PSNCs, the ^{113}Cd SSNMR spectrum is provided in Figure 32. The comparison of the ^{113}Cd WURST-CPMG NMR spectra of stationary samples of the 10% Sn:CdO PSNCs exhibits a distinct breadth of 400 kHz (2300 ppm) with a very intense gaussian-like feature at around 1400 PPM, which suggest that the origin of this shift is from a very uniform site. Although currently the origin of this feature is assigned to a large Knight-shift, it is very possible that it arises from chemical shift. The main takeaway from this spectra is to denote that both the reported ^{113}Cd WURST-CPMG NMR for CTO (Figure 25) and Sn:CdO (Figure 32) demonstrate very different chemical and electronic environments. Without further experiments such as CP-MAS or removal of the free carriers to

eliminate sight from KS, it is hard to make assignments of core vs. surface. Current efforts are underway to understand the KS and CS of the Sn:CdO NMR spectra

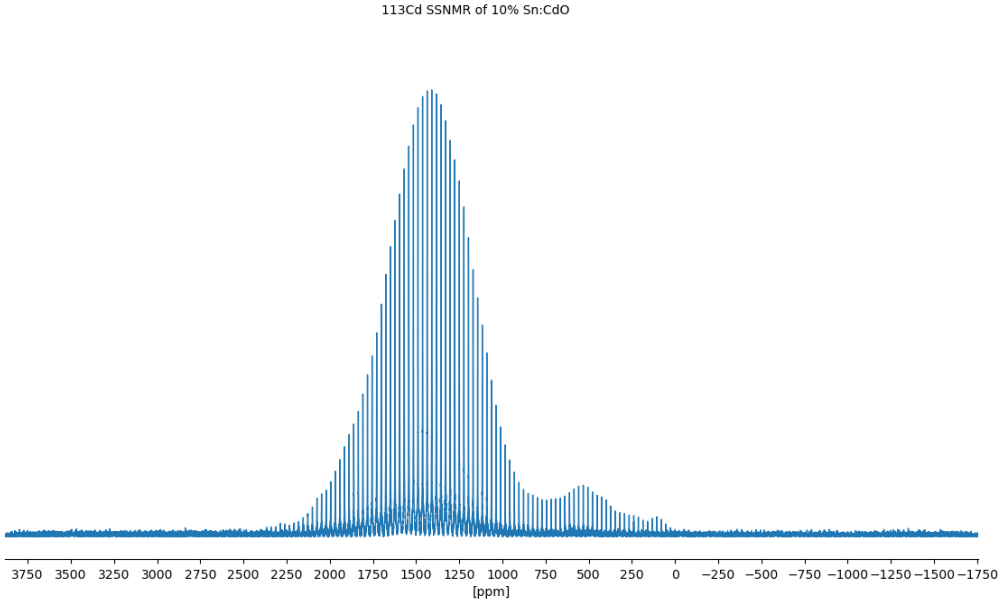

Figure 32. ^{113}Cd of 10% Sn:CdO PSNCs collected using a WURST-CPMG pulse sequence.

In Figure 32 the TEM images collected from the 15% Sn:CdO reveals that the NCs have an octahedral morphology as reported by Murray and coworkers.[216] In addition, high-resolution TEM allows for measurement of the lattice fringes to obtain a *d*-spacing value of 0.28 Å, which corresponds to the (111) lattice plane of cubic rock salt CdO. The slight decrease in *d*-spacing for the (111) can be understood as the substitution of a smaller atom, Sn(IV), for Cd(II) in CdO lattice.

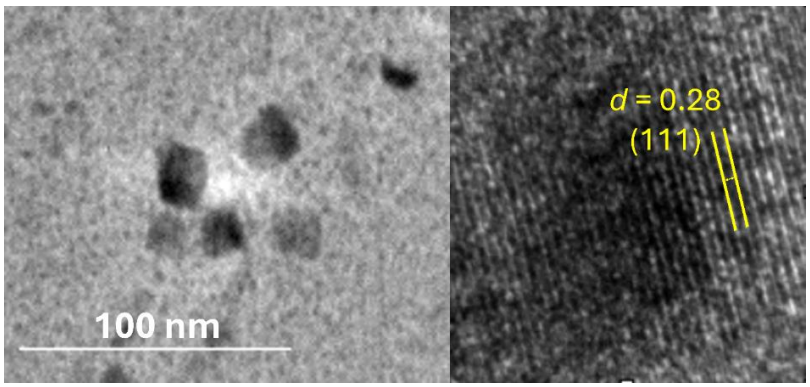

Figure 33. Low resolution TEM image (left) showing the octahedral morphology for the 15% Sn:CdO. High-resolution TEM on a NP shows a d-spacing of 0.28 that is assigned to the (111) facet of the cubic rock-salt CdO lattice.

3.3.2 Optical Measurements of Cd-Sn-O Series

The extinction and Tauc plot spectra of 5, 10, and 15% Sn:CdO are shown in figure 34. The observed absorption edge in the optical spectra at > 3.0 eV (333 nm) is assigned to the onset of E_g, while the features at 0.68 eV (1823 nm), 0.72 eV (1722 nm), and 0.74 eV(1675 nm) are assigned to the LSPR of the 5, 10, and 15% Sn:CdO respectively. In Figure 34, a Tauc plot is plotted to analyze the optical bandgap ($E_{g,opt}$), yielding values of 3.22 eV (385 nm), 3.36 eV (369 nm), 3.54 eV (350 nm) for 5, 10, and 15% SnCdO respectively. The hypsochromic shift of the $E_{g,opt}$ and LSPR frequency with Sn content follow both the Burstein-Moss and Drude behavior, where the increase in energy for each feature is dependent on $n^{2/3}$ and $n^{1/3}$ accordingly.

The LSPR exhibits three modes, with peaks at 0.75 eV (6053.2 cm^{-1}), 0.68 eV (5530.9 cm^{-1}), and 0.65 eV (5263.1 cm^{-1}) for 5% Sn, 0.79 eV (6410.0 cm^{-1}), 0.74 eV (5938.0 cm^{-1}), and 0.70 eV (5617.0 cm^{-1}) for 10% Sn, and 0.83 eV (6702.0 cm^{-1}), 0.77 eV (6218.0 cm^{-1}), and 0.73 eV (5910.0 cm^{-1}) for 15% Sn, that are attributed to face, edge, and corner contributions to the LSPR, respectively, as seen in Figure 34. The three-mode SDA model provides an average n of 7.30×10^{19} carriers cm^{-3} The distinct modes are expected based on the octahedral shape observed by TEM and reported by Murray and coworkers,[216] leading to the separation of the LSPR into three different modes corresponding to the face, edge, and corner contributions.[76,115,167,222] It is important to note that it seems that the corner contributions increase as a function of [Sn] relative to the edge and face contributions. This might be an indication that the inclusion of Sn is responsible for the elongation of these PSNCs, as observed in the CTO samples where a high aspect ratio of 1.30 was measured leading to highly faceted PSNCs. This observation was also indirectly reported by Murray and coworkers where they noted that the Sn(IV) doped CdO PSNCs possessed octahedral morphology, where the In(III) doped CdO NCs yielded spherical morphology.[216]

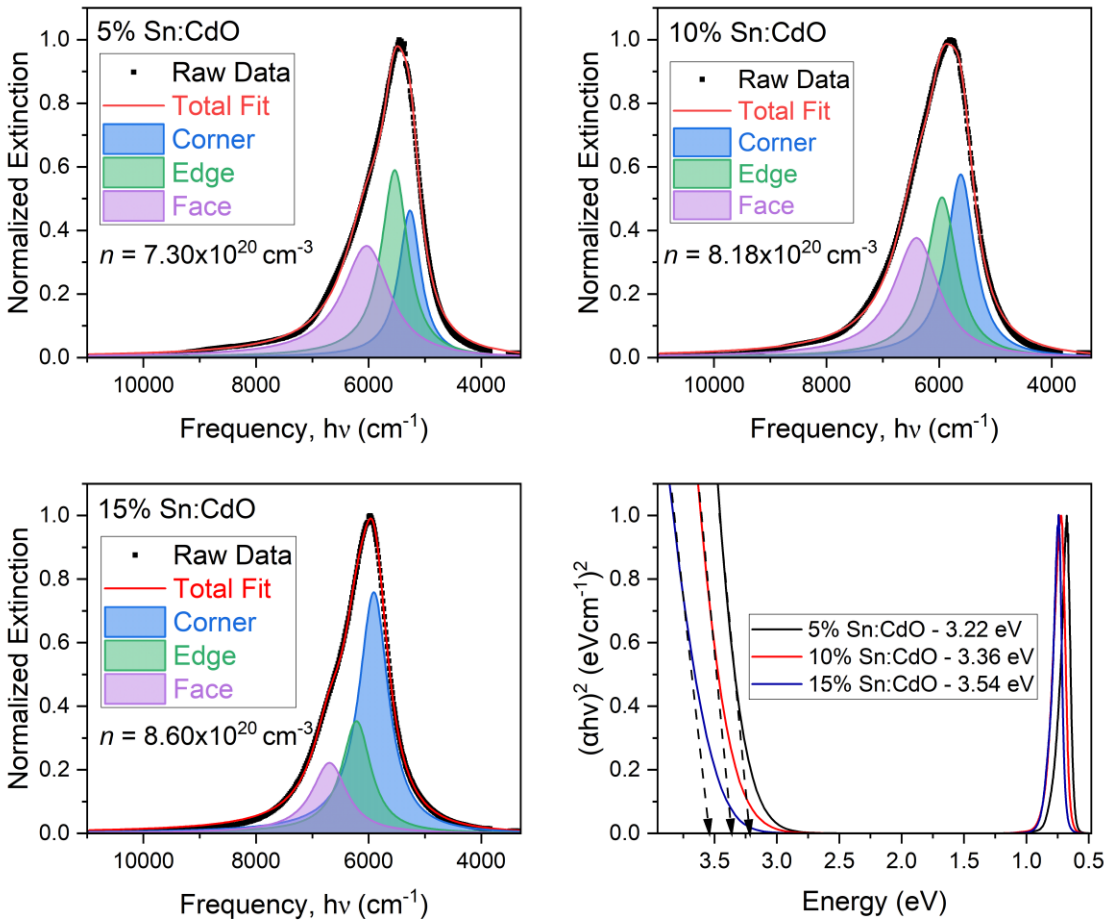

Figure 34. Tauc Plot and extinction spectra of 5, 10, and 15% Sn:CdO with each corresponding LSPR fitted to a 3-mode simplified Drude approximation illustrating the corner, edge, and face contributions with corresponding calculated carrier densities.

3.3.3 EPR Measurements of Cd-Sn-O Series

EPR and photoinduced EPR were used to show the distinction between pinned and free carriers in Al_2O_3@Al and have correlated SSNMR Al chemical shifts to provide insight into catalytic activity vs. defect type.[223] Here EPR is employed to study the g-value shifts of carriers originating in the Sn:CdO and CTO series. Surprisingly in PSNCs, the EPR behavior has not been explored; although g-value shifts with increasing n in Nb:TiO_2 was observed but not discussed.[72] In the CTO PSNC as a function of increasing antisite occupation, we expect the EPR g-value for $V_O^{\cdot}$ and $V_{Cd}^{\cdot}$ to be invariant with n, while the free carrier concentration follows a $n^{1/3}$ dependence. With increasing Sn_{Cd} occupation, the temperature dependent EPR line width for the

free carrier is linearly dependent on temperature, decreasing with decreasing temperature, as predicted by Knight-Korringa behavior. In EPR, KS in PSNCs has not been investigated, although EPR shifts proportional to PSNC size was reported.[224,225] In Figure 35 EPR data shows a high sensitivity to defect type,[223,226,227] strongly supporting the hypothesis that EPR resonance and KS should be responsive to changes in Sn_{Cd} occupation for CTO.

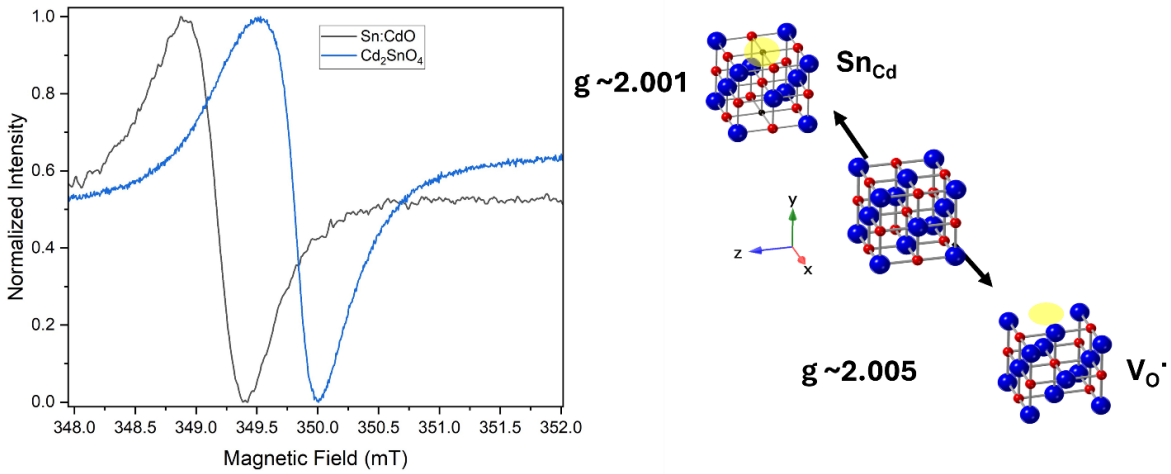

Figure 35. EPR spectra of 5% Sn:CdO and CTO demonstrate the large EPR shift due to drastically different carrier origin.

In Figure 35, the EPR spectrum of 5% Sn:CdO and CTO are plotted as a function of magnetic field. The magnetic field can be converted to g-value (analogous to ppm in NMR) to compare the two samples. The 5% Sn:CdO feature is at around 349.25 mT (2.001 g) which is mainly attributed to contributions from V_Os where there's an equilibrium between the double ionized $V_{Ox}^{\cdot\cdot}$ and the singly ionized $V_{Ox}^{\cdot}$, which is EPR active. Although both single- and doubly- ionized V_O defects affect conductivity, only the singly ionized feature is EPR active, which allows direct observation of the signal arising from V_O. The CTO has an EPR response of about 349.85 mT (2.005 g) coming from the free carriers introduced by the Sn_{Cd} defect in CTO.

From the EPR measurement it is clear that the differences in g-value between the two distinct samples are due to the populations of both V_O and Sn_{Cd} having drastically different responses. The Sn_{Cd} exhibits a g-value shift similar to that reported for other free carriers,

indicating that these carriers are truly delocalized in CTO compared to the carriers originating from V_O in Sn:CdO.

3.3.4 Femtosecond Transient Absorption Measurements

Transient absorption at the femtosecond to nanosecond timescale is used to evaluate the impact on relaxation pathways as an indirect measure of carrier mobility in the Cd-Sn-O PSNC series. It is hypothesized with increasing [Sn] in CdO, the increasing impurity centers will shorten the carrier relaxation, while at the CTO phase transition it is anticipated the carrier mobility will be increased due to a loss of impurity scattering due to the decrease of V_O, and the electron–phonon (*el-ph*) relaxation will increase.

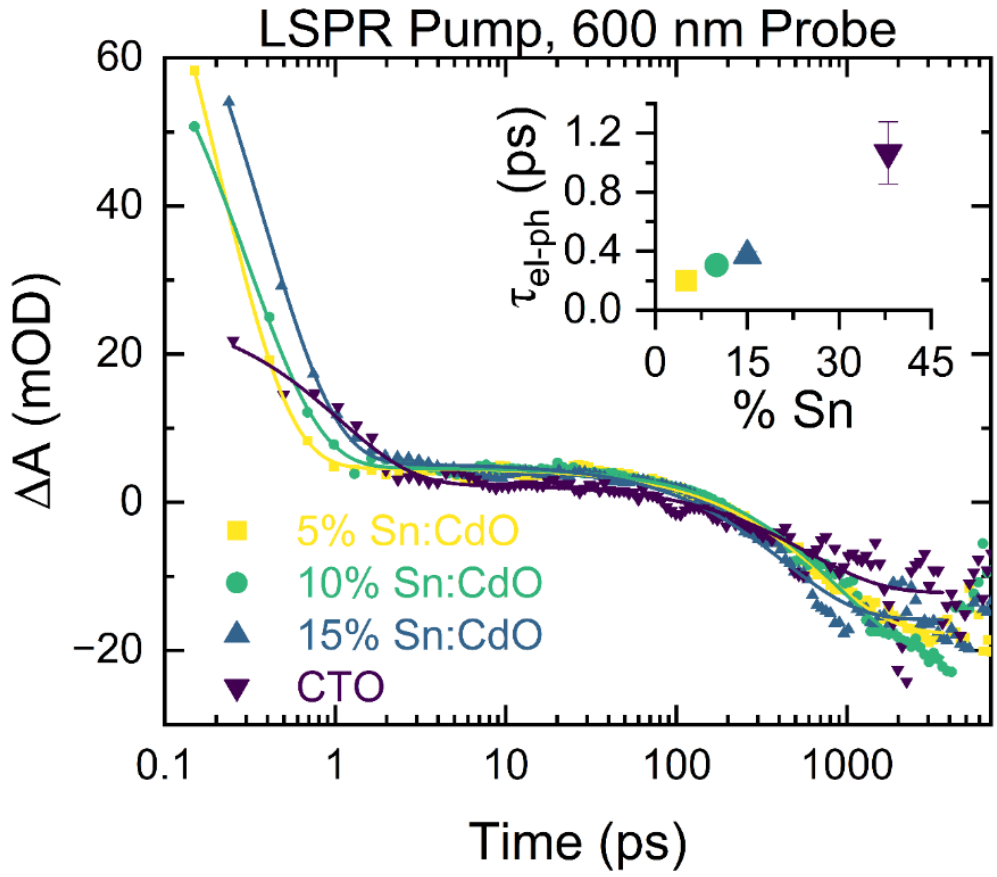

Figure 36. Hot electron interband relaxation kinetics for various nominally doped Sn:CdO PSNCs compared with CTO PSNCs. When fit to a bi-exponential equation, CTO PSNCs display the longest lifetimes for both *el-ph* relaxation as expected due to a maximization of Sn_{Cd} vs. V_O.

Upon LSPR excitation, all spectra feature an expected photoinduced absorption (PIA) tail feature at < 550 nm lasting less than 10 ps, which slowly shifts into a bleach beyond 50 ps. All materials are fit to bi-exponential lifetimes attributed to (*el-ph*) relaxation and thermalization due to phonon-phonon (*ph-ph*) relaxation for fast and slow components respectively. The fast PIA component is attributed to hot electron interband relaxation, as the timescale of the phenomenon matches the expected time of electronic relaxation and is in the energy regime of the band gap for these materials. The bleach component is attributed to band gap reorganization due to plasmon thermalization, resulting in the appearance of a depleted ground state at longer time scales.

As [Sn(IV)] increases, changes in the band diagram and V_O density lead to changes in m^* and n. It is anticipated that V_O trap sites should lead to rapid relaxation via an electron trapping mechanism, while Sn_{Cd} should only contribute free electrons with minimal negative impact on relaxation kinetics. As shown in Figure 36, hot electron interband relaxation after LSPR pumping (1600 nm) is observed for the Cd-Sn-O series, where the *el-ph* lifetimes are found to be 199.7 ± 6.3 fs, 305.8 ± 11.4 fs, 372.3 ± 22.3 fs, and 1.06 ± 0.02 ps in order of increasing [Sn] dopant. The results support the hypothesis that increased Sn_{Cd} contributions minimize trapping probability from deleterious defects like V_O, and is similar to a report observing *el-ph* changes in In:CdO.[228]

3.4 Conclusions

In MO_x semiconductors, V_O and antisite defects generate carriers and significantly impact the photonic and electronic properties. Investigating how these defects affect carrier self-trapping in PSNCs is crucial for applications involving MO_x semiconductors. Notably, in the Sn-Cd-O system, the Sn_{Cd} antisite defect is the primary carrier contributor in CTO, resulting in varied carrier properties across the series, despite all additional carrier density originating from the same Sn(IV) dopant.

The Sn(IV) doping in CdO PSNCs retains its rock salt structure up to 20% Sn concentration, beyond which it transitions to the CTO inverse spinel phase in the nanoscale. This structural transition affects the electronic, crystallographic, and carrier properties. Optical

measurements reveal hypsochromic shifts in the energy gap and LSPR frequencies with increasing Sn content, following Burstein-Moss and Drude behaviors.

The m^* of carriers in Sn-doped CdO PSNCs are influenced by the presence of V_Os, which increase electron scattering and decreases conductivity due to carrier trapping. In contrast, CTO, driven by antisite defects, shows lower effective mass and higher conductivity, indicating free carriers not associated with trap centers. The EPR measurement demonstrates this behavior by the drastic shift in EPR signal between the Sn:CdO and CTO PSNCs.

Femtosecond transient absorption measurements demonstrate that the electronic relaxation and thermalization processes vary with Sn doping levels. Higher Sn concentrations reduce the probability of electron trapping by V_O, leading to longer electronic relaxation lifetimes, which is consistent with the hypothesis that antisite defects contribute free electrons with minimal trapping.

In conclusion, structural and optical characterization provides a comprehensive understanding of how carrier parentage and dopant site occupation influence the evolution of metallic character in Sn-Cd-O PSNCs. The SSNMR and EPR allow to study novel PSNCs through methods that are not usually employed. The results in this work lay the foundation to utilize and understand carrier evolution in different PSNCs, which can help in optimizing the design and performance of PSNCs for various applications, particularly in enhancing conductivity and minimizing electron trapping by carefully controlling defect types and dopant concentrations.

CHAPTER 4

ANNEALING EFFECTS IN CADMIUM STANNATE PLASMONIC SEMICONDUCTOR NANOCRYSTALS

4.1 Introduction

TCOs are materials that exhibit both optical transparency and electrical conductivity, making them important materials in displays,[229] solar cells,[34] and electrochromic windows (smart windows).[8] However, the performance on TCOs is significantly influenced by various crystallographic defects, including V_Os, M_is, V_Ms, and even M'_M.V_Os occur when oxygen atoms are missing from the crystal lattice, interstitial metals are formed when a metal is small enough where it can occupy interstitial sites, metal vacancies are formed when metal atoms are missing during the crystal growth process, and M'_M sites are created when two atoms are capable of occupying the same lattice site without causing major lattice distortion. All these crystallographic defects can alter the electronic properties of the material, therefore there are considerable efforts to remove or "anneal" these crystal imperfections. Annealing can reduce or minimize these defects by providing enough energy to move and fill vacancies, improving the crystallinity and overall material performance. The annealing protocol differs from material to material, since it is very dependent on the energies of the defects that need to be annealed. Developing an annealing protocol involves a lot of trial and error through different annealing conditions. The annealing process involves slow heating up the material at a specific temperature for a fixed amount of time, which allows the crystal to reconfigure into a more energetically favorable structure, thus reducing the number of defects. For example, ITO is routinely annealed[230] to promote diffusion of Sn atoms and fill metal vacancies, enhancing its electrical conductivity.

The annealing effects of CTO has been studied in thin films due to their high transparency in the visible spectral region, high carrier mobility, and low surface roughness, which has led them to be employed in CdTe films and perovskite based solar cells[231] making them attractive toward optoelectronic devices. Although there is interest in this topic in the thin CTO thin films, the annealing effects on the structure, and plasmonic properties in CTO PSNCs have not been explored.

In MO_x bulk and thin film samples is common to anneal samples under low O conditions to induce V_Os and increase *n*. The same can be done in O-rich conditions to ensure that the materials have low V_O concentrations. Originally it was understood that V_Os were the main source of carrier generation in CTO, but it has been reported that Sn_{Cd} antisites are the major contributors to carrier density. It has been suggested theoretically[125] and experimentally[232,233] that annealing CTO samples under Cd-rich conditions will lead to higher Sn_{Cd} formation, and thus, higher carrier concentrations, while diminishing the hypothesis that Cd_i and V_O are major contributors to carrier generation.

In this work, the structural and optical properties of CTO are investigated before, during, and after the annealing process. The changes in structure and optical response due to defect migration are monitored through the plasmon frequency (UV-Vis-IR spectroscopy), structural changes (pXRD), size/faceting changes (TEM), changes in metal-oxygen bond frequency and ligand packing (FTIR), and Cd:Sn content (XRF).

4.2 Experimental Methods

4.2.1 Synthesis of CTO Inverse Spinel PSNCs

The CTO PSNCs are synthesized following a modified method based on the one reported by Ye and co-workers,[103] where the original Sn(IV) source is substituted for a Sn(II) acetate precursor. In a 3-neck round bottom flask fitted with a condenser and a thermocouple, cadmium acetylacetonate ($Cd(acac)_2$, 1.2 mmol) and tin(II) acetate ($Sn(OAc)_2$, 0.3 mmol) are combined with OA (7.5 mmol) and ODE (25 mL). The solution is degassed at 120 °C for 1 hour, and then rapidly heated to 319 °C where is kept refluxing for 100 minutes until the solution turns dark black/grey indicating the nucleation of CTO PSNCs. The PSNCs are isolated by addition of IPA, followed by selective precipitation of the smaller CTO in toluene from bigger metallic Cd particles that form as a byproduct. The isolated CTO NCs are then passed through a toluene gel permeation chromatography (GPC) column to remove excess ligand following published procedure.[150] The NCs are kept in toluene or TCE for storage.

4.2.2 General Characterization

Powder X-ray Diffraction (pXRD) patterns were collected with a Rigaku MiniFlex powder X-ray diffractometer using a Cu Kα source. The pXRD patterns were collected using a zero-background micro-powder plate. Scans were collected from 15 to 70° at a rate of 7°/min and a 0.05 step size.

Fourier transform infrared (FTIR) spectroscopy of the annealed CTO samples was performed with a JASCO-6800 FT-IR spectrometer.

UV−Vis−NIR absorbance of purified CTO are dissolved in TCE for all optical measurements. The optical data were collected in a PerkinElmer Lambda 950 spectrometer. A 1 mm path length NIR quartz cuvette was used for all absorbance measurements. Spectra were corrected using TCE.

Size, size dispersity, morphology, and lattice fringe analysis were obtained by transmission electron microscopy (TEM). TEM images were collected of a Tecnai Osiris TEM/scanning TEM operating at 200 kV. Samples were sonicated for 5 minutes and drop-casted onto lacey carbon-coated copper TEM grids (Ted Pella 01896).

Elemental composition for all samples was confirmed using X-ray Fluorescence (XRF) on a Panalytical Epsilon X-ray fluorescence analyzer (Malvern, UK; Cu Kα source).

4.3 Results and Discussion

4.3.1 Annealing of CTO PSNCs

To analyze defect behavior during the annealing process, a scaled-up batch of CTO PSNCs was synthesized and purified as described in section 4.2.1, but using five times the amount of reagents, and following the already published methodology. The scale-up did not affect the the material properties, as described in previous work. The resulting CTO PSNCs from the scaled-up batch were dissolved in 24 mL of ODE (non-coordinationg solvent) to ensure that the particles remained dispersed in solution. The CTO solution was quickly degassed at 120 °C for 20 minutes in a 50 mL round bottom flask, then quickly heated to 290 °C and it remained at this temperature during the reminder of the annealing period. Aliquots were taken at 0 (before anneal), 1, 2, 4, 6, 8, 12, and 24 hours.To ensure that enough annealed CTO PSNCs were extracted to track the evolution of the PSNCs, 8 mL aliquots were taken at 0, 6, and 24 hours,

and only 1 mL was taken 1, 2, 4, 8, and 12 hours to track LSPR changes. The aliquots were cleaned with toluene and IPA, then redissolved in TCE for further characterization. Throughtout the manuscript, there are 8 total aliquots and they are referered to as P#1, P#2, P#3, P#4, , P#5, P#6, ,P#7, P#8 for the sample measurements taken at 0, 1, 2, 4, 6, 8, 12, 24 hours, respectively. It is worth noting that at every point that an aliquot was taken, a small amount of Cd metal was also collected with each draw. These observations suggest that CTO PSNCs expell Cd during the annealing process as a function of time, or within the first hour as suggested in a further section.

4.3.2 Evolution of CTO LSPR During Annealing

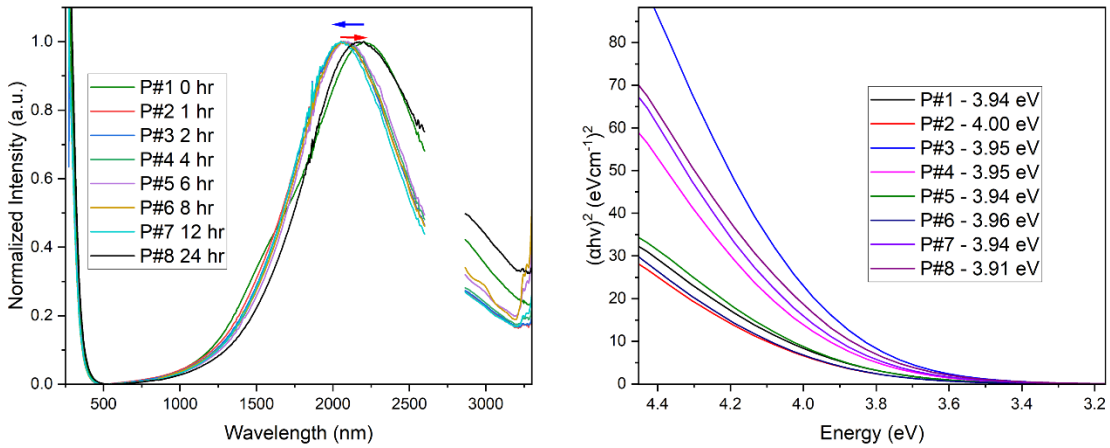

Figure 37. Extinction spectra of the aliquots taken during the annealing period (left). Tauc plot of the aliquots taken during the annealing process (right).

In Figure 37, the normalized LSPR extinction spectra of all the aliquots is shown to track the LSPR frequency chages as a function of the annealing time. In P#1, the LSPR is similar to the already published CTO LSPR, with the main feature at 2208 nm (0.56 eV) and a prominent shoulder feature at around 1500 nm (0.83 eV), which was accredited to the well-faceted morphology of the CTO samples by employing a Sn(II) source as discussed above. After 1 hour,the peak in the spectrum of P#2 blue-shifts to 2068 nm (0.60 eV) for a $\Delta\lambda$ of 140 nm (0.04 eV). This shift to higher energy can be explained by two possible phenomena: i) remaining unactivated Sn(IV) atoms in interstitials, or at the surface, migrate into the O_h Cd(II) sites, creating Sn_{Cd} in the process, thereby increasing n in the process; or (ii) any leftovover defect such as V_Os or M_is that might have been left over from the pristine synthesis gets annealed, thereby decreasing scattering centers and decreasing m^*, which shows as a shift of the LSPR to

higher energy. In additon, the shoulder feature is greatly reduced in intensity, suggesting changes in the facetting of the CTO PSNC, or annealing of a particular defect that is responsible for that feature. It is also possible, although speculative at this point, that the feature around 1500 nm is due to V_Os that get rapidly annealed within the first hour. For the next 12 hours (P#2 through P#7) there are negligible or no changes in the LSPR energy and quality factor, indicating that the samples remain stable within this time period, and that the main annealing event, if any, happens within the first hour. After 24 hours, P#8 red-shifts from 2056 (0.60 eV) to 2172 nm (0.57 eV), with an increase in the LSPR FWHM from 882 to 954 nm. There are several potential factors contributing to the LSPR red shift observed at the 24-hour mark. During annealing, the particles may be redissolving into the ODE as it is possible for NCs to be broken down and dissolved. Additionally, the nanoparticles might be unstable due to the ejection of Cd, as evidenced by the observed metallic Cd in the aliquots. Another possibility is the loss of Sn content in the CTO PSNCs, resulting in a reduction of Sn_{Cd} defect density, as antisite defects, like other defects, are prone to annealing. Furthermore, the m^* of the CTO PSNCs could be lower than that of the pristine samples due to the removal of scattering defects, as indicated by the broadening of the LSPR feature, which is known to be a function of the PSNC's m^*.

Analyzing the Burstein-Moss shift through Tauc plot analysis can give further insight into free carrier concentration. The Tauc plot (Figure 37) shows a similar behavior to the LSPR extinction spectra. At P#1, the calculated E_g of 3.94 eV gets blue shifted to 4.0 eV after annealing for 1 hour (P#2). This shift indicates that there's a slight increase in n, which can be attributed to the same reasons for the shift in LSPR noted above. From P#2 to P#7 the E_g remains relatively constant at an average value of 3.96 eV following similar behavior to what is observed in the LSPR analysis. Finally, the E_g red shifts to a value of 3.91 which is a drastic shift in accordance with the observations of the LSPR. These shifts suggest that n is changing as a function of annealing time, through changes in Sn_{Cd}, or m^* is changing, as the Burstein-moss shift is also sensitive to changes in m^*.

4.3.3 Structural Analysis of Annealed CTO

To analyze any changes to the crystal structures of the annealed CTO PSNCs, the pXRD patterns of P#1, P#5, and P#8 (Figure 38) were obtained. All the patterns fit well to the inverse spinel structure (PDF 01-080-1468), and there seems to be no secondary phases such as SnO_2 or

CdO forming during the annealing process. The powder patterns are extremely similar to each other, suggesting that no drastic changes in crystallinity occur as a function of annealing, even when obvious changes in the LSPR are observed. The sizes of the PSNCs obtained through the pXRD are within error of each other, further suggesting that there are no structural changes between the samples. The Halder-Wagner method used to calculate the NC size through pXRD data also reports strain values, which are not always accurate as the true size of the NCs is hard to obtain through pXRD alone. Any changes in size can be interpreted as changes in the strain of the lattice, and vice versa. If the size of the PSNCs is not changing, the change in strain from P#1 to P#5 suggests that the Sn migration argument is the possible mechanism at play by reducing the number of V_M available, lowering strain as explained in section 4.1.

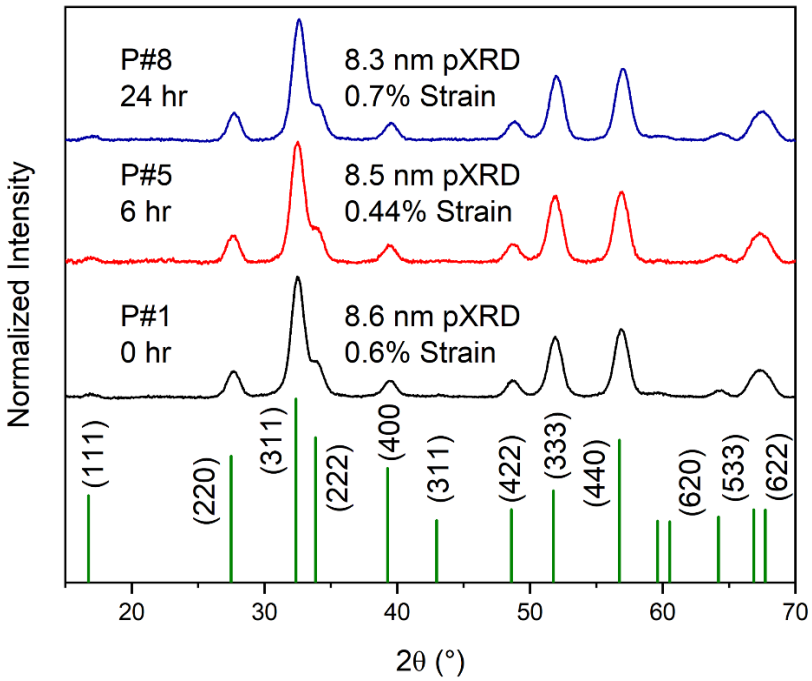

Figure 38. pXRD patterns of annealed CTO PSNCs with corresponding inverse spinel Cd_2SnO_4 reflections, size, and strain % obtained from the Halder-Wagner method.

If there are no evident changes in crystal structure, perhaps there are faceting or drastic size changes between samples. In Figure 39, the TEM and histograms of P#0, P#5, and P#8 are shown. The CTO PSNCs are well formed and seemed to have octahedral morphology, as previously reported in the original CTO work.[221] The P#0 sample has a size of 10.4 ± 1.3 nm with a 12.4% size distribution, following a decrease in size to 9.3 ± 1.4 nm when P#5 is reached.

This slight change in size is consistent with the changes observed in the LSPR, meaning that the reduction in size is correlated to the defect changes associated with the shift in LSPR. At P#8 there seems to be no further changes in size (9.4 ± 1.4 nm, 13% distribution), which does not explain the changes in LSPR; hence, and thus the size changes might not be correlated at all to the changes in LSPR.

The aspect ratio of the CTO octahedral PSNCs can be calculated through TEM by measuring long and short sides of the PSNCs. The aspect ratio of the PSNCs might reflect different growth stages, as the 001 facet of the octahedral PSNCs are high energy facets due to it being the tips of the octahedrons. A change in the aspect ratio would imply that as the sample anneals, the quickest and most notable change would be the 001-facet, and it is expected that the particle will start to become rounded or shrink (lower aspect ratio). As shown in Figure 39, the aspect ratio starts (P#1) at 1.19, then increases to 1.24 (P#5). Although this is the opposite of the expected behavior, it might be explained by the increase in Sn content, which will be explained in the upcoming section. At P#8 the samples revert to an aspect ratio closer to the original, which might be related to the idea that the CTO PSNCs start to break down after 24 hours.

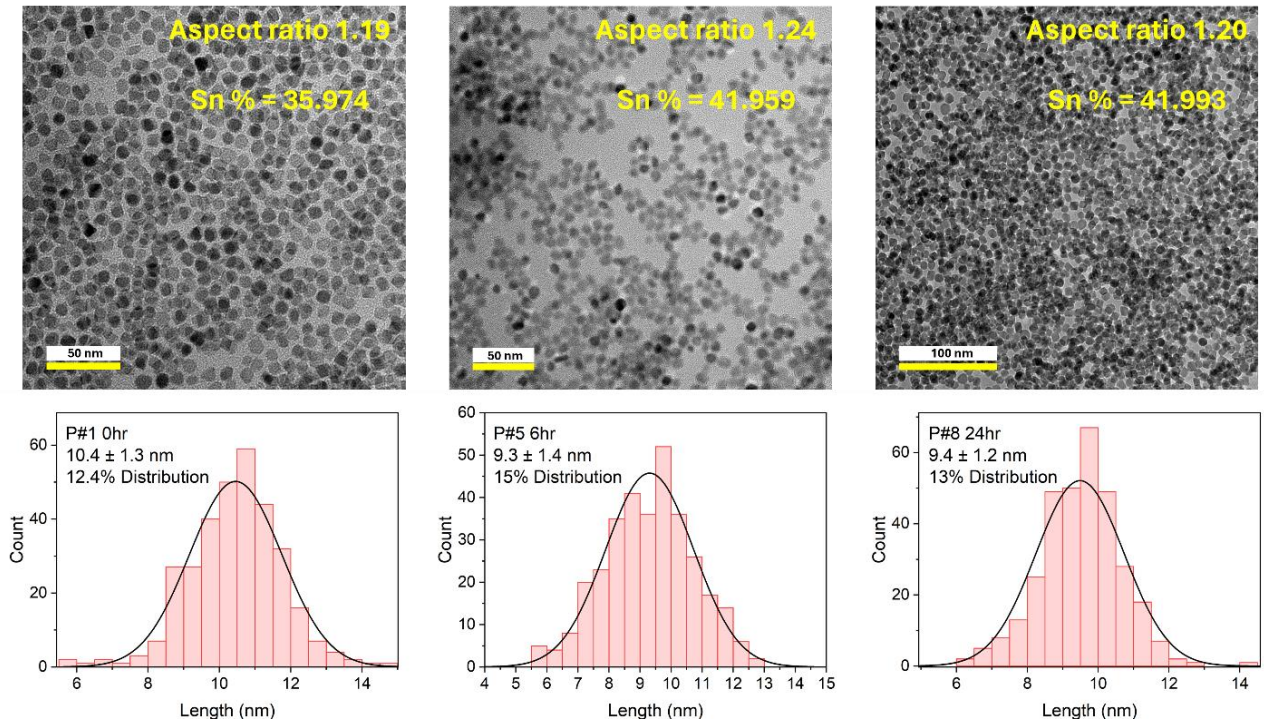

Figure 39. TEM, histograms, aspect ratio, and %Sn content of annealed P#1, P#5, and P#8 CTO PSNCs.

An interesting aspect of the annealing experiments is that the Sn content seems to be changing as a function of the annealing time (Figure 39). At P#1, the Sn content is 35.974% which is congruent with the inverse spinel where Sn atomic % surpasses the 33.33% amount. At the P#5 mark, there is an increase of Sn content to 41.959%, which correlates well with the changes in LSPR from P#1 to P#5 (Figure 37), suggesting that the changes in LSPR are because of the possible formation of extra Sn_{Cd} defects. In P#8, it seems that the Sn content does not change between P#5 and P#8; therefore, there might be another factor playing a role in the LSPR changes in P#8 (Figure 37). As alluded to earlier, it is possible that the Sn content in the CTO PSNCs is related to the aspect ratio of the octahedrons. It was noted by Murray and coworkers[216] that the octahedral morphology is more pronounced in the Sn(IV) doped CdO PSNCs than the In(III) doped samples, suggesting that there may be a morphology-directing component to the incorporation of Sn that elongates the PSNCs. This observation would also suggest why it is possible to grow CTO PSNCs with such defined octahedral morphologies with aspect ratios of up to 1.30, as reported for the CTO PSNCs.[221]

4.3.4 FTIR Investigation of Annealed CTO

To elucidate further information about the local structure and crystallinity and of the annealed CTO PSNCs, the FTIR spectra of P#1, P#5, and P#8 are shown in Figure 40. The first area of interest is the region from 444 cm^{-1} to 886 cm^{-1}, which is commonly assigned in literature to Cd-O stretch vibrations, which are in a similar frequency range to other M-O stretching modes[234–236] Although it is enticing to assign this feature to the Cd-O stretch, typical Cd-O stretches are more commonly observed at lower frequency values (< 450 cm^{-1}); therefore, it is more likely that this feature is the Sn-O stretching vibration, as seen in SnO_2.[237] This Sn-O stretching mode has been more accurately assigned to the A_{2u} (700 cm^{-1}) and E_u (633 cm^{-1}) TO vibrational modes. Upon further inspection of this region, P#1 only has one peak at 624 cm^{-1}, and upon further annealing to P#5 and P#8, it is clear that a new peak grows in intensity at 734 cm^{-1} in conjunction to a small broadening of the 624 cm^{-1} feature. The broadening of the Sn-O stretch at 624 cm^{-1} is minimal and appears to remain constant by the time the P#5 feature is reached. The observed changes in the 734 cm^{-1} peaks indicate a distinct alteration in the crystallinity of the Sn-O bond as a function of annealing, which indicates that the Sn-O crystallinity is drastically changing, as observed in changes of the Sn concentration in the CTO

PSNCs through XPS. This shift in behavior results in the broad Sn-O feature splitting into the two distinct vibrational modes at 624 and 734 cm^{-1}.

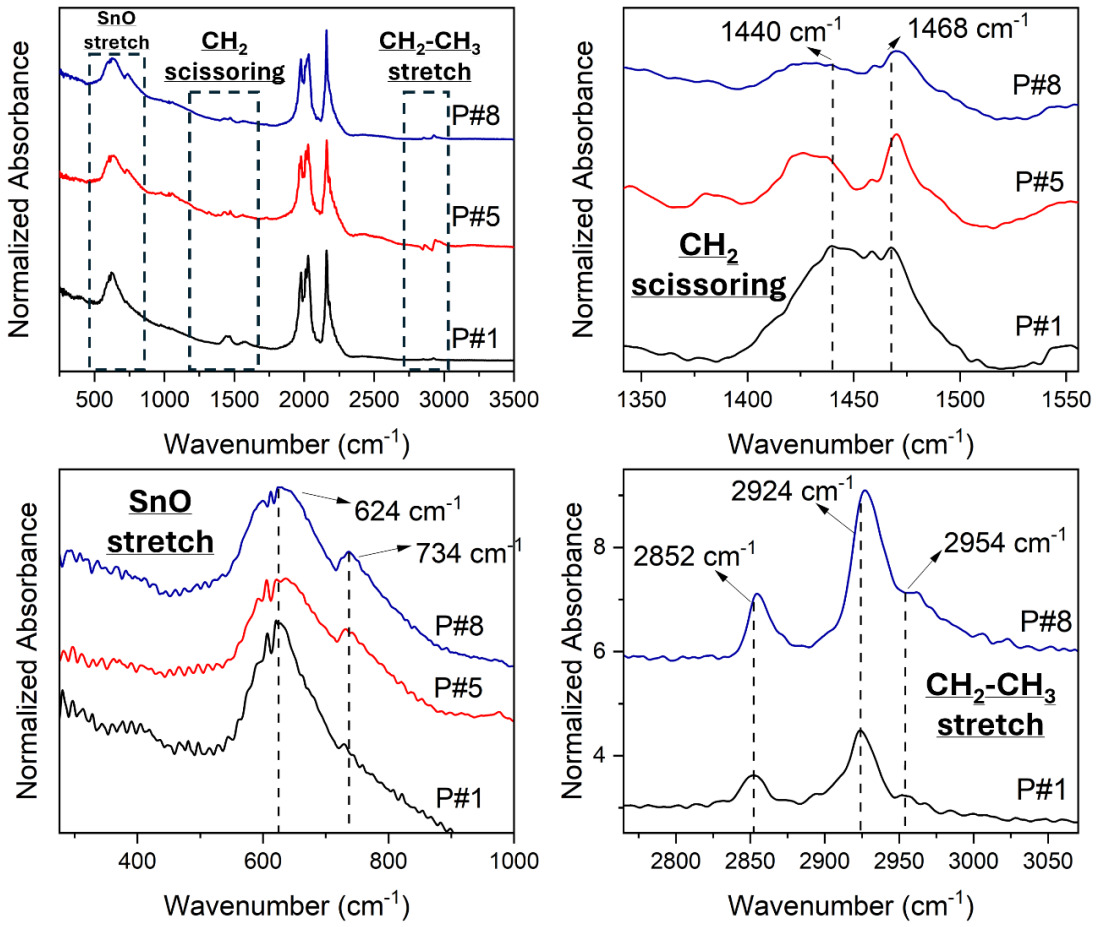

Figure 40. FTIR from 250 to 3500 cm^{-1} of annealed P#1, P#5, and P#8 CTO PSNCs.

The next IR feature is a bit harder to assign. It is a very low intensity broad feature at 1450 cm^{-1} that seems to be composed of two peaks (P#1). It has been assigned to M-O bonds such as those in CdO,[236,238] although it is more likely that these features belong to the bending vibrations (scissoring) of CH_2 moieties. Through the evolution from P#1 to P#5, there is a clear splitting of the two 1440 cm^{-1} and 1468 cm^{-1} features. The 1440 cm^{-1} peak becomes broader and shifts to lower energy, indicating a change in the chemical environment, and or possibly weaking on the CH_2 vibration. The 1468 cm^{-1} peaks broaden slightly and shift to a higher frequency, which also indicates a slow progression towards a different chemical environment.

Lastly, the peaks found in the 2700 cm^{-1} to 3100 cm^{-1} regions are associated with the CH_2-CH_3 stretch, more specifically, the symmetric (2852 cm^{-1}) and asymmetric (2924 cm^{-1}) vibrational modes. Normally these peaks would be of little to no interest, but Meulenberg et al. were able to not only assign all the ligand vibrations in CdSe QDs, but also made some correlations about the crystallinity of the QDs based on these vibrations. They concluded that the splitting of asymmetric peak (Figure 40) indicates hindered chain rotations about the long axis of the ligand.[239] This observation shows that the ligands are locked in position at the surface due to a change in the surface faceting or enhanced crystallinity. The splitting of the asymmetric mode could also explain why the LSPR blue shifts between P#1 and P#5. Surface reconstruction during annealing occurs to accommodate for Sn migrating from a surface site to an antisite, which explains the observations made on the LSPR absorption through reduction of the surface depletion layer, allowing for more activated Sn atoms at the surface that can contribute to the plasmonic response. It is worth noting that no presence of O-H stretching vibrations from hydroxyl groups is found around 3600-3250 cm^{-1}, which is very common in CdO systems synthesized in hydrothermal conditions.[234]

4.4 Conclusions

In conclusion, the annealing of CTO PSNCs allows for a detailed investigation of defect behavior and changes in the plasmonic response. The process of scaling up did not impact the properties of the CTO PSNCs, maintaining properties consistent with previously reported results. Throughout the annealing process, the samples showed an initial shift of the LSPR to higher energy (2208 to 2068 nm) where it remained constant for the first 12 hours, then proceeded to redshift to 2172 from 2068 nm for the next 12 hours, indicating variations in the defect and Sn content within the CTO PSNCs. Initial rapid shifts in LSPR energy suggested fast defect annealing or surface reconstruction within the first hour, followed by a period of LSPR stability, and a notable red shift after 24 hours. Structural analysis through pXRD and TEM confirmed that the overall crystal structure and morphology remained largely unchanged, although slight reductions in size (10.4 to 9.4 nm) and alterations in aspect ratio were observed, correlating with changes in the LSPR extinction. FTIR analysis provided insights into the local chemical environment changes, particularly in Sn-O and CH_2 vibrations, further illustrating the dynamic

evolution of the crystallinity and surface reconstruction during annealing. These findings enhance our understanding of the defect dynamics in CTO PSNCs, potentially guiding future improvements in material design by performing selective annealing during the early stages yielding improved LSPR properties for electronic and optical applications.

CHAPTER 5

STRUCTURE AND CHARACTERIZATION OF TIN (II) FLUORIDE CADMIUM STANNATE NANOCRYSTALS

5.1 Introduction

Introducing fluorine (F) dopants into TCOs to manipulate their optoelectronic properties is a very common practice both in academia and industry. There are proposed mechanisms regarding the role of F in the TCO lattice. The most agreed upon mechanism explains that F atoms can substitute O atoms in the lattice, but can also occupy V_Os, increasing carrier density and carrier mobility, in the process, lowering impurities that function as scattering centers. In thin films and bulk materials, the addition of F can help reduce grain boundaries, thereby increasing carrier density and conductivity.

There are multiple examples of F incorporation into different PSNCs, where F increases carrier density and removes scattering centers. F doping have been used in conjunction with other aliovalent dopants such as in F-Sn:CdO (FICO),[216] F-Sn_2O_3 (FTO),[76,240] and F-Sn:In_2O_3 (FITO)[17] to enhance the optoelectronic properties of these materials. In the FITO system, Milliron and coworkers argue that F substitutes an O site ($F_O^{\cdot}$), providing free electrons and reducing the number of V_Os. Since the scattering of electrons by ionized impurities is related to the square of their ionic charge, fluorine defects scatter electrons less than V_Os. Consequently, F doping can reduce the damping of the LSPR, while maintaining a high concentration of charge carriers. Therefore, the employment and small amount of F, along with other extrinsic or intrinsic dopants, can enhance the plasmonic properties and enhance the faceting of MO_x PSNCs.

With this in mind, the current study investigates the optical and structural properties of CTO PSNCs synthesized using tin (II) fluoride (SnF_2) instead of tin (II) acetate ($SnOAc_2$). These will be referred to as "FCTO" to differentiate them from the CTO synthesized using the acetate precursor, as described in previous chapters. Structural changes are monitored through pXRD, and the oxidation states of Cd and Sn in the FCTO samples are confirmed through XPS measurements. The LSPR differences between CTO and FCTO are monitored through UV-Vis-IR absorption measurements and carrier densities are extracted through m^* determined from MCD. The LSPR extinction can be fit to a 3-mode frequency dependent Drude approximation

(SXDA) to extract *n* and Γ for the face, edge, and corner contributions to the overall LSPR feature. The size and morphology are confirmed through TEM analysis.

5.2 Experimental Methods

5.2.1 Synthesis of FCTO Inverse Spinel PSNCs

The CTO PSNCs were synthesized following the modified method by Strouse and coworkers, where the original Sn(II) acetate source is substituted by a Sn(II) fluoride precursor. In a 3-neck round bottom flask fitted with a condenser and a thermocouple, cadmium acetylacetonate ($Cd(acac)_2$, 1.2 mmol) and tin(II) fluoride (SnF_2, 0.3 mmol) are combined with OA (7.5 mmol) and ODE (25 mL). The solution is degassed at 120 °C for 1 hour, and then rapidly heated to 319 °C where is kept refluxing for 100 minutes until the solution turns dark blue/grey indicating the nucleation of CTO PSNCs. The PSNCs are isolated by addition of IPA, followed by selective precipitation of the smaller CTO in toluene from bigger metallic Cd particles that form as a byproduct. The isolated CTO NCs are then passed through a toluene gel permeation chromatography (GPC) column to remove excess ligand following published procedure. The NCs are kept in toluene or TCE for storage.

5.2.2 General Characterization

Powder X-ray diffraction (pXRD) patterns were collected with a Rigaku MiniFlex powder X-ray diffractometer using a Cu Kα source. The pXRD patterns were collected using a zero-background micro-powder plate. Scans were collected from 15 to 70° at a rate of 7°/min and a 0.05 step size.

UV−Vis−NIR absorbance of purified CTO are dissolved in TCE for all optical measurements. The optical data were collected in a PerkinElmer Lambda 950 spectrometer. A 1 mm path length NIR quartz cuvette was used for all absorbance measurements. Spectra were corrected using TCE.

Size, size dispersity, morphology, and lattice fringe analysis were obtained by transmission electron microscopy (TEM). High-angle annular dark-field scanning transmission electron microscopy (HAADF-STEM) and EDX measurements were performed at 300 kV on an FEI Titan Themis3 (scanning) transmission electron microscope

X-ray photoelectron spectroscopy (XPS) was obtained on FCTO powders deposited on carbon tape using a PHI 5100 X-ray photoelectron spectrometer. The XPS has an excitation source of Mg Kα, with a pass energy of 22.36 eV to minimize linewidth. All samples were calibrated to the aliphatic carbon assignment (C1s 284.8 eV).

5.2.3 Magnetic Circular Dichroism Parameters

Thin film samples of FCTO were prepared in neat toluene and dropcast onto a quartz substrate. The concentration was controlled by measuring the E_g linear absorption feature and maintaining an absorption of between 0.5 – 1.0 absorption units using a Varian Cary 50 Bio spectrophotometer. Afterwards, the substrate was secured onto the sample probe of the optical cryostat using VGE-7031 varnish diffractometer

VH-MCD is performed on a CTO sample dropcast onto a 0.5-inch quartz substrate. The sample was dried under vacuum prior to insertion into an Oxford Instruments 10 T HelioxTL Superconducting Spectromag. A 300 W Newport Xe Arc Lamp (Model 6258) with a monochromator (Model 69931) and optical chopper operating at a frequency of 211 Hz was used in combination with a ThorLabs Glan-Taylor linear polarizer (GLB-10) to linearly polarize incident light, followed by use of a HINDS Instruments photoelastic modulator (PEM-100) for subsequent circular polarization at 47 kHz. Two Stanford Research Systems SR830 Lock-In Amplifiers were phase-locked to the chopper and PEM frequencies to maximize the signal-to-noise for the DC detector spectrum (V_{DC}) and ΔA signal (V_{AC}) obtained, respectively. A Hamamatsu (R928) PMT was used for the UV-Vis region of 4.4 – 2.5 eV with a Femto current amplifier (LCA-200K-20M) to enhance signal generated by the PMT. Temperature was monitored and controlled through a Keck-Clamp fiber cable routed through the sample probe and mounted adjacent to the sample substrate. A positive and negative field sweep scan from 0 - 6 T was performed for the stannate samples at 40 $\pm$ 0.5 K in 2 T intervals. The reported spectra were corrected by subtracting the 0 T scan, to eliminate artifacts from polarization effects, magnetic field inhomogeneity, and other disturbances that may have arisen during MCD measurement. VH-MCD data was used to calculate the effective mass of CTO for each field increment following a previously published procedure.[210]

5.3 Results and Discussion

5.3.1 Characterization of FCTO PSNCs

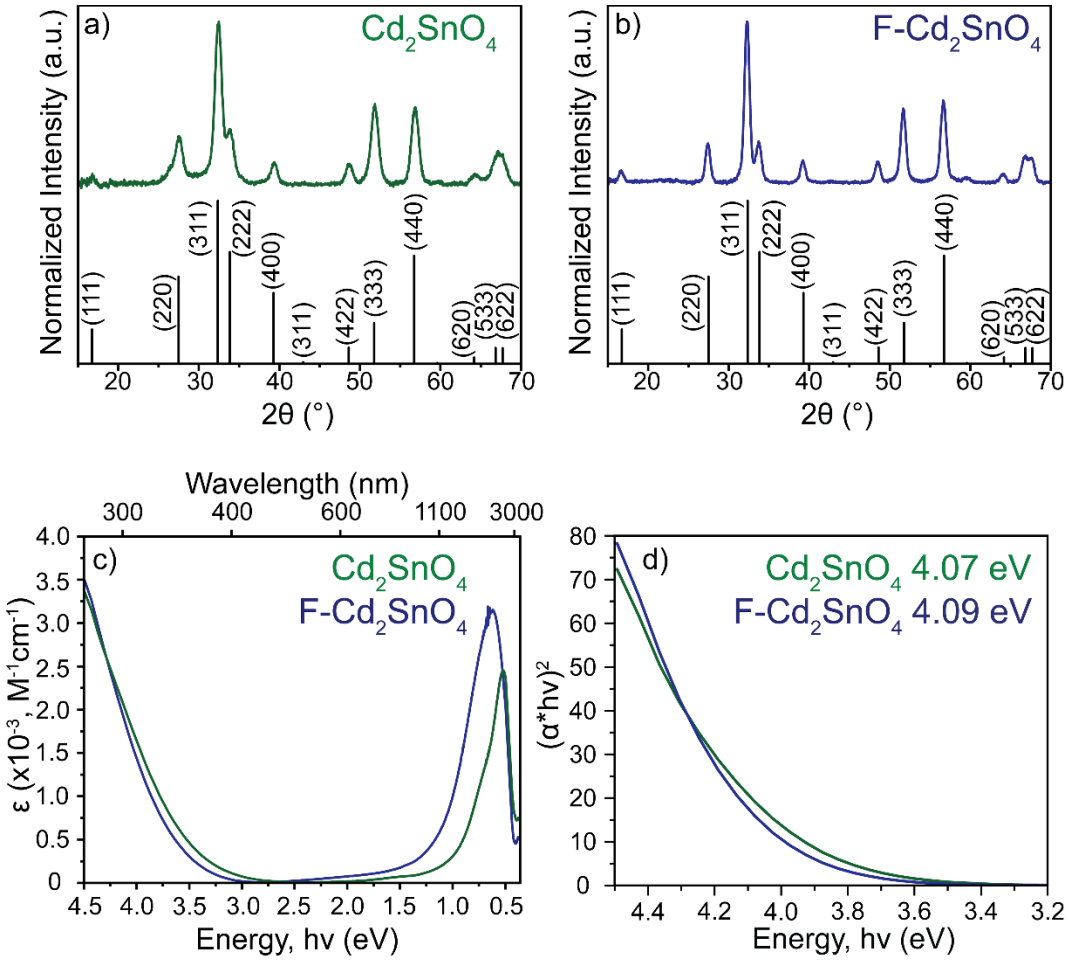

Figure 41. pXRD of (a) CTO and (b) FCTO precursors indexed to the inverse spinel structure (PDF #01-080-1468). Extinction spectra (c) and Tauc plot (d) of CTO and FCTO 2.45x10^{-3} M solutions in TCE.

The syntheses of CTO and FCTO NCs were performed following a modified procedure adapted from Ye and co-workers. The CTO and FCTO samples are ~10 nm in size based on Halder-Wagner fitting on Rigaku software using Si as an external standard (later confirmed by TEM) and can be assigned to an inverse spinel lattice. The pXRD patterns of the CTO made with tin (II) acetate $(SnOAc)_2$ and tin(II) fluoride (SnF_2) can be assigned to the inverse spinel structure with no evidence of impurities or secondary phase.(Figure 41a,b). The relative intensities of the of the (333) and (440) reflections match better with the CTO inverse spinel card (calc. PDF 01-080-1468) in the FCTO PSNCs, suggesting improved crystallinity (Figure 41a,b).

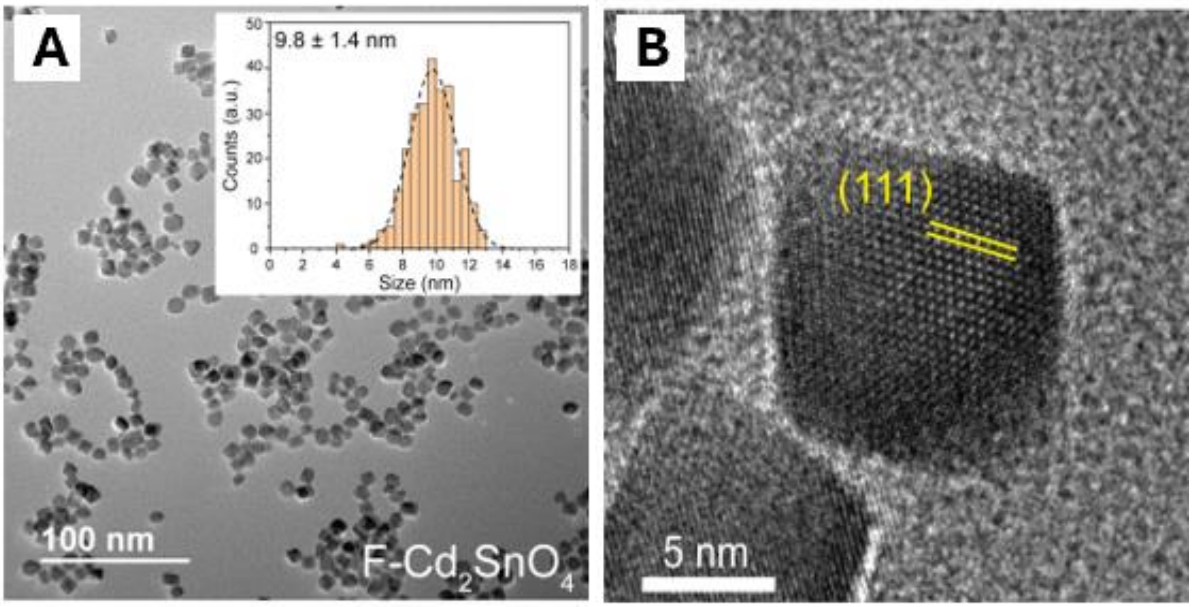

Figure 42. TEM of FCTO (A) with inset showing distribution of PSNC sizes (14 %).and HR-TEM of (B) FCTO with assigned (111) planes.

According to the Drude-Lorentz model,[68] the free carrier properties can be evaluated by changes in the LSPR and band-edge shifts using Tauc plots.[241] To explore these, same concentration (2.45×10^{-3} M) solutions of both samples were made using TCE as solvent. In Figure 1c, the UV-Vis-IR extinction spectra for both NCs can be observed. These materials are highly transparent in the visible region from approximately 1000 to 450 nm, followed by a rapid increase in the absorbance which is assigned as the band edge absorbance. The LSPR for the CTO is centered around 2450 nm with an extinction value of 2448 $M^{-1}cm^{-1}$. In contrast, the FCTO has a higher energy LSPR centered at 1950 nm with an extinction of 3150 $M^{-1}cm^{-1}$ and much broader FWHM. This might suggest that the difference in LSPR is due to *in situ* formation of HF by heating SnF_2 at high temperatures in the presence of carboxylic acid, which leads to more faceted NCs and removal of oxygen vacancies (V_O) and defects at the NC surface. It is also worth noting that the F ions can modify the surface of the FCTO samples, leading to different facets being expressed in the FCTO compared to the CTO particles, which will influence the m^* of the material as the free carriers may have different momenta as they travel through different directions in the crystal.[50] A direct Tauc plot (Fig. 41d) shows a slight blueshift of the optical bandgap from 4.07 eV (CTO) to 4.09 eV (FCTO) in conjunction with an isosbestic point at 290 nm. The blueshift of the optical band gap and the LSPR energy can be an indication of higher free carrier concentrations in the

FCTO NCs. According to the Drude model (Equation 4), this is only accurate if the carrier m^*, is constant between PSNCs.

To elucidate the size, size distribution, and morphology of these materials, TEM and HR-TEM graphs were collected for FCTO. The FCTO has shorter octahedral PSNCs with sharper corners and better-defined faces. The sizes of the FCTO are 9.8 ± 1.4 nm and are slightly shorter than the CTO samples reported in previous chapters. The FCTO PSNCs have flatter corners in the (001) plane (tips). The HR-TEM reveals different oriented fringes with d-spacing of 3.24 Å, 2.65 Å, and 1.77 Å corresponding to the (220), (222), and (511) reflections respectively. No apparent carbon coating or layer in the PSNCs is observed in any of the images.

The XPS allows for investigation of any differences in Cd, Sn oxidation states between CTO and FCTO, and it can detect any presence of F that can exist in the FCTO PSNCs. The XPS data can be interpreted by looking at the Cd, Sn, and O spectra before and after sputtering. The sputtering process allows for the removal of extra layers of the material allowing for a deeper penetration of X-rays.

In the XPS Cd spectra for the CTO (43a) and FCTO (43c), both Cd $3d_{3/2}$ and $3d_{5/2}$ peaks have two contributions that are assigned to Cd(II) in the core, and Cd(II) containing ligands (Cd-ligand) at the surface. In both samples, the Cd-ligand is present, but contributions to the Cd-ligand are greater in the FCTO samples. In both samples the feature with lower energy was assigned to Cd-ligand because when the samples are sputtered (43b, d) the peaks at 411.5 eV and 406.5 eV are removed and only the Cd(II) peaks at 412.5 eV and 405.5 eV remain. This suggests that there is a small layer of leftover $Cd(OAc_2)$ or $(Cd(acac)_2)$ on the surface, or a Cd(II)-rich surface that is more predominant in the FCTO than the CTO PSNCs.

Similarly, the Sn spectra of CTO (Figure 43a) and FCTO (Figure 43c) shows the Sn $3d_{3/2}$ and $3d_{5/2}$ peaks that are assigned to the Sn(IV) and Sn(II) oxidation states. The Sn(IV) signal occurs at 495.0 eV and 486.0 eV, assigned by sputtering the surface and removing the contribution from the Sn(II) signal at 496.0 eV and 4875 eV (Figure 43b,d). It can be inferred that the signal that

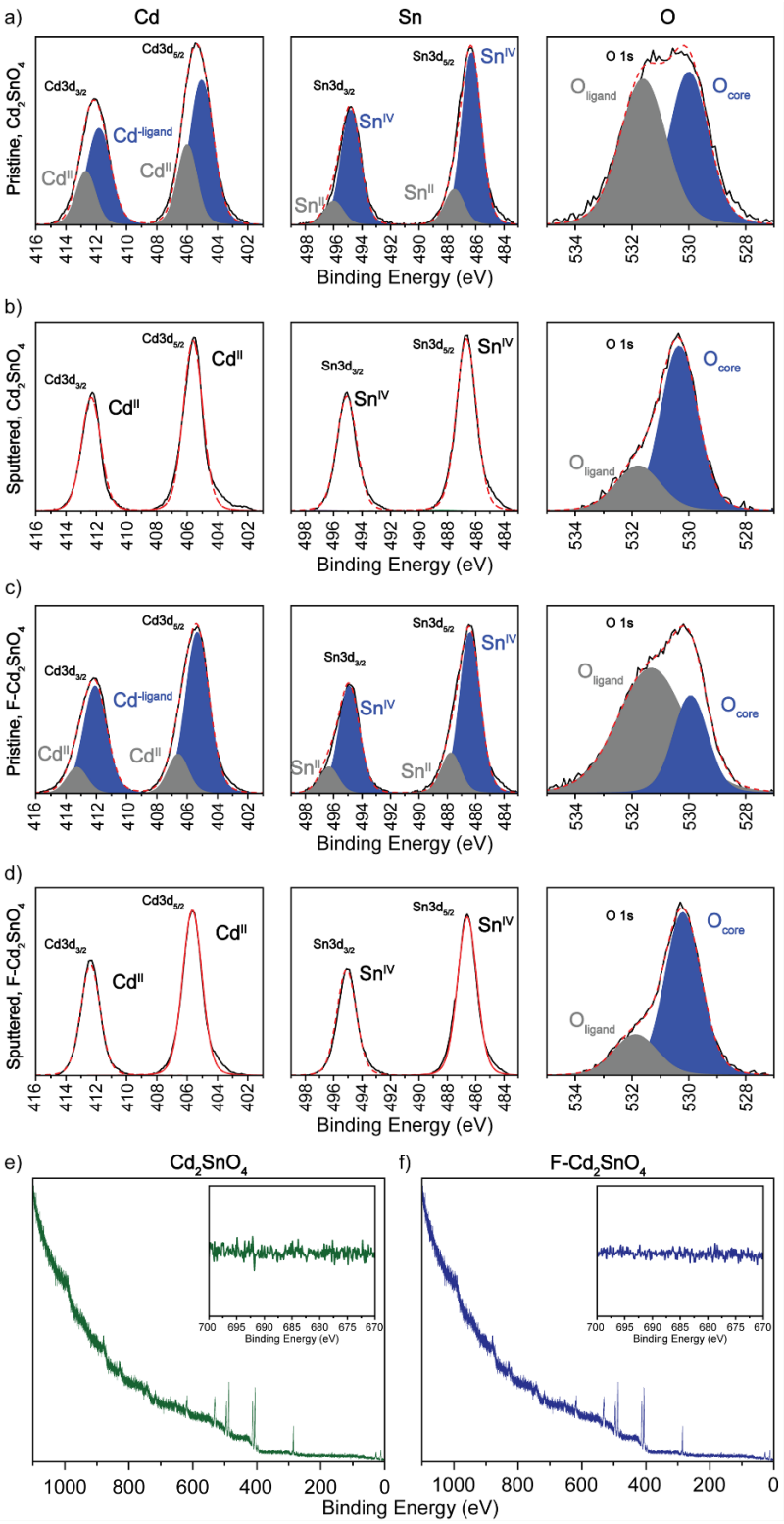

Figure 43. XPS data of Cd $3d_{3/2}$, $3d_{5/2}$; Sn $3d_{3/2}$, $3d_{5/2}$; O 1s of CTO before (a) and after sputtering (b). FCTO before (c) before and after sputtering (d). Survey scan of CTO (e) and F-Cd_2SnO_4 (f) with an inset from 700 to 670 eV showing the energy region where the F 1S transition occurs. No peak is observed at 684 eV corresponding to this feature.

disappears after sputtering is coming from Sn (II), as the preferred oxidation state of Sn in CTO is Sn(IV), and it's also confirmed through ^{119}Sn SSNMR measurements in the pristine CTO PSNCs (Figure 25). The presence Sn(II) species at the surface suggest that there are possible Sn(II) moieties, such as $Sn(oleate)_2$ and $Sn(acac)_2$, that are either unreacted leftover species, or a thin layer of Sn(II) at the surface where is readily available to be oxidize, reducing Cd(II) to Cd (0) in the process, leaving behind a Sn(IV) atoms that dictate CTO growth.

The most significant effects are observed in the O 1s spectra (Figure 43 a,c). The peak was deconvoluted into two components: one from oxygen atoms in the ligand and the other from oxygen atoms within the CTO crystal lattice. The O 1s spectra are widely used in literature to quantify V_Os, and it is likely that the signal attributed to the O-ligand partially includes contributions from V_Os. The key observation is that the relative intensity of the O-ligand signal is significantly stronger in the FCTO sample compared to the CTO sample. This indicates that F atoms either remove surface ligands or contribute to V_Os. The rationale for fitting the O 1s signal to V_O, ligand, and core oxygen is that the ligand peak's intensity significantly diminishes after sputtering. Given that XPS is a surface-sensitive technique, this reduction suggests that the signal predominantly arises from oxygen species at the surface rather than V_Os. Additionally, it is noteworthy that the spectra for both CTO and FCTO samples appear very similar, indicating that the effects of F in the CTO are not changes in Sn(IV) or Cd(II) content.

Lastly, the full XPS spectra of the CTO and FCTO are plotted (Figure 43e, f) to show the whole scan regime from 0 to 1200 eV. The inset as shown from 700 to 670 eV shows no peak at 684 eV, which is the typically binding energy regime for F 1S signal. This observation indicates that the F atoms are not incorporated into the crystal lattice as suggested in thin-films and in FITO nanocubes.[17,242]

The main impact on the SnF_2 precursor in the FCTO PSNCs in comparison to the regular CTO is the improved faceting and crystallinity. There are two mechanisms that could play a role in these observations: 1) As previously suggested, SnF_2 is an ionic salt that isn't soluble in non-polar solvents such as OA and ODE. It stays solid in solution even at 120 °C under low pressure. The SnF_2 only becomes soluble in the OA/ODE mixture when it reaches reflux temperatures of ~ 319 °C. At this point, the SnF_2 dissociates and the Sn^{2+} atoms contribute to the formation of the CTO lattice by introducing itself into the CdO crystal, here the Sn(II) species reduces a Cd(II) to Cd(0), inducing the release of metallic Cd and leaving a Cd(IV) increasing Sn_{Cd} content, then free

F^- in solutions react with free H^+ from OA forming HF in-situ. It has been previously observed that formation of HF during and after NC growth can induce faceting, but can also etch the NC surface, thereby reducing the amount of defects.[243] 2) In contrast to SnF_2, the $Sn(OAc)_2$ forms Sn (II) oleate ($Sn(OA)_2$) in the presence of OA at 120 °C under low pressure.[244] The $(SnOAc)_2$ is a more reactive species than SnF_2, which in turn releases Sn^{2+} at a slower rate, thereby slowing down the formation of the FCTO monomers allowing for the growth of bigger particles. The slower step of the SnF_2 dissociation is reflected in the average time it requires for the nucleation of the CTO when using the acetate vs. the SnF_2.

.

5.3.2 MCD Measurements of FCTO

VH-MCD was performed from +6 to -6 T in intervals of 2 T for a total of seven spectra performed in triplicate, where concurrent absorbance spectra (Figure 44, top) and VHMCD spectra (Figure 44, bottom) are compared. The absorbance spectra are extremely similar as a function of field and MCD signal increases as a function of increasing applied magnetic field as expected. Each magnetic field spectra were run in triplicate and averaged together to enhance the signal-to-noise ratio.

Through VH-MCD, the optical bandgap ($E_{g,opt}$) absorption edge is analyzed, where simulated MCD curves can be fit to the observed feature to extract a Zeeman splitting energy assuming the RS approximation holds true. To improve accuracy of calculations, the Zeeman splitting energy for each field pair (e.g. +2 and -2 T) were averaged together. From the Zeeman splitting energy, m^* is calculated through Equation 12. The results are plotted in Figure 44 where the Zeeman splitting energy can be fit within error to a linear regression. From all calculated m^* values, a mean effective mass of 0.006 ± 0.004 m^*/m_e was found which is 3× as low as previously published results on ($Sn(acetate)_2$) precursor synthesized CTO The lower mass reported in the FCTO (0.006) vs. CTO (0.022) helps explain why there are higher LSPR energies in the FCTO when compared to the CTO PSNCs. According to the Drude model, this change in frequency is a direction observation of lower m^*, if n remains constant. The changes in m^* might be due to differences in faceting due to surface modification induced by F etching of metal atoms, as observed in InP QDs.[245] According to band theory, the charge carriers will experience different m^* values depending on the k-space projection in which travel. Materials expressing

different effective masses depending on facet concentration have been suggested in theoretical literature, and hasn't been studied experimentally in depth.[50]

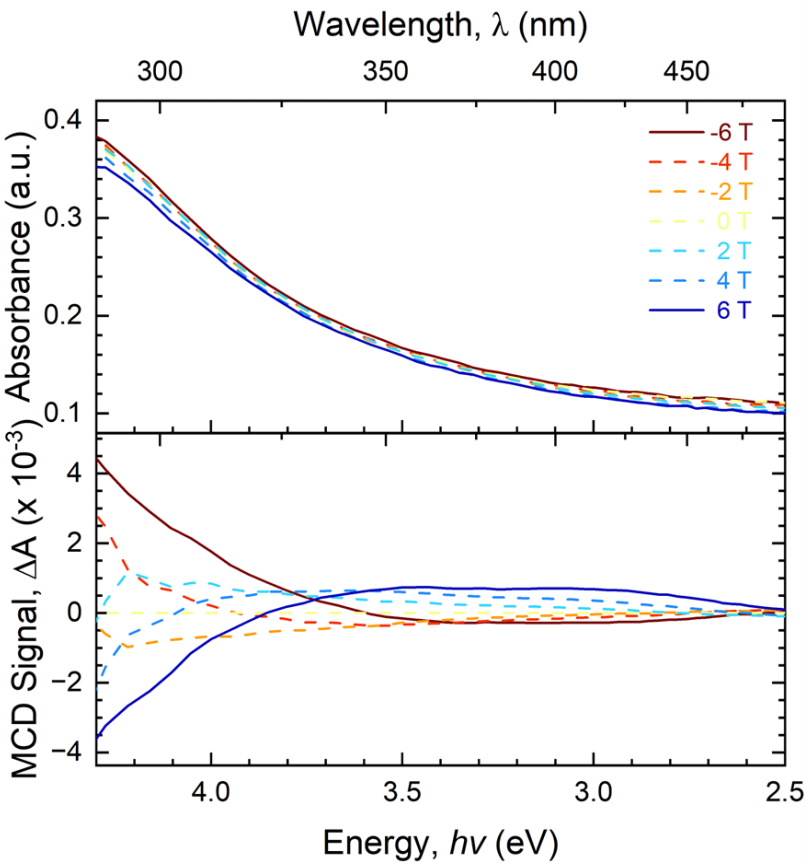

Figure 44. Linear absorption (top) was monitored for thin-film FCTO PSNCs, where the $E_{g,opt}$ edge is visible between 4.3 – 2.5 eV. VH-MCD (bottom) within the same spectral range exhibits an inflection point observed at 3.8 eV at maximum field. All data were averaged in triplicate for each magnetic field point between +6 to -6 T.

5.3.3 Frequency Dependent Drude Fits of CTO

The absorption spectra for CTO and FCTO were compared utilizing a frequency-dependent Drude modeling MATLAB code, adopted from prior work in the Milliron Research Group. Despite the increase in total damping (increase of FWHM, which is dependent on damping and m^*) for FCTO vs. CTO, a simple Drude approximation deconvolution result in face and edge modes having similar damping parameters. While FCTO does have slightly lower damping parameters, this difference alone is not enough to account for the m^* difference observed between FCTO and CTO.

Frequency-dependent Drude modeling was performed on the two different CTO PSNCs and compared directly with one another in Figure 45, where the fitting parameters are compiled in Table 5 for direct comparison. FCTO produces a higher Q-factor LSPR due to the combination of greater carrier density and lower damping contribution from Γ(face), Γ(edge), but not Γ(corner) compared to regular CTO.

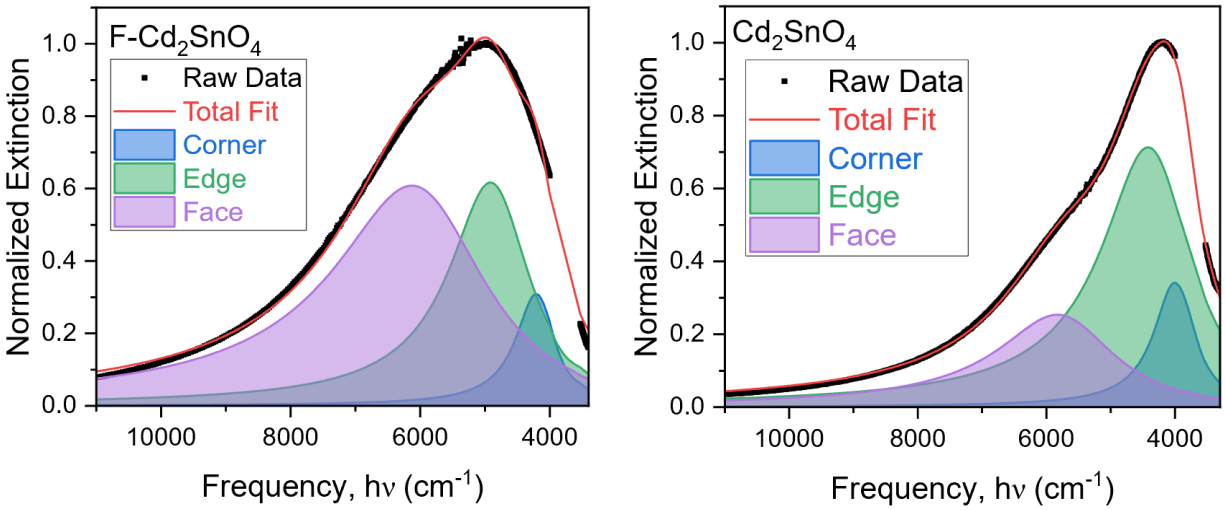

Figure 45. The LSPR extinction feature for FCTO and CTO were quantified using the frequency dependent Drude model. The fitting parameters for frequencies and damping factors are placed in Table 5. Good agreement is seen between the fitting and the experimentally observed extinction feature

In comparing FCTO and CTO, the changes in synthetic conditions for PSNC formation result in minor differences in the damping contributions of the LSPR for face and edge components of the octahedral LSPR modes. However, when comparing SDA deconvolutions, an increase in overall broadening for FCTO appears to be attributable to an increase in availability (volume fraction) of the facial mode compared to CTO, rather than an overall increase in damping. The difference between Γ(face), Γ(edge), and Γ(corner) directly correlate with the location of activated carrier species in the nanocrystal and subsequent degree of spectral anisotropy observed in the LSPR. As the Γ difference between Γ(face),and Γ(edge) is lower for the FCTO than the CTO PSNC, the distribution of activated carrier species in the FCTO material clearly possesses more activated carriers on that specific facet of the nanocrystal. On the opposite side, Γ(corner) its lower in the CTO than the FCTO. This suggests that there are more active carriers at the corners of the CTO rather than the FCTO. These differences should be

detectable through EELS spectroscopy because the near-field enhancement (NFE) may be greater at the tips of the CTO.

5.3.4 Transient Absorption Dynamics of CTO

The fsTA spectra of CTO and FCTO are presented in Figure 46. Both samples were analyzed using a 1600 nm pump, with absorption monitored from 300 to 700 nm. In the top figure, CTO, when pumped at 1600 nm, shows a feature at 350 nm that grows with a positive ΔA on the fs timescale, followed by a bleach as it approaches the ns timescale. FCTO exhibits similar behavior under the same conditions. Following pump excitation, a prominent feature at 350 nm grows and then splits into two distinct features, at 350 nm and 400 nm, between the fs and ns regimes. This behavior is correlated to hot-carrier generation through the excitation of the localized surface plasmon resonance (LSPR) feature.

Table 5. Frequency dependent Drude fitting parameters

Sample	**Face ω_p**	**Edge ω_p**	**Corner ω_p**	**Face Γ**	**Edge Γ**	**Corner Γ**
CTO (cm^{-1})	12692.5	14000.0	18466.7	769.571	1696.03	2213.23
FCTO (cm^{-1})	13336.2	15567.3	19408.8	753.929	1513.91	2853.48

From the lifetime of the 350 nm excitation in Figure 46 (bottom), the bi-exponential dynamics corresponding to electron-phonon (*el-ph*) and phonon-phonon (*ph-ph*) interactions are calculated and tabulated in Table 6. Both CTO (green) and FCTO (blue) exhibit similar behaviors up to the 100 ps range, where there is a sudden inversion of the decay behavior, which was completely unexpected. A deeper understanding of the carrier's behavior in these materials is required to explain this inversion in lifetime behavior.

The lifetime of the *el-ph* interaction is 184 fs for CTO and 192 fs for FCTO, indicating a slightly longer hot-carrier lifetime in FCTO. This is crucial for applications where long-lived hot carriers are needed to perform work, catalysis, and electron injection. The significant difference between the two samples lies in the *ph-ph* interaction lifetime, which measures the thermalization of heat in the lattice. FCTO shows a much shorter *ph-ph* lifetime compared to CTO (141.6 ps vs. 250.0 ps), demonstrating that FCTO is more efficient at removing heat from

the lattice. This suggests that F alters the phonon energy dynamics within the CTO lattice by removing V_O, or affecting the facet expression in FCTO, enhancing its thermal properties and capabilities.

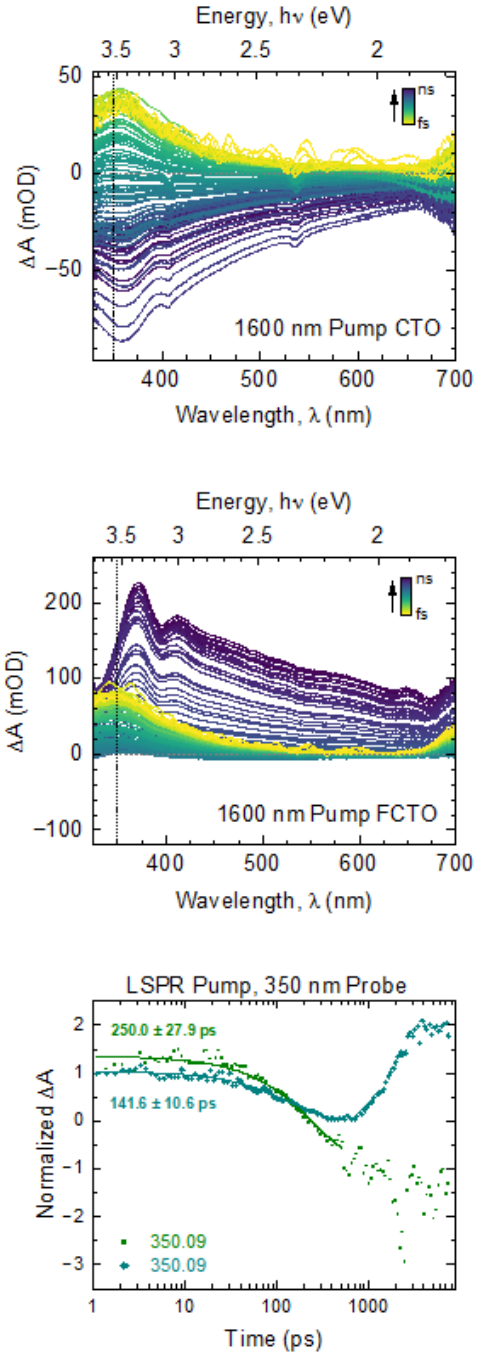

Figure 46. fsTA of CTO and FCTO PSNCs was performed under LSPR pumping conditions. All spectra show high energy PIA signatures above 500 nm, while the LSPR pumped regime shows an additional bleach at lower energy. Lifetime analysis is shown in green (CTO) and blue (FCTO) for pumped regime, where characteristic bi-exponential decay dynamics are observed/

Table 6. Tabulated *el-ph* and *ph-ph* lifetime values for CTO and FCTO

350 nm probe	$\tau_{el\text{-}ph}$ (fs)	$\tau_{ph\text{-}ph}$ (ps)
CTO	184 ± 5.8	250.0 ± 27.9
FCTO	192 ± 6.4	141.6 ± 10.6

5.4 Conclusions

The incorporation of dopants into TCOs to modify their optoelectronic properties is a well-established approach in both academic research and industrial applications. The application of SnF_2 to synthesize CTO PSNCs, referred to as FCTO, is employed to study the effects of F on the structural and optical properties CTO PSNCs. The results demonstrate significant improvements in LSPR energy, *m**, and fsTA dynamics due to utilization of SnF_2, although no evidence of F doping into the CTO lattice was observed with XPS or NMR.

In this study, the synthesis of FCTO was achieved using a SnF_2 precursor instead of $Sn(OAc)_2$. Structural changes were monitored using pXRD, which confirmed the improved crystallinity of the FCTO samples. The oxidation states Cd and Sn in the FCTO samples were verified using XPS, and the differences in LSPR between CTO and FCTO were analyzed through UV-Vis-IR absorption measurements. Carrier *m** were determined using MCD, showing that FCTO had a significantly lower *m** than CTO (0.022 vs. 0.006 m^*/m_e respectively), explaining the higher LSPR energies observed in FCTO.

TEM in conjunction with pXRD, revealed that FCTO nanocrystals exhibit improved faceting and similar shapes to CTO, with FCTO particles showing rounded corners and well-defined faces. The XPS data indicated that the use of SnF_2 results in a higher presence of Cd-ligands at the surface and a more significant reduction of Sn(II) to Sn(IV), suggesting the presence of a thin layer of unreacted species or a Cd(II) rich surface in FCTO. Additionally, the O 1s spectra suggested that fluorine atoms remove surface ligands or contribute to the formation of oxygen vacancies.

The main mechanistic explanation of the difference between CTO and FCTO is attributed to the slower dissociation rate of SnF_2 compared to $Sn(OAc)_2$, leading to a more controlled formation of CTO monomers and the subsequent growth of nanocrystals. The inclusion of fluorine in the reaction mixture (not in the resulting PSNC) also enhances the phonon energy

dynamics within the CTO lattice, improving its thermal properties and making FCTO more efficient at removing heat from the lattice.

In conclusion, this work provides the groundwork to understand the mechanisms in which F addition can help control and improve the structural and optoelectronic properties of TCOs. These findings demonstrate the potential of FCTO nanocrystals for applications requiring enhanced plasmonic properties, higher carrier densities, improved hot carrier generation, and faster heat dissipation which are all critical to the development of TCOs for PSNC applications.

CHAPTER 6

FUTURE WORK

The main goal of this thesis is to understand the optoelectronic properties novel TCO PSNCs. There's still much work to be done in these plasmonic systems, and there's always room for further understanding. The following are brief explanations, descriptions, and motivations for future work.

6.1 Understanding the Growth of CTO PSNCs

It is possible to synthesize CTO, and CdO PSNCs that are well-formed, and have competitive size distributions. Although this is possible, there is currently no understanding on how these PSNCs form and grow. The CTO PSNCs do not follow regular nucleation theory. Chemists making QDs and PSNCs take advantage of understanding the growth mechanism to control the size and dispersity of NPs. This is not the case in CTO PSNCs, where the nucleation event occurs instantly after a certain amount of time is reached after reflux. The reason for nucleation, what induces this nucleation event, and the reaction kinetics are unknown at this point. It is suspected that this reaction is autocatalytic in nature. In the autocatalytic mechanism, the surface of the formed NPs enhances the decomposition of the existing precursor in solution leading to enhanced growth. One proposed mechanism is that with enough time a critical Sn concentration will be reached inside small CdO seeds to form Sn:CdO or CTO PSNCs. The initial formation of nuclei will drive the reaction to completion, which is why the nucleation event seems spontaneous and requires a long time (~70 minutes) for completion.

6.2 Coupling of LSPR with Lanthanides Optical Properties in TCO

Due to reasons that currently escape the scope of current work, materials that exhibit LSPR usually are not luminescent, and vice versa. Therefore, it is of great interest to study materials that are both luminescent and plasmonic to see if coupling between the LSPR and

emissive states can either enhance or allow further tunning of the optical responses of these materials. Based on previous work, it is possible to doped non-plasmonic wide E_g transparent oxides, such as Zn_2AlO_4,[246] ZnO,[45] Y_2O_3,[247] CdO,[248] and many others with Ln(III) ions to act as highly efficient phosphor materials. Current research efforts in this area focus on coupling plasmonic noble metal NPs with different Lns through cation exchange or through different methods such as core-shells or thin film assemblies. CTO and CdO PSNCs offer great opportunities for coupling for LSPRs with the emissive properties of Lns as they can accommodate dopant ions into their crystal lattices. The are currently efforts to couple LSPRs with Ln emission for down[249] and up-converting[250] phosphors, and there is ample potential for TCO PSNCs to serve as targets for these applications.

6.3 Development of New TCO PSNCs

There are other possible TCOs that can be PSNCs, yet they have not been synthesized colloidally. Although the work here focused on the Cd-Sn-O system, analog systems such as the Zn-Sn-O exist and have not been studied at the nano scale. Initial studies on CdO, CTO, Sn_2O_3, and ITO indicate interest in these TCOs. However, other TCOs different from CTO and ITO became less relevant as they did not exhibit competitive optoelectronic properties. The Zn_2SnO_4 (ZTO) inverse spinel structure has been synthesized in solid-state, thin film, and even at the nanoscale through solgel and solvothermal techniques.[35,251–253] The ZTO PSNCs have not been successfully synthesized through colloidal routes, and no well-formed particles have been reported to the same degree as those for CTO PSNCs. Although not detailed in this work, significant effort was devoted to the synthesis of these novel ZTO PSNCs using colloidal methods.

6.4 Investigation of LSPR in PSNCs Through Novel Spectroscopic Techniques

The plasmonic properties of various PSNCs are commonly analyzed through extinction experiments in the UV-Vis-NIR region of the electromagnetic spectrum. There are numerous

avenues available to understand the nature of the LSPR response in PSNCs. For instance, magnetic circular dichroism (MCD) has become a widely accepted technique to determine the m^* of different PSNCs through optical methods, which was previously considered a niche technique for non-plasmonic systems. Similarly, EPR is typically used to study chemical reactions involving radicals or EPR-active metals such as Mn, Fe, Co, Ni, and other species with unpaired electrons. Free carriers, in principle, can be investigated through EPR spectroscopy. Numerous literature reports discuss the assignment of V_O due to the equilibrium with the singly ionized vacancy, which is EPR active. The understanding of these features and their correlation to the LSPR response is still highly debated in the literature. Therefore, there is significant room to explore size effects, carrier origin, and surface vs. core effects through EPR spectroscopy.

Raman spectroscopy is another technique that remains underexplored for the analysis of plasmonic materials. The shift in frequency for certain Raman modes can be correlated to changes in n in thin films. Thus, it is reasonable to assume that these techniques should also be applicable to TCO PSNCs.

REFERENCES

(1) Sui, M.; Kunwar, S.; Pandey, P.; Lee, J. Strongly Confined Localized Surface Plasmon Resonance (LSPR) Bands of Pt, AgPt, AgAuPt Nanoparticles. *Sci Rep* **2019**, *9* (1), 16582.

(2) Agrawal, A.; Cho, S. H.; Zandi, O.; Ghosh, S.; Johns, R. W.; Milliron, D. J. Localized Surface Plasmon Resonance in Semiconductor Nanocrystals. *Chem. Rev.* **2018**, *118* (6), 3121–3207.

(3) Lv, S.; Du, Y.; Wu, F.; Cai, Y.; Zhou, T. Review on LSPR Assisted Photocatalysis: Effects of Physical Fields and Opportunities in Multifield Decoupling. *Nanoscale Adv.* **2022**, *4* (12), 2608–2631.

(4) Verma, R.; Belgamwar, R.; Polshettiwar, V. Plasmonic Photocatalysis for CO_2 Conversion to Chemicals and Fuels. *ACS Materials Lett.* **2021**, *3* (5), 574–598.

(5) Saylan, Y.; Akgönüllü, S.; Denizli, A. Plasmonic Sensors for Monitoring Biological and Chemical Threat Agents. *Biosensors* **2020**, *10* (10), 142.

(6) Homola, J. Surface Plasmon Resonance Sensors for Detection of Chemical and Biological Species. *Chem. Rev.* **2008**, *108* (2), 462–493.

(7) Tandon, B.; Lu, H.-C.; Milliron, D. J. Dual-Band Electrochromism: Plasmonic and Polaronic Mechanisms.

(8) Runnerstrom, E. L.; Llordés, A.; Lounis, S. D.; Milliron, D. J. Nanostructured Electrochromic Smart Windows: Traditional Materials and NIR-Selective Plasmonic Nanocrystals. *Chem. Commun.* **2014**, *50* (73), 10555–10572.

(9) Liu, Y.; Huang, L.; Cao, S.; Chen, J.; Zou, B.; Li, H. Plasmonic-Based Electrochromic Materials and Devices. *Nanophotonics* **2024**, *13* (2), 155–172.

(10) Alonso Calafell, I.; Cox, J. D.; Radonjić, M.; Saavedra, J. R. M.; García de Abajo, F. J.; Rozema, L. A.; Walther, P. Quantum Computing with Graphene Plasmons. *npj Quantum Inf* **2019**, *5* (1), 1–7.

(11) Bozhevolnyi, S. I.; Mortensen, N. A. Plasmonics for Emerging Quantum Technologies. *Nanophotonics* **2017**, *6* (5), 1185–1188.

(12) Xia, Y.; Halas, N. J. Shape-Controlled Synthesis and Surface Plasmonic Properties of Metallic Nanostructures. *MRS Bull.* **2005**, *30* (5), 338–348.

(13) Jain, P. K.; Huang, X.; El-Sayed, I. H.; El-Sayed, M. A. Noble Metals on the Nanoscale: Optical and Photothermal Properties and Some Applications in Imaging, Sensing, Biology, and Medicine. *Acc. Chem. Res.* **2008**, *41* (12), 1578–1586.

(14) Moores, A.; Goettmann, F. The Plasmon Band in Noble Metal Nanoparticles: An Introduction to Theory and Applications. *New J. Chem.* **2006**, *30* (8), 1121.

(15) Cleret de Langavant, C.; Oh, J.; Lochon, F.; Tusseau-Nenez, S.; Ponsinet, V.; Baron, A.; Gacoin, T.; Kim, J. Near-Infrared Dual-Band LSPR Coupling in Oriented Assembly of Doped Metal Oxide Nanocrystal Platelets. *Nano Lett.* **2024**, *24* (10), 3074–3081.

(16) Lounis, S. D.; Runnerstrom, E. L.; Llordés, A.; Milliron, D. J. Defect Chemistry and Plasmon Physics of Colloidal Metal Oxide Nanocrystals. *J. Phys. Chem. Lett.* **2014**, *5* (9), 1564–1574.

(17) Agrawal, A.; Singh, A. A.; Yazdi, S.; Singh, A. A.; Ong, G. K.; Bustillo, K.; Johns, R. W.; Ringe, E.; Milliron, D. J. Resonant Coupling between Molecular Vibrations and Localized Surface Plasmon Resonance of Faceted Metal Oxide Nanocrystals. *Nano Letters* **2017**, *17* (4), 2611–2620.

(18) Liu, Z.; Zhong, Y.; Shafei, I.; Borman, R.; Jeong, S.; Chen, J.; Losovyj, Y.; Gao, X.; Li, N.; Du, Y.; Sarnello, E.; Li, T.; Su, D.; Ma, W.; Ye, X. Tuning Infrared Plasmon Resonances in Doped Metal-Oxide Nanocrystals through Cation-Exchange Reactions. *Nat Commun* **2019**, *10* (1), 1394.

(19) Tandon, B.; Ghosh, S.; Milliron, D. J. Dopant Selection Strategy for High-Quality Factor Localized Surface Plasmon Resonance from Doped Metal Oxide Nanocrystals. *Chemistry of Materials* **2019**, *31* (18), 7752–7760.

(20) Mott, N. F. Impurity Band Conduction. Experiment and Theorythe Metal-Insulator Transition in an Impurity Band. *J. Phys. Colloques* **1976**, *37* (C4), C4-301-C4-306.

(21) Pergament, A.; Stefanovich, G.; Markova, N. The Mott Criterion: So Simple and yet so Complex. arXiv November 23, 2014.

(22) Kanehara, M.; Koike, H.; Yoshinaga, T.; Teranishi, T. Indium Tin Oxide Nanoparticles with Compositionally Tunable Surface Plasmon Resonance Frequencies in the Near-IR Region. *J. Am. Chem. Soc.* **2009**, *131* (49), 17736–17737.

(23) Zhu, L.; Mao, Z.; Li, P.; Xu, M.; Meng, Z.; Chen, L.; Zhao, B. Modulating Carrier Density of the $(Ag)_x(MoO_3)_y$ System to Enhance SERS:Localized Surface Plasmon Resonance Contribution. *Journal of Materiomics* **2023**, *9* (2), 387–394.

(24) Zhang, X.-Y.; Han, D.; Ma, N.; Gao, R.; Zhu, A.; Guo, S.; Zhang, Y.; Wang, Y.; Yang, J.; Chen, L. Carrier Density-Dependent Localized Surface Plasmon Resonance and Charge Transfer Observed by Controllable Semiconductor Content. *J. Phys. Chem. Lett.* **2018**, *9* (20), 6047–6051.

(25) Chen, L.; Hu, H.; Chen, Y.; Gao, J.; Li, G. Plasmonic $Cu_{2-x}S$ Nanoparticles: A Brief Introduction of Optical Properties and Applications. *Materials Advances* **2021**, *2* (3), 907–926.

(26) Luther, J. M.; Jain, P. K.; Ewers, T.; Alivisatos, A. P. Localized Surface Plasmon Resonances Arising from Free Carriers in Doped Quantum Dots. *Nature Mater* **2011**, *10* (5), 361–366.

(27) Chavan, G. T.; Kim, Y.; Khokhar, M. Q.; Hussain, S. Q.; Cho, E.-C.; Yi, J.; Ahmad, Z.; Rosaiah, P.; Jeon, C.-W. A Brief Review of Transparent Conducting Oxides (TCO): The Influence of Different Deposition Techniques on the Efficiency of Solar Cells. *Nanomaterials (Basel)* **2023**, *13* (7), 1226.

(28) Príncipe, J.; Duarte, V. C. M.; Mendes, A.; Andrade, L. Influence of the Transparent Conductive Oxide Type on the Performance of Inverted Perovskite Solar Cells. *ACS Appl. Energy Mater.* **2023**, *6* (24), 12442–12451.

(29) Grundmann, M. Karl Bädeker (1877-1914) and the Discovery of Transparent Conductive Materials: Karl Bädeker. *Phys. Status Solidi A* **2015**, *212* (7), 1409–1426.

(30) Bädeker, K. Über die elektrische Leitfähigkeit und die thermoelektrische Kraft einiger Schwermetallverbindungen. *Annalen der Physik* **1907**, *327* (4), 749–766.

(31) Haacke, G. Transparent Conducting Coatings. **1977**, *7*, 73–93.

(32) Holland, L.; Siddall, G. The Properties of Some Reactively Sputtered Metal Oxide Films. *Vacuum* **1953**, *3* (4), 375–391.

(33) Kane, J.; Schweizer, H. P.; Kern, W. Chemical Vapor Deposition of Antimony-Doped Tin Oxide Films Formed from Dibutyl Tin Diacetate. *J. Electrochem. Soc.* **1976**, *123* (2), 270.

(34) Asha Bhardwaj; Bhardwaj, A.; Banshi D. Gupta; Gupta, B. K.; A. Raza; A. Raza; A. Raza; Raza, A.; Anurag Sharma; Sharma, A.; Sharma, A. K.; Sharma, A. K.; O.P. Agnihotri; Agnihotri, O. P. Fluorine-Doped SnO_2 Films for Solar Cell Application. *Solar Cells* **1981**, *5* (1), 39–49.

(35) Coutts, T. J.; Young, D. L.; Li, X.; Mulligan, W. P.; Wu, X. Search for Improved Transparent Conducting Oxides: A Fundamental Investigation of CdO, Cd_2SnO_4, and Zn_2SnO_4. *Journal of Vacuum Science & Technology A* **2000**, *18* (6), 2646–2660.

(36) Koffyberg, F. P. Electron Concentration and Mobility in Semimetallic CdO. *Can. J. Phys.* **1971**, *49* (4), 435–440.

(37) Watanabe, H.; Wada, M.; Takahashi, T. Optical and Electrical Properties of ZnO Crystals. *Jpn. J. Appl. Phys.* **1964**, *3* (10), 617.

(38) Hahn, E. E. Some Electrical Properties of Zinc Oxide Semiconductor. *Journal of Applied Physics* **1951**, *22* (7), 855–863.

(39) Hada, T.; Wasa, K.; Hayakawa, S. Structures and Electrical Properties of Zinc Oxide Films Prepared by Low Pressure Sputtering System. *Thin Solid Films* **1971**, *7* (2), 135–145.

(40) Itoyama, K. Properties of Sn-Doped Indium Oxide Prepared by High Rate and Low Temperature RF Sputtering. *Jpn. J. Appl. Phys.* **1978**, *17* (7), 1191.

(41) Fan, J. C. C.; Goodenough, J. B. X-ray Photoemission Spectroscopy Studies of Sn-doped Indium-oxide Films. *Journal of Applied Physics* **1977**, *48* (8), 3524–3531.

(42) Kane, J.; Schweizer, H. P.; Kern, W. Chemical Vapor Deposition of Transparent Electrically Conducting Layers of Indium Oxide Doped with Tin. *Thin Solid Films* **1975**, *29* (1), 155–163.

(43) Ponja, S. D.; Sathasivam, S.; Parkin, I. P.; Carmalt, C. J. Highly Conductive and Transparent Gallium Doped Zinc Oxide Thin Films via Chemical Vapor Deposition. *Sci Rep* **2020**, *10* (1), 638.

(44) Khan, S.; Stamate, E. Comparative Study of Aluminum-Doped Zinc Oxide, Gallium-Doped Zinc Oxide and Indium-Doped Tin Oxide Thin Films Deposited by Radio Frequency Magnetron Sputtering. *Nanomaterials (Basel)* **2022**, *12* (9), 1539.

(45) Conti, C. R.; McBride, J. R.; Strouse, G. F. Examining the Effect of Dopant Ionic Radius on Plasmonic M:ZnO Nanocrystals (M = Al^{3+}, Ga^{3+}, In^{3+}). *J. Phys. Chem. C* **2021**, *125* (14), 7772–7779.

(46) Singleton, J. *Band Theory and Electronic Properties of Solids*, 1st edition.; Oxford University Press: Oxford ; New York, 2001.

(47) Kittel, C. *Introduction to Solid State Physics*, 8th edition.; Wiley: Hoboken, NJ, 2004.

(48) Holgate, S. *Understanding Solid State Physics*, 1st ed.; CRC Press, 2009.

(49) Tang, M.; Shang, J.; Zhang, Y. Density Functional Theory Analysis of Electronic Structure and Optical Properties of La Doped Cd_2SnO_4 Transparent Conducting Oxide. *Chinese Physics B* **2018**, *27* (1).

(50) Lin, R.; Wan, J.; Xiong, Y.; Wu, K.; Cheong, W.; Zhou, G.; Wang, D.; Peng, Q.; Chen, C.; Li, Y. Quantitative Study of Charge Carrier Dynamics in Well-Defined WO_3 Nanowires and Nanosheets: Insight into the Crystal Facet Effect in Photocatalysis. *J. Am. Chem. Soc.* **2018**, *140* (29), 9078–9082.

(51) Arduca, E.; Perego, M. Doping of Silicon Nanocrystals. *Materials Science in Semiconductor Processing* **2017**, *62*, 156–170.

(52) Cheng, C.; Fang, Q.; Fernandez-Alberti, S.; Long, R. Controlling Charge Carrier Trapping and Recombination in $BiVO_4$ with the Oxygen Vacancy Oxidation State. *J. Phys. Chem. Lett.* **2021**, *12* (14), 3514–3521.

(53) Deák, P.; Aradi, B.; Frauenheim, T. Quantitative Theory of the Oxygen Vacancy and Carrier Self-Trapping in Bulk TiO_2. *Phys. Rev. B* **2012**, *86* (19), 195206.

(54) Han, S.; Flewitt, A. J. Analysis of the Conduction Mechanism and Copper Vacancy Density in P-Type Cu_2O Thin Films. *Sci Rep* **2017**, *7* (1), 5766.

(55) Amini, M. N.; Dixit, H.; Saniz, R.; Lamoen, D.; Partoens, B. The Origin of P-Type Conductivity in ZnM_2O_4 (M = Co, Rh, Ir) Spinels. *Phys. Chem. Chem. Phys.* **2014**, *16* (6), 2588–2596.

(56) Kuo, P. H.; Du, J. Lithium Ion Diffusion Mechanism and Associated Defect Behaviors in Crystalline $Li_{1+x}Al_xGe_{2-x}(PO_4)_3$ Solid-State Electrolytes. *J. Phys. Chem. C* **2019**, *123* (45), 27385–27398.

(57) Cho, S.; Kim, Y.; DiVenere, A.; Wong, G. K.; Ketterson, J. B.; Meyer, J. R. Antisite Defects of Bi_2Te_3 Thin Films. *Applied Physics Letters* **1999**, *75* (10), 1401–1403.

(58) Hussain, A.; Mian, S. A.; Ahmed, E.; Jang, J. Orchestrating the Impact of Antisites and Vacancy Defects on the Elastic and Optoelectronic Properties of Boron Arsenide. *J Mol Model* **2023**, *29* (12), 393.

(59) Mekuye, B.; Abera, B. Nanomaterials: An Overview of Synthesis, Classification, Characterization, and Applications. *Nano Select* **2023**, *4* (8), 486–501.

(60) Ferrari, M. Introduction to Nanotechnology. Charles P. Poole, Jr., and Frank J. Owens. Hoboken, NJ: John Wiley & Sons, 2003, 400 Pp., $79.95, Hardcover. ISBN 0-471-07935-9. *Clinical Chemistry* **2004**, *50* (5), 981–981.

(61) Gibbs, S. L.; Staller, C. M.; Milliron, D. J. Surface Depletion Layers in Plasmonic Metal Oxide Nanocrystals. *Acc. Chem. Res.* **2019**, *52* (9), 2516–2524.

(62) Shubert-Zuleta, S.; Segui Barragan, V.; Berry, M.; Russum, R.; Milliron, D. How Depletion Layers Govern the Dynamic Plasmonic Response of In-Doped CdO Nanocrystals. February 20, 2024.

(63) Staller, C. M.; Robinson, Z. L.; Agrawal, A.; Gibbs, S. L.; Greenberg, B. L.; Lounis, S. D.; Kortshagen, U. R.; Milliron, D. J. Tuning Nanocrystal Surface Depletion by Controlling Dopant Distribution as a Route Toward Enhanced Film Conductivity. *Nano Lett.* **2018**, *18* (5), 2870–2878.

(64) Roscow, J. I.; Bowen, C. R.; Almond, D. P. Breakdown in the Case for Materials with Giant Permittivity? *ACS Energy Lett.* **2017**, *2* (10), 2264–2269.

(65) Hassan, S. ul; Farid, M. A.; Wang, Y. A Series of Lanthanide–Quinoxaline-2,3(1H,4H)-Dione Complexes Containing 1D Chiral Ln_2O_3 (Ln = Eu, Tb, Sm, Dy) Chains: Luminescent Properties and Response to Small Molecules. *RSC Adv.* **2021**, *11* (53), 33309–33318.

(66) Choi, H.; Raabe, I.; Kim, D.; Teocoli, F.; Kim, C.; Song, K.; Yum, J.-H.; Ko, J.; Nazeeruddin, Md. K.; Grätzel, M. High Molar Extinction Coefficient Organic Sensitizers for Efficient Dye-Sensitized Solar Cells. *Chemistry – A European Journal* **2010**, *16* (4), 1193–1201.

(67) Han, X. X.; Rodriguez, R. S.; Haynes, C. L.; Ozaki, Y.; Zhao, B. Surface-Enhanced Raman Spectroscopy. *Nat Rev Methods Primers* **2022**, *1* (1), 1–17.

(68) Drude, P. Zur Elektronentheorie Der Metalle. *Annalen der Physik* **1900**, *306* (3), 566–613.

(69) Conti III, C. R.; Quiroz-Delfi, G.; Schwarck, J. S.; Chen, B.; Strouse, G. F.; R. Conti III, C.; Quiroz-Delfi, G.; S. Schwarck, J.; Chen, B.; F. Strouse, G. Carrier Density, Effective Mass, and Nuclear Relaxation Pathways in Plasmonic Sn:In_2O_3 Nanocrystals. *The Journal of Physical Chemistry C* **2020**, *124* (51), 28220–28229.

(70) Jang, Y. H.; Jang, Y. J.; Kim, S.; Quan, L. N.; Chung, K.; Kim, D. H. Plasmonic Solar Cells: From Rational Design to Mechanism Overview. *Chem. Rev.* **2016**, *116* (24), 14982–15034.

(71) F. Carvalho, W. O.; Mejía-Salazar, J. R. Plasmonics for Telecommunications Applications. *Sensors* **2020**, *20* (9), 2488.

(72) De Trizio, L.; Buonsanti, R.; Schimpf, A. M.; Llordes, A.; Gamelin, D. R.; Simonutti, R.; Milliron, D. J. Nb-Doped Colloidal TiO_2 Nanocrystals with Tunable Infrared Absorption. *Chem. Mater.* **2013**, *25* (16), 3383–3390.

(73) Imanaka, Y.; Oshikiri, M.; Takehana, K.; Takamasu, T.; Kido, G. Cyclotron Resonance in N-Type ZnO. *Physica B: Condensed Matter* **2001**, *298* (1), 211–215.

(74) Department of Physics, Government General Degree College Singur, 712409, West Bengal, India; Das, A. Removal of Defects in CdO Nanoparticle and Rapid Synthesis of CdO Nanoflake Using Novel Microwave Technique to Improve Semiconductor Device Performance. *IJST* **2021**, *14* (10), 858–868.

(75) Lyons, J. L. Self-Trapped Holes and Polaronic Acceptors in Ultrawide-Bandgap Oxides. *Journal of Applied Physics* **2022**, *131* (2), 025701.

(76) Cho, S. H.; Ghosh, S.; Berkson, Z. J.; Hachtel, J. A.; Shi, J.; Zhao, X.; Reimnitz, L. C.; Dahlman, C. J.; Ho, Y.; Yang, A.; Liu, Y.; Idrobo, J. C.; Chmelka, B. F.; Milliron, D. J. Syntheses of Colloidal F:In_2O_3 Cubes: Fluorine-Induced Faceting and Infrared Plasmonic Response. *Chemistry of Materials* **2019**, *31* (7), 2661–2676.

(77) Piontkowski, Z. T.; Runnerstrom, E. L.; Cleri, A.; McDonald, A.; Ihlefeld, J.; Saltonstall, C.; Maria, J.-P.; Beechem, T. E. Effects of Strain, Disorder, and Coulomb Screening on Free-Carrier Mobility in Doped Cadmium Oxide. *Journal of Applied Physics* **2021**, *130* (19), 195105.

(78) Crouch Holler, S. *Principles of Instrumental Analysis, 6th Edition*, 6th edition.; Thomson Brooks/Cole, 2007.

(79) *NMR Spectroscopy: Basic Principles, Concepts and Applications in Chemistry, 3rd Edition | Wiley*. Wiley.com.

(80) MacKenzie, K. J. D.; Smith, M. E. *Multinuclear Solid-State NMR of Inorganic Materials*, 1st ed.; Pergamon materials series; Pergamon: Oxford ; New York, 2002.

(81) Marbella, L. E.; Millstone, J. E. NMR Techniques for Noble Metal Nanoparticles. *Chem. Mater.* **2015**, *27* (8), 2721–2739.

(82) Leroy, C.; Bryce, D. L. Recent Advances in Solid-State Nuclear Magnetic Resonance Spectroscopy of Exotic Nuclei. *Progress in Nuclear Magnetic Resonance Spectroscopy* **2018**, *109*, 160–199.

(83) Yesinowski, J. P.; Purdy, A. P. Defect Dynamics Observed by NMR of Quadrupolar Nuclei in Gallium Nitride. *J. Am. Chem. Soc.* **2004**, *126* (30), 9166–9167.

(84) Jung, W.-S.; Han, O. H.; Chae, S.-A. Characterization of Wurtzite Indium Nitride Synthesized from Indium Oxide by In-115 MAS NMR Spectroscopy. *Materials Letters* **2007**, *61* (16), 3413–3415.

(85) Sears, R. E. J. Al 27 Nuclear-Magnetic Shielding in Aluminum Group-V Semiconductors. *Phys. Rev. B* **1980**, *22* (3), 1135–1140.

(86) Wolf, D. *Spin-Temperature and Nuclear-Spin Relaxation in Matter: Basic Principles and Applications*; International series of monographs on physics; Clarendon Press; Oxford University Press: Oxford : New York, 1979.

(87) Korringa, J. Nuclear Magnetic Relaxation and Resonnance Line Shift in Metals. *Physica* **1950**, *16* (7), 601–610.

(88) Yesinowski, J. P. Solid-State NMR of Inorganic Semiconductors. In *Peptide-Based Materials*; 2011; Vol. 310, pp 229–312.

(89) Conti III, C. R.; Quiroz-Delfi, G.; Schwarck, J. S.; Chen, B.; Strouse, G. F. Carrier Density, Effective Mass, and Nuclear Relaxation Pathways in Plasmonic Sn:In_2O_3 Nanocrystals. *J. Phys. Chem. C* **2020**, *124* (51), 28220–28229.

(90) Marbella, L. E.; Gan, X. Y.; Kaseman, D. C.; Millstone, J. E. Correlating Carrier Density and Emergent Plasmonic Features in $Cu_{2-x}Se$ Nanoparticles. *Nano Lett.* **2017**, *17* (4), 2414–2419.

(91) Look, D. C. NMR Determination of the Conduction-Electron Hyperfine Interaction in Crystalline CdO. *Phys. Rev.* **1969**, *184* (3), 705–708.

(92) Hahn, E. L. Spin Echoes. *Phys. Rev.* **1950**, *80* (4), 580–594.

(93) Hung, I.; Gan, Z. On the Practical Aspects of Recording Wideline QCPMG NMR Spectra. *J Magn Reson* **2010**, *204* (2), 256–265.

(94) Zhang, S.; Meier, B. H.; Ernst, R. R. Polarization Echoes in NMR. *Phys. Rev. Lett.* **1992**, *69* (14), 2149–2151.

(95) O'Dell, L. A.; Schurko, R. W. QCPMG Using Adiabatic Pulses for Faster Acquisition of Ultra-Wideline NMR Spectra. *Chemical Physics Letters* **2008**, *464* (1), 97–102.

(96) O'Dell, L. A.; Rossini, A. J.; Schurko, R. W. Acquisition of Ultra-Wideline NMR Spectra from Quadrupolar Nuclei by Frequency Stepped WURST-QCPMG. *Chemical Physics Letters* **2009**, *468*, 330–335.

(97) MacGregor, A. W.; O'Dell, L. A.; Schurko, R. W. New Methods for the Acquisition of Ultra-Wideline Solid-State NMR Spectra of Spin-1/2 Nuclides. *Journal of Magnetic Resonance* **2011**, *208* (1), 103–113.

(98) Schurko, R. W. Ultra-Wideline Solid-State NMR Spectroscopy. *Acc. Chem. Res.* **2013**, *46* (9), 1985–1995.

(99) Kaduk, J. A.; Billinge, S. J. L.; Dinnebier, R. E.; Henderson, N.; Madsen, I.; Černý, R.; Leoni, M.; Lutterotti, L.; Thakral, S.; Chateigner, D. Powder Diffraction. *Nat Rev Methods Primers* **2021**, *1* (1), 1–22.

(100) Shrivastav, A. M.; Cvelbar, U.; Abdulhalim, I. A Comprehensive Review on Plasmonic-Based Biosensors Used in Viral Diagnostics. *Commun Biol* **2021**, *4* (1), 70.

(101) Cohen, N.; Zussman, A.; Sarusi, G. A Monolithic LWIR/NIR Multispectral QWIP for Night Vision and See Spot. *Infrared Physics & Technology* **2001**, *42* (3–5), 391–396.

(102) Villuendas, H.; Vilches, C.; Quidant, R. Standardization of *In Vitro* Studies for Plasmonic Photothermal Therapy. *ACS Nanosci. Au* **2023**, *3* (5), 347–352.

(103) Zhong, Y.; Liu, Z.; Sarnello, E.; Li, T.; Liu, Y.; Chen, J.; Ye, X. Controlling Infrared Plasmon Resonances in Inverse-Spinel Cadmium Stannate Nanocrystals via Site-Selective Cation-Exchange Reactions. *Chemistry of Materials* **2021**, *33* (6), 1954–1963.

(104) Gordon, T. R.; Paik, T.; Klein, D. R.; Naik, G. V.; Caglayan, H.; Boltasseva, A.; Murray, C. B. Shape-Dependent Plasmonic Response and Directed Self-Assembly in a New Semiconductor Building Block, Indium-Doped Cadmium Oxide (ICO). *Nano Letters* **2013**, *13* (6), 2857–2863.

(105) Liu, Z.; Zhong, Y.; Shafei, I.; Jeong, S.; Wang, L.; Nguyen, H. T.; Sun, C. J.; Li, T.; Chen, J.; Chen, L.; Losovyj, Y.; Gao, X.; Ma, W.; Ye, X. Broadband Tunable Mid-Infrared Plasmon Resonances in Cadmium Oxide Nanocrystals Induced by Size-Dependent Nonstoichiometry. *Nano Letters* **2020**, *20* (4), 2821–2828.

(106) Manthiram, K.; Alivisatos, A. P. Tunable Localized Surface Plasmon Resonances in Tungsten Oxide Nanocrystals. *J. Am. Chem. Soc.* **2012**, *134* (9), 3995–3998.

(107) Conti, C. R.; McBride, J. R.; Strouse, G. F. Examining the Effect of Dopant Ionic Radius on Plasmonic M:ZnO Nanocrystals (M = Al^{3+}, Ga^{3+}, In^{3+}). *J. Phys. Chem. C* **2021**, *125* (14), 7772–7779.

(108) Anitha, M.; Saravanakumar, K.; Anitha, N.; Amalraj, L. Influence of Fluorine Doped CdO Thin Films by an Simplified Spray Pyrolysis Technique Using Nebulizer. *Opt Quant Electron* **2019**, *51* (6), 187.

(109) Kim, B. H.; Staller, C. M.; Cho, S. H.; Heo, S.; Garrison, C. E.; Kim, J.; Milliron, D. J. High Mobility in Nanocrystal-Based Transparent Conducting Oxide Thin Films. *ACS Nano* **2018**, *12* (4), 3200–3208.

(110) Yu, W.; Lee, J. G.; Joo, Y.-H.; Hou, B.; Um, D.-S.; Kim, C.-I. Etching Characteristics and Surface Properties of Fluorine-Doped Tin Oxide Thin Films under CF_4-Based Plasma Treatment. *Appl. Phys. A* **2022**, *128* (10), 942.

(111) Vidhya, S. N.; Balasundaram, O. N.; Chandramohan, M. Structural and Optical Investigations of Gallium Doped Tin Oxide Thin Films Prepared by Spray Pyrolysis. *Journal of Saudi Chemical Society* **2016**, *20* (6), 703–710.

(112) Saha, J. K.; Bukke, R. N.; Mude, N. N.; Jang, J. Significant Improvement of Spray Pyrolyzed ZnO Thin Film by Precursor Optimization for High Mobility Thin Film Transistors. *Sci Rep* **2020**, *10* (1), 8999.

(113) Kim, J.; Agrawal, A.; Krieg, F.; Bergerud, A.; Milliron, D. J. The Interplay of Shape and Crystalline Anisotropies in Plasmonic Semiconductor Nanocrystals. *Nano Letters* **2016**, *16* (6), 3879–3884.

(114) Petrini, N.; Ghini, M.; Curreli, N.; Kriegel, I. Optical Modeling of Plasmonic Nanoparticles with Electronically Depleted Layers. *J. Phys. Chem. C* **2023**, *127* (3), 1576–1587.

(115) Roman, B. J.; Shubert-Zuleta, S. A.; Shim, G.; Kyveryga, V.; Faris, M.; Milliron, D. J. Facet-Enhanced Dielectric Sensitivity in Plasmonic Metal Oxide Nanocubes. *Journal of Physical Chemistry C* **2023**, *127* (5), 2456–2463.

(116) Liu, Z.; Beaulac, R. Nature of the Infrared Transition of Colloidal Indium Nitride Nanocrystals: Nonparabolicity Effects on the Plasmonic Behavior of Doped Semiconductor Nanomaterials. *Chem. Mater.* **2017**, *29* (17), 7507–7514.

(117) Lee, J. T.; Hati, S.; Fahey, M. M.; Zaleski, J. M.; Sardar, R. Surface-Ligand-Controlled Enhancement of Carrier Density in Plasmonic Tungsten Oxide Nanocrystals: Spectroscopic Observation of Trap-State Passivation *via* Multidentate Metal Phosphonate Bonding. *Chem. Mater.* **2022**, *34* (7), 3053–3066.

(118) Kuszynski, J. E.; Kays, J. C.; Conti, C. R.; McGill, S. A.; Dennis, A. M.; Strouse, G. F. Effective Mass for Holes in Paramagnetic, Plasmonic Cu_5FeS_4 Semiconductor Nanocrystals. *J. Phys. Chem. C* **2022**, *126* (30), 12669–12679.

(119) Kuszynski, J. E.; Fabiano, C. J.; Nguyen, E. T.; Mao, K.; Ahuja, A. K.; Schaller, R. D.; Strouse, G. F. Plasmon-Induced Hot-Carrier Excited-State Dynamics in Plasmonic Semiconductor Nanocrystals. *J. Phys. Chem. C* **2023**, *127* (46), 22654–22661.

(120) Shi, Y.; Ndione, P. F.; Lim, L. Y.; Sokaras, D.; Weng, T.-C.; Nagaraja, A. R.; Karydas, A. G.; Perkins, J. D.; Mason, T. O.; Ginley, D. S.; Zunger, A.; Toney, M. F. Self-Doping and Electrical Conductivity in Spinel Oxides: Experimental Validation of Doping Rules. *Chem. Mater.* **2014**, *26* (5), 1867–1873.

(121) Foley, M. E.; Meulenberg, R. W.; McBride, J. R.; Strouse, G. F. Eu^{3+}-Doped ZnB_2O_4 (B = Al^{3+}, Ga^{3+}) Nanospinels: An Efficient Red Phosphor. *Chemistry of Materials* **2015**, *27* (24), 8362–8374.

(122) Hardy, D. A.; Tigaa, R. A.; McBride, J. R.; Ortega, R. E.; Strouse, G. F. Structure-Function Correlation: Engineering High Quantum Yields in Down-Shifting Nanophosphors. *Journal of the American Chemical Society* **2019**, *141* (51), 20416–20423.

(123) Da Silva, M. N.; De Carvalho, J. M.; De Abreu Fantini, M. C.; Chiavacci, L. A.; Bourgaux, C. Nanosized $ZnGa_2O_4$:Cr^{3+} Spinels as Highly Luminescent Materials for Bioimaging. *ACS Appl. Nano Mater.* **2019**, *2* (11), 6918–6927.

(124) Yang, W. C.; Xie, Y. T.; Zhu, W. K.; Park, K.; Chen, A. P.; Losovyj, Y.; Li, Z.; Liu, H. M.; Starr, M.; Acosta, J. A.; Tao, C. G.; Li, N.; Jia, Q. X.; Heremans, J. J.; Zhang, S. X. Epitaxial Thin Films of Pyrochlore Iridate $Bi_{2+x}Ir_{2-y}O_7$-δ: Structure, Defects and Transport Properties. *Sci Rep* **2017**, *7* (1), 7740.

(125) Zhang, S. B.; Wei, S.-H. Self-Doping of Cadmium Stannate in the Inverse Spinel Structure. *Applied Physics Letters* **2002**, *80* (8), 1376–1378.

(126) Urso, C.; Barawi, M.; Gaspari, R.; Sirigu, G.; Kriegel, I.; Zavelani-Rossi, M.; Scotognella, F.; Manca, M.; Prato, M.; De Trizio, L.; Manna, L. Colloidal Synthesis of Bipolar Off-Stoichiometric Gallium Iron Oxide Spinel-Type Nanocrystals with Near-IR Plasmon Resonance. *Journal of the American Chemical Society* **2017**, *139* (3), 1198–1206.

(127) Hartman, S. T.; Pilania, G. Defect Thermodynamics in Spinel Oxides Leading to Plasmonic Behavior. *J. Phys. Chem. Solids* **2022**, *168*, 110822.

(128) Dou, Y.; Egdell, R. G. *N*-Type Doping in Cd_2SnO_4: A Study by EELS and Photoemission. *Phys. Rev. B* **1996**, *53* (23), 15405–15408.

(129) Mulligan, W. P.; Coutts, T. J. Measurement of the Effective Mass of Transparent Conducting Films of Cadmium Tin Oxide. *MRS Proc.* **1997**, *471*, 117.

(130) Leja, E.; Stapiński, T.; Marszalek, K. Electrical and Optical Properties of Conducting N-Type Cd_2SnO_4 Thin Films. *Thin Solid Films* **1985**, *125* (1), 119–122.

(131) Haacke, G.; Mealmaker, W. E.; Siegel, L. A. Sputter Deposition and Characterization of Cd2SnO4 Films. *Thin Solid Films* **1978**, *55* (1), 67–81.

(132) Nozik, A. J. Optical and Electrical Properties of Cd_2SnO_4: A Defect Semiconductor. *Physical Review B* **1972**, *6* (2), 453–459.

(133) Haacke, G. Transparent Electrode Properties of Cadmium Stannate. *Applied Physics Letters* **1976**, *28* (10), 622–623.

(134) Siegel, L. A. A Spinel Form of Cadmium Stannate. *Journal of Applied Crystallography* **1978**, *11* (4), 284–286.

(135) Schimpf, A. M.; Thakkar, N.; Gunthardt, C. E.; Masiello, D. J.; Gamelin, D. R. Charge-Tunable Quantum Plasmons in Colloidal Semiconductor Nanocrystals. *ACS Nano* **2014**, *8* (1), 1065–1072.

(136) Burstein, E. Anomalous Optical Absorption Limit in InSb. *Phys. Rev.* **1954**, *93* (3), 632–633.

(137) Moss, T. S. The Interpretation of the Properties of Indium Antimonide. *Proc. Phys. Soc. B* **1954**, *67* (10), 775–782.

(138) Casabianca, L. B. Solid-State Nuclear Magnetic Resonance Studies of Nanoparticles. *Solid State Nuclear Magnetic Resonance* **2020**, *107*, 101664.

(139) Knight, W. D. Nuclear Magnetic Resonance Shift in Metals. *Phys. Rev.* **1949**, *76* (8), 1259–1260.

(140) Abragam, A. *The Principles of Nuclear Magnetism*; Clarendon Press: Oxford, 1961.

(141) Slichter, C. P. The Knight Shift—a Powerful Probe of Condensed-Matter Systems. *Philosophical Magazine B: Physics of Condensed Matter; Statistical Mechanics, Electronic, Optical and Magnetic Properties* **1999**, *79* (9), 1253–1261.

(142) Van Der Klink, J. J.; Buttet, J.; Graetzel, M. Knight Shift in Small Platinum Particles. *Phys. Rev. B* **1984**, *29* (11), 6352–6355.

(143) Rhodes, H. E.; Wang, P. K.; Stokes, H. T.; Slichter, C. P.; Sinfelt, J. H. NMR of Platinum Catalysts. I. Line Shapes. *Physical Review B* **1982**, *26* (7), 3559–3568.

(144) Taylor, R. E.; Alkan, F.; Koumoulis, D.; Lake, M. P.; King, D.; Dybowski, C.; Bouchard, L.-S. A Combined NMR and DFT Study of Narrow Gap Semiconductors: The Case of PbTe. *J. Phys. Chem. C* **2013**, *117* (17), 8959–8967.

(145) Ganguly, B. N. Nuclear-Spin Relaxation and Knight Shift in Transition Metals. *Phys. Rev. B* **1973**, *8* (3), 1055–1060.

(146) Titman, J. M. Nuclear Magnetic Resonance in Liquid Metals and Alloys. *Physics Reports* **1977**, *33* (1), 1–50.

(147) Levin, E. M.; Cook, B. A.; Ahn, K.; Kanatzidis, M. G.; Schmidt-Rohr, K. Electronic Inhomogeneity and Ag:Sb Imbalance of $Ag_{1-y}Pb_{18}Sb_{1+z}Te_{20}$ High-Performance Thermoelectrics Elucidated by T 125 e and P 207 b NMR. *Phys. Rev. B* **2009**, *80* (11), 115211.

(148) Schurko, R. W. Acquisition of Wideline Solid-State NMR Spectra of Quadrupolar Nuclei. In *eMagRes*; John Wiley & Sons, Ltd, 2011.

(149) Bennett, L. H.; Watson, R. E.; Carter, G. C. Relevance of Knight Shift Measurements to the Electronic Density of States. *Journal of Research of the National Bureau of Standards Section A: Physics and Chemistry* **1970**, *74A* (4), 569.

(150) Shen, Y.; Roberge, A.; Tan, R.; Gee, M. Y.; Gary, D. C.; Huang, Y.; Blom, D. A.; Benicewicz, B. C.; Cossairt, B. M.; Greytak, A. B. Gel Permeation Chromatography as a Multifunctional Processor for Nanocrystal Purification and On-Column Ligand Exchange Chemistry. *Chemical Science* **2016**, *7* (9), 5671–5679.

(151) Chatzigoulas, A.; Karathanou, K.; Dellis, D.; Cournia, Z. NanoCrystal: A Web-Based Crystallographic Tool for the Construction of Nanoparticles Based on Their Crystal Habit. *Journal of Chemical Information and Modeling* **2018**, *58* (12), 2380–2386.

(152) Garrity, K. F.; Bennett, J. W.; Rabe, K. M.; Vanderbilt, D. Pseudopotentials for High-Throughput DFT Calculations. *Computational Materials Science* **2014**, *81*, 446–452.

(153) Prandini, G.; Marrazzo, A.; Castelli, I. E.; Mounet, N.; Marzari, N. Precision and Efficiency in Solid-State Pseudopotential Calculations. *npj Comput Mater* **2018**, *4* (1), 1–13.

(154) Giannozzi, P.; Baroni, S.; Bonini, N.; Calandra, M.; Car, R.; Cavazzoni, C.; Ceresoli, D.; Chiarotti, G. L.; Cococcioni, M.; Dabo, I.; Dal Corso, A.; de Gironcoli, S.; Fabris, S.; Fratesi, G.; Gebauer, R.; Gerstmann, U.; Gougoussis, C.; Kokalj, A.; Lazzeri, M.; Martin-Samos, L.; Marzari, N.; Mauri, F.; Mazzarello, R.; Paolini, S.; Pasquarello, A.; Paulatto, L.; Sbraccia, C.; Scandolo, S.; Sclauzero, G.; Seitsonen, A. P.; Smogunov, A.; Umari, P.; Wentzcovitch, R. M. QUANTUM ESPRESSO: A Modular and Open-Source Software Project for Quantum Simulations of Materials. *J. Phys.: Condens. Matter* **2009**, *21* (39), 395502.

(155) Bowden, M. E.; Cardile, C. M. Structures of Orthorhombic and Cubic Dicadmium Stannate by Rietveld Refinement. *Powder Diffr.* **1990**, *5* (1), 36–40.

(156) Hinuma, Y.; Pizzi, G.; Kumagai, Y.; Oba, F.; Tanaka, I. Band Structure Diagram Paths Based on Crystallography. *Computational Materials Science* **2017**, *128*, 140–184.

(157) Monkhorst, H. J.; Pack, J. D. Special Points for Brillouin-Zone Integrations. *Phys. Rev. B* **1976**, *13* (12), 5188–5192.

(158) Tang, M.; Shang, J.; Zhang, Y. Density Functional Theory Analysis of Electronic Structure and Optical Properties of La Doped Cd_2SnO_4 Transparent Conducting Oxide. *Chinese Phys. B* **2018**, *27* (1), 017101.

(159) Pines, A.; Gibby, M. G.; Waugh, J. S. Proton-enhanced NMR of Dilute Spins in Solids. *The Journal of Chemical Physics* **2003**, *59* (2), 569–590.

(160) Siegel, R.; Nakashima, T. T.; Wasylishen, R. E. Signal-to-Noise Enhancement of NMR Spectra of Solids Using Multiple-Pulse Spin-Echo Experiments. *Concepts in Magnetic Resonance Part A* **2005**, *26A* (2), 62–77.

(161) Hung, I.; Rossini, A. J.; Schurko, R. W. Application of the Carr−Purcell Meiboom−Gill Pulse Sequence for the Acquisition of Solid-State NMR Spectra of Spin-1/2 Nuclei. *J. Phys. Chem. A* **2004**, *108* (34), 7112–7120.

(162) Mishra, R. K.; Thomas, G. Surface Energy of Spinel. *Journal of Applied Physics* **1977**, *48* (11), 4576–4580.

(163) Meng, T.; McCandless, B.; Buchanan, W.; Kimberly, E.; Birkmire, R. Cadmium Tin Oxide Thin Films Deposited by RF Magnetron Sputtering for Photovoltaic Applications. *Journal of Alloys and Compounds* **2013**, *556*, 39–44.

(164) Kim, D. Y.; Li, W.; Ma, Y.; Yu, T.; Li, Z. Y.; Park, O. O.; Xia, Y. Seed-Mediated Synthesis of Gold Octahedra in High Purity and with Well-Controlled Sizes and Optical Properties. *Chemistry - A European Journal* **2011**, *17* (17), 4759–4764.

(165) Agrawal, A.; Kriegel, I.; Milliron, D. J. Shape-Dependent Field Enhancement and Plasmon Resonance of Oxide Nanocrystals. *Journal of Physical Chemistry C* **2015**, *119* (11), 6227–6238.

(166) Lounis, S. D.; Runnerstrom, E. L.; Bergerud, A.; Nordlund, D.; Milliron, D. J. Influence of Dopant Distribution on the Plasmonic Properties of Indium Tin Oxide Nanocrystals. *J. Am. Chem. Soc.* **2014**, *136* (19), 7110–7116.

(167) Ghosh, S.; Saha, M.; Paul, S.; De, S. K. Shape Controlled Plasmonic Sn Doped CdO Colloidal Nanocrystals: A Synthetic Route to Maximize the Figure of Merit of Transparent Conducting Oxide. *Small* **2017**, *13* (7), 1602469.

(168) Staller, C. M.; Gibbs, S. L.; Saez Cabezas, C. A.; Milliron, D. J. Quantitative Analysis of Extinction Coefficients of Tin-Doped Indium Oxide Nanocrystal Ensembles. *Nano Lett.* **2019**, *19* (11), 8149–8154.

(169) Zandi, O.; Agrawal, A.; Shearer, A. B.; Reimnitz, L. C.; Dahlman, C. J.; Staller, C. M.; Milliron, D. J. Impacts of Surface Depletion on the Plasmonic Properties of Doped Semiconductor Nanocrystals. *Nature Materials* **2018**, *17* (8), 710–717.

(170) Shubert-Zuleta, S. A.; Tandon, B.; Roman, B. J.; Gan, X. Y.; Milliron, D. J. How to Quantify Electrons in Plasmonic Colloidal Metal Oxide Nanocrystals. *Chem. Mater.* **2023**, *35* (10), 3880–3891.

(171) Pineider, F.; Campo, G.; Bonanni, V.; Fernández, C. D. J.; Mattei, G.; Caneschi, A.; Gatteschi, D.; Sangregorio, C. Circular Magnetoplasmonic Modes in Gold Nanoparticles. *Nano Letters* **2013**, *13* (10), 4785–4789.

(172) Hartstein, K. H.; Schimpf, A. M.; Salvador, M.; Gamelin, D. R. Cyclotron Splittings in the Plasmon Resonances of Electronically Doped Semiconductor Nanocrystals Probed by Magnetic Circular Dichroism Spectroscopy. *J. Phys. Chem. Lett.* **2017**, *8* (8), 1831–1836.

(173) Han, B.; Gao, X.; Lv, J.; Tang, Z. Magnetic Circular Dichroism in Nanomaterials: New Opportunity in Understanding and Modulation of Excitonic and Plasmonic Resonances. *Advanced Materials* **2020**, *32* (41), 1801491.

(174) Yin, P.; Chen, S.; Radovanovic, P. V. Properties of Free Charge Carriers Govern Exciton Polarization in Plasmonic Semiconductor Nanocrystals. *J. Phys. Chem. Lett.* **2022**, *13* (24), 5545–5552.

(175) Tandon, B.; Radovanovic, P. V. Size Control of the Mechanism of Exciton Polarization in Metal Oxide Nanocrystals through Fermi Level Pinning. *ACS Nano* **2023**, *17* (14), 14069–14078.

(176) Jayaram, P.; Jaya, T. P.; Prasanth, K.; Abdul Gafoor, A. K.; Pradyumnan, P. P. Structural, Electrical and Surface Morphological Studies of Cd_2SnO_4 and Mg Doped Cd_2SnO_4 Thin Films. *Trans Indian Inst Met* **2011**, *64* (1–2), 221–225.

(177) El-Nahass, M. M.; Atta, A. A.; Abd El-Raheem, M. M.; Hassanien, A. M. Structural and Optical Properties of DC Sputtered Cd2SnO 4 Nanocrystalline Films. *Journal of Alloys and Compounds* **2014**, *585*, 1–6.

(178) Wei, S.-H.; Segev, D. Electronic and Optical Properties of Spinel TCOs: $SnZn_2O_4$, $SnCd_2O_4$, and $CdIn_2O_4$. **2004**.

(179) Barrows, C. J.; Vlaskin, V. A.; Gamelin, D. R. Absorption and Magnetic Circular Dichroism Analyses of Giant Zeeman Splittings in Diffusion-Doped Colloidal $Cd_{1-x}Mn_xSe$ Quantum Dots. *J. Phys. Chem. Lett.* **2015**, *6* (15), 3076–3081.

(180) Kolahi, S.; Farjami-Shayesteh, S.; Azizian-Kalandaragh, Y. Comparative Studies on Energy-Dependence of Reduced Effective Mass in Quantum Confined ZnS Semiconductor Nanocrystals Prepared in Polymer Matrix. *Materials Science in Semiconductor Processing* **2011**, *14* (3–4), 294–301.

(181) Gibbs, S. L.; Staller, C. M.; Agrawal, A.; Johns, R. W.; Cabezas, C. A. S.; Milliron, D. J. Intrinsic Optical and Electronic Properties from Quantitative Analysis of Plasmonic Semiconductor Nanocrystal Ensemble Optical Extinction. *J. Phys. Chem. C* **2020**.

(182) Berrettini, M. G.; Braun, G.; Hu, J. G.; Strouse, G. F. NMR Analysis of Surfaces and Interfaces in 2-nm CdSe. *Journal of the American Chemical Society* **2004**, *126* (22), 7063–7070.

(183) Kittel, C. *Introduction to Solid State Physics*, 8th ed.; Wiley: Hoboken, NJ, 2005.

(184) Li, Q.; Sui, L.; Niu, G.; Jiang, J.; Zhang, Y.; Che, L.; Wu, G.; Jin, M.; Yuan, K. Ultrafast Optical Switching to a Metallic State via Photoinduced Mott Transition in Few-Layer MoS_2 under Hydrostatic Pressure. *PHYSICAL REVIEW B* **2021**.

(185) Townes, C. H.; Herring, C.; Knight, W. D. The Effect of Electronic Paramagnetism on Nuclear Magnetic Resonance Frequencies in Metals. *Phys. Rev.* **1950**, *77* (6), 852–853.

(186) Alexander, M. N.; Holcomb, D. F. Semiconductor-to-Metal Transition in n -Type Group IV Semiconductors. *Rev. Mod. Phys.* **1968**, *40* (4), 815–829.

(187) Marbella, L. E.; Gan, X. Y.; Kaseman, D. C.; Millstone, J. E. Correlating Carrier Density and Emergent Plasmonic Features in $Cu_{2-x}Se$ Nanoparticles. *Nano Lett.* **2017**, *17* (4), 2414–2419.

(188) Cardile, C. M.; Meinhold, R. H.; MacKenzie, K. J. D. The Properties of Cadmium Stannates Investigated by EPR and High-Resolution Solid-State ^{113}Cd NMR Spectroscopy. *Journal of Physics and Chemistry of Solids* **1987**, *48* (10), 881–885.

(189) Sundfors, R. K.; Holcomb, D. F. Nuclear Magnetic Resonance Studies of the Metallic Transition in Doped Silicon. *Phys. Rev.* **1964**, *136* (3A), A810–A820.

(190) Meintjes, E. M.; Warren, W. W.; Yesinowski, J. P. Temperature-Dependent ^{29}Si NMR Resonance Shifts in Lightly- and Heavily-Doped Si:P. *Solid State Nuclear Magnetic Resonance* **2013**, *55–56*, 91–94.

(191) Leloup, J. Y.; Sapoval, B.; Martinez, G. Knight Shift in Multivalley Semiconductors. II. Determination of the Hyperfine Coupling Constants in N -and P -Type PbSe and PbTe. *Phys. Rev. B* **1973**, *7* (12), 5276–5284.

(192) Lee, K.; Liesegang, J.; Phipps, P. B. P. Pb 207 Nuclear Magnetic Resonance in PbSe. *Phys. Rev.* **1967**, *161* (2), 322–329.

(193) Lovingood, D. D.; Achey, R.; Paravastu, A. K.; Strouse, G. F. Size- and Site-Dependent Reconstruction in CdSe QDs Evidenced by $^{77}Se\{^{1}H\}$ CP-MAS NMR Spectroscopy. *J. Am. Chem. Soc.* **2010**, *132* (10), 3344–3354.

(194) Lovingood, D. D.; Oyler, R. E.; Strouse, G. F. Composition Control and Localization of S^{2-} in CdSSe Quantum Dots Grown from $Li_4[Cd_{10}Se_4(SPh)_{16}]$. *J. Am. Chem. Soc.* **2008**, *130* (50), 17004–17011.

(195) Honkonen, R. S.; Doty, F. D.; Ellis, P. D. Cadmium-113 Shielding Tensors of Cadmium-Oxo Compounds. 1. Single-Crystal Studies on $Cd(NO_3)_2$-$4H_2O$ and $3CdSO_4$ $8H_2O$.

(196) Ratcliffe, C. I.; Yu, K.; Ripmeester, J. A.; Badruz Zaman, Md.; Badarau, C.; Singh, S. Solid State NMR Studies of Photoluminescent Cadmium Chalcogenide Nanoparticles. *Phys. Chem. Chem. Phys.* **2006**, *8* (30), 3510.

(197) Duncan T., Michael. *A Compilation of Chemical Shift Anisotropies*; Farragut Press, 1990.

(198) Schlaak, M.; Weiss, A. Knight Shift in CdO. *Solid State Communications* **1970**, *8* (15), 1241–1243.

(199) Rees, G. J.; Orr, S. T.; Barrett, L. O.; Fisher, J. M.; Houghton, J.; Spikes, G. H.; Theobald, B. R. C.; Thompsett, D.; Smith, M. E.; Hanna, J. V. Characterisation of Platinum-Based Fuel Cell Catalyst Materials Using ^{195}Pt Wideline Solid State NMR. *Phys. Chem. Chem. Phys.* **2013**, *15* (40), 17195.

(200) Gibbs, S. L.; Staller, C. M.; Milliron, D. J. Surface Depletion Layers in Plasmonic Metal Oxide Nanocrystals. *Acc. Chem. Res.* **2019**, *52* (9), 2516–2524.

(201) Cossement, C.; Darville, J.; Gilles, J. -M; Nagy, J. B.; Fernandez, C.; Amoureux, J. -P. Chemical Shift Anisotropy and Indirect Coupling in SnO_2 and SnO. *Magnetic Resonance in Chemistry* **1992**, *30* (3), 263–270.

(202) Batool, J.; Alay-e-Abbas, S. M.; Amin, N. Thermodynamic, Electronic, and Magnetic Properties of Intrinsic Vacancy Defects in Antiperovskite Ca_3SnO. *Journal of Applied Physics* **2018**, *123* (16), 161516.

(203) Yu, L.; Zunger, A. A Polarity-Induced Defect Mechanism for Conductivity and Magnetism at Polar–Nonpolar Oxide Interfaces. *Nat Commun* **2014**, *5* (1), 5118.

(204) Muñoz-García, A. B.; Pavone, M.; Carter, E. A. Effect of Antisite Defects on the Formation of Oxygen Vacancies in Sr_2FeMoO_6 : Implications for Ion and Electron Transport. *Chem. Mater.* **2011**, *23* (20), 4525–4536.

(205) Wang, Z.; Wang, L. Role of Oxygen Vacancy in Metal Oxide Based Photoelectrochemical Water Splitting. *EcoMat* **2021**, *3* (1), e12075.

(206) Gunkel, F.; Christensen, D. V.; Chen, Y. Z.; Pryds, N. Oxygen Vacancies: The (in)Visible Friend of Oxide Electronics. *Applied Physics Letters* **2020**, *116* (12), 120505.

(207) Zhang, L.; Chu, W.; Zheng, Q.; Zhao, J. Effects of Oxygen Vacancies on the Photoexcited Carrier Lifetime in Rutile TiO_2. *Phys. Chem. Chem. Phys.* **2022**, *24* (8), 4743–4750.

(208) Liu, L.; Mei, Z.; Tang, A.; Azarov, A.; Kuznetsov, A.; Xue, Q.-K.; Du, X. Oxygen Vacancies: The Origin of n -Type Conductivity in ZnO. *Phys. Rev. B* **2016**, *93* (23), 235305.

(209) Wang, Q.; Puntambekar, A.; Chakrapani, V. Vacancy-Induced Semiconductor–Insulator–Metal Transitions in Nonstoichiometric Nickel and Tungsten Oxides. *Nano Lett.* **2016**, *16* (11), 7067–7077.

(210) Kuszynski, J. E.; Kays, J. C.; Conti, C. R.; McGill, S. A.; Dennis, A. M.; Strouse, G. F. Effective Mass for Holes in Paramagnetic, Plasmonic Cu_5FeS_4 Semiconductor Nanocrystals. *J. Phys. Chem. C* **2022**, *126* (30), 12669–12679.

(211) Pineider, F.; Campo, G.; Bonanni, V.; de Julián Fernández, C.; Mattei, G.; Caneschi, A.; Gatteschi, D.; Sangregorio, C. Circular Magnetoplasmonic Modes in Gold Nanoparticles. *Nano Lett.* **2013**, *13* (10), 4785–4789.

(212) Kuszynski, J. E.; Fabiano, C. J.; Nguyen, E. T.; Mao, K.; Ahuja, A. K.; Schaller, R. D.; Strouse, G. F. Plasmon-Induced Hot-Carrier Excited-State Dynamics in Plasmonic Semiconductor Nanocrystals. *J. Phys. Chem. C* **2023**, acs.jpcc.3c05208.

(213) Kuszynski, J. E.; Zhong, X.; Fabiano, C. J.; Dennis, A. M.; Strouse, G. F. Hot Hole Kinetics of Bornite Plasmonic Semiconductor Nanocrystals. *publication in progress*.

(214) Jefferson, P. H.; Hatfield, S. A.; Veal, T. D.; King, P. D. C.; McConville, C. F.; Zúñiga–Pérez, J.; Muñoz–Sanjosé, V. Bandgap and Effective Mass of Epitaxial Cadmium Oxide. *Applied Physics Letters* **2008**, *92* (2), 022101.

(215) Mulligan, W. P.; Coutts, T. J. Measurement of the Effective Mass of Transparent Conducting Films of Cadmium Tin Oxide. *Materials Research Society Symposium - Proceedings* **1997**, *471* (1), 117–122.

(216) Ye, X.; Fei, J.; Diroll, B. T.; Paik, T.; Murray, C. B. Expanding the Spectral Tunability of Plasmonic Resonances in Doped Metal-Oxide Nanocrystals through Cooperative Cation–Anion Codoping. *J. Am. Chem. Soc.* **2014**, *136* (33), 11680–11686.

(217) Ghosh, S.; Saha, M.; Paul, S.; De, S. K. Shape Controlled Plasmonic Sn Doped CdO Colloidal Nanocrystals: A Synthetic Route to Maximize the Figure of Merit of Transparent Conducting Oxide. *Small* **2017**, *13* (7), 1602469.

(218) Su, Z.; Yang, W.; Wang, C.; Xiong, S.; Cao, X.; Peng, Y.; Si, W.; Weng, Y.; Xue, M.; Li, J. Roles of Oxygen Vacancies in the Bulk and Surface of CeO_2 for Toluene Catalytic Combustion. *Environ. Sci. Technol.* **2020**, *54* (19), 12684–12692.

(219) Torbrügge, S.; Reichling, M.; Ishiyama, A.; Morita, S.; Custance, Ó. Evidence of Subsurface Oxygen Vacancy Ordering on Reduced CeO_2 (111). *Phys. Rev. Lett.* **2007**, *99* (5), 056101.

(220) Wang, Z.; Yu, H.; Su, H. The Transport Properties of Oxygen Vacancy-Related Polaron-like Bound State in HfO_x. *Sci Rep* **2013**, *3* (1), 3246.

(221) Ortega, R. E.; Smith, Robert B; Kusynski, J. E.; Bayles, A.; McGill, S. A.; Halas, N. J.; Schurko, R. W.; Strouse, G. F. Observing Metallic Carriers in Highly Faceted Plasmonic Cd_2SnO_4 Inverse Spinel Nanocrystals. *Adv. Optical Mater.* **2024**.

(222) Jain, P. K.; Lee, K. S.; El-Sayed, I. H.; El-Sayed, M. A. Calculated Absorption and Scattering Properties of Gold Nanoparticles of Different Size, Shape, and Composition: Applications in Biological Imaging and Biomedicine. *J. Phys. Chem. B* **2006**, *110* (14), 7238–7248.

(223) Bayles, A.; Fabiano, C. J.; Shi, C.; Yuan, L.; Craft, N.; Jacobson, C.; Dhindsa, P.; Ogundare, A.; Mendez, Y.; Chen, B.; Robatjazi, H.; Han, Y.; Strouse, G. F.; Nordlander, P.; Everitt, H. O.; Halas, N. J. Tailoring the Aluminum Nanocrystal Surface Oxide for All-Aluminum-Based Antenna-Reactor Plasmonic Photocatalysts. *Proc. Natl. Acad. Sci. U.S.A.*

(224) Norberg, N. S.; Gamelin, D. R. Giant Zeeman Effects in Colloidal Diluted Magnetic Semiconductor Quantum Dots with Homogeneous Dopant Speciation. *Journal of Applied Physics* **2006**, *99* (8), 08M104.

(225) Schimpf, A. M.; Ochsenbein, S. T.; Buonsanti, R.; Milliron, D. J.; Gamelin, D. R. Comparison of Extra Electrons in Colloidal N-Type Al^{3+}-Doped and Photochemically Reduced ZnO Nanocrystals. *Chem. Commun.* **2012**, *48* (75), 9352–9354.

(226) Magana, D.; Perera, S. C.; Harter, A. G.; Dalal, N. S.; Strouse, G. F. Switching-on Superparamagnetism in Mn/CdSe Quantum Dots. *J. Am. Chem. Soc.* **2006**, *128* (9), 2931–2939.

(227) Bindra, J. K.; Gutsev, L. G.; Van Tol, J.; Singh, K.; Dalal, N. S.; Strouse, G. F. Experimental Validation of Ferromagnetic–Antiferromagnetic Competition in $Fe_xZn_{1-x}Se$ Quantum Dots by Computational Modeling. *Chem. Mater.* **2018**, *30* (6), 2093–2101.

(228) Diroll, B. T.; Guo, P.; Chang, R. P. H.; Schaller, R. D. Large Transient Optical Modulation of Epsilon-Near-Zero Colloidal Nanocrystals. *ACS Nano* **2016**, *10* (11), 10099–10105.

(229) Lewis, B. G.; Paine, D. C. Applications and Processing of Transparent Conducting Oxides. *MRS Bulletin* **2000**, *25* (8), 22–27.

(230) Anitha, M.; Saravanakumar, K.; Anitha, N.; Kulandaisamy, I.; Amalraj, L. Influence of Annealing Temperature on Physical Properties of Sn-Doped CdO Thin Films by Nebulized Spray Pyrolysis Technique. *Materials Science and Engineering B: Solid-State Materials for Advanced Technology* **2019**, *243* (January), 54–64.

(231) Wu, X. High-Efficiency Polycrystalline CdTe Thin-Film Solar Cells. *Solar Energy* **2004**, *77* (6), 803–814.

(232) Meng, T.; McCandless, B. E.; Buchanan, W. A.; Birkmire, R. W.; Hamilton, C. T.; Aitken, B. G.; Williams, C. A. K. Effect of Annealing Atmosphere and Temperature on the Properties of Cd_2SnO_4 Thin Films. In *2012 38th IEEE Photovoltaic Specialists Conference*; 2012; pp 001803–001806.

(233) Mamazza, R.; Morel, D. L.; Ferekides, C. S. Transparent Conducting Oxide Thin Films of Cd_2SnO_4 Prepared by RF Magnetron Co-Sputtering of the Constituent Binary Oxides. *Thin Solid Films* **2005**, *484* (1–2), 26–33.

(234) Kaviyarasu, K.; Manikandan, E.; Paulraj, P.; Mohamed, S. B.; Kennedy, J. One Dimensional Well-Aligned CdO Nanocrystal by Solvothermal Method. *Journal of Alloys and Compounds* **2014**, *593*, 67–70.

(235) Abd El-Moneim, A.; Azooz, M. A.; Hashem, H. A.; Fayad, A. M.; Elwan, R. L. XRD, FTIR and Ultrasonic Investigations of Cadmium Lead Bismuthate Glasses. *Sci Rep* **2023**, *13* (1), 12788.

(236) Sasikumar, P.; Revathy, M. S.; Nithiyanantham, S. $Cd(OH)_2$ and CdO: Structural, Optical, Electron Density Distribution Analysis with Antibacterial Assay. *Eur. Phys. J. Plus* **2022**, *137* (3), 294.

(237) Akram, M.; Saleh, A. T.; Ibrahim, W. A. W.; Awan, A. S.; Hussain, R. Continuous Microwave Flow Synthesis (CMFS) of Nano-Sized Tin Oxide: Effect of Precursor Concentration. *Ceramics International* **2016**, *42* (7), 8613–8619.

(238) Prakash, T.; Arunkumar, T.; Sathya Raj, D.; Jayaprakash, R. Surfactant-Liaised Variation in CdO Nanocomposites Morphology. *Physics Procedia* **2013**, *49*, 36–43.

(239) Meulenberg, R. W.; Strouse, G. F. Chain Packing Analysis of the Passivating Layer on Nanocrystalline Quantum Dot Surfaces. *J. Phys. Chem. B* **2001**, *105* (31), 7438–7445.

(240) Kendall, O.; Wainer, P.; Barrow, S.; van Embden, J.; Della Gaspera, E. Fluorine-Doped Tin Oxide Colloidal Nanocrystals. *Nanomaterials* **2020**, *10* (5).

(241) Makuła, P.; Pacia, M.; Macyk, W. How To Correctly Determine the Band Gap Energy of Modified Semiconductor Photocatalysts Based on UV–Vis Spectra. *J. Phys. Chem. Lett.* **2018**, *9* (23), 6814–6817.

(242) Wohlmuth, W.; Adesida, I. Properties of R.F. Magnetron Sputtered Cadmium–Tin–Oxide and Indium–Tin–Oxide Thin Films. *Thin Solid Films* **2005**, *479* (1), 223–231.

(243) George, S. M. Mechanisms of Thermal Atomic Layer Etching. **2020**.

(244) Li, F.; Moayed, M. M. R.; Gerdes, F.; Kull, S.; Klein, E.; Lesyuk, R.; Klinke, C. Colloidal Tin Sulfide Nanosheets: Formation Mechanism, Ligand-Mediated Shape Tuning and Photo-Detection. *J. Mater. Chem. C* **2018**, *6* (35), 9410–9419.

(245) Lovingood, D. D.; Strouse, G. F. Microwave Induced In-Situ Active Ion Etching of Growing InP Nanocrystals. *Nano Lett.* **2008**, *8* (10), 3394–3397.

(246) Hardy, D. A.; Tigaa, R. A.; Ortega, R. E.; McBride, J. R.; Strouse, G. F. Breaking Latva's Rule by Energy Hopping in a Tb(III):$ZnAl_2O_4$ Nanospinel. *J. Phys. Chem. C* **2019**, *123* (51), 31175–31182.

(247) Lo Faro, M. J.; Leonardi, A. A.; Priolo, F.; Fazio, B.; Miritello, M.; Irrera, A. Erbium Emission in Er:Y_2O_3 Decorated Fractal Arrays of Silicon Nanowires. *Sci Rep* **2020**, *10* (1), 12854.

(248) Sachet, E.; Shelton, C. T.; Harris, J. S.; Gaddy, B. E.; Irving, D. L.; Curtarolo, S.; Donovan, B. F.; Hopkins, P. E.; Sharma, P. A.; Sharma, A. L.; Ihlefeld, J.; Franzen, S.; Maria, J.-P. Dysprosium-Doped Cadmium Oxide as a Gateway Material for Mid-Infrared Plasmonics. *Nature Mater* **2015**, *14* (4), 414–420.

(249) Zhang, J.; Cheng, X.; Zhang, H.; Zheng, J.; Wang, J. Plasmon-Controlled Selective Emission Enhancement of Eu^{3+} with (Au Core)@(Y(V,P)O_4:Eu) Nanostructures. *ACS Nano* **2023**.

(250) He, J.; Zheng, W.; Ligmajer, F.; Chan, C.-F.; Bao, Z.; Wong, K.-L.; Chen, X.; Hao, J.; Dai, J.; Yu, S.-F.; Lei, D. Y. Plasmonic Enhancement and Polarization Dependence of Nonlinear Upconversion Emissions from Single Gold nanorod@SiO2@CaF2:Yb^{3+},Er^{3+} Hybrid Core–Shell–Satellite Nanostructures. *Light Sci Appl* **2017**, *6* (5), e16217–e16217.

(251) Jia, T.; An, J.; Yu, D.; Li, J.; Fu, F.; Wang, K.; Wang, W. Continuously Improved Photocatalytic Performance of Zn_2SnO_4/SnO_2/Cu_2O Composites by Structural Modulation and Band Alignment Modification. *Nanomaterials* **2019**, *9* (10), 1390.

(252) Rovisco, A.; Branquinho, R.; Martins, R.; Fortunato, E.; Barquinha, P. Microwave-Assisted Hydrothermal Synthesis of Zn_2SnO_4 Nanostructures for Photocatalytic Dye Degradation. In *The 2nd International Online-Conference on Nanomaterials*; MDPI, 2021; p 92.

(253) Zhao, Y.; Hu, L.; Liu, H.; Liao, M.; Fang, X.; Wu, L. Band Gap Tunable Zn_2SnO_4 Nanocubes through Thermal Effect and Their Outstanding Ultraviolet Light Photoresponse. *Sci Rep* **2014**, *4* (1), 6847.

BIOGRAPHICAL SKETCH

Education

Florida State University 2018-Present
Tallahassee, FL
Ph.D. Materials Chemistry
Dissertation: Understanding the Evolution of Carries in Tin Cadmium Oxide Ternary Plasmonic Nanocrystals (Defense date: 7/1/2024)
Dissertation Advisor: Professor Geoffrey F. Strouse
M.S. Materials Chemistry 2020
Qualification Exam Title: Tuning Phosphor Emission for Solid-state Lighting by Manipulation of Ln(III) Photophysics
Awards: Selected to host and organize the ACS Spring 2022 Graduate Student symposium Planning Committee (GSSPC) in honor of Dr. Michael Kasha, 2022.
Philip Schlenoff Excellence Award, 2022.

Florida Atlantic University 2015-2017
Boca Raton, FL
B.S. Chemistry 2017
Awards: Summer Undergraduate Research Fellowship (SURF), 2016.

Palm Beach State College 2013-2014
Lake Worth, FL
A.A. General Education 2014
CCC Emergency Medical Technician 2013
Awards: Graduated from the Dr. Floyd F. Koch Honors College with the highest rank.
Certificate of Achievement from the Math and Science Institute at Palm Beach State College.
Awarded most active member of Biology club in 2013.

Experience

Graduate Student Researcher, Ph.D. Candidate **August 2018-Present**
Florida State University – Tallahassee, FL

- Designed, synthesized, and probed the structural and optical properties of luminesce and plasmonic nanomaterials through round bottom and microwave techniques.
- Performed contract work for Samsung through Kirkland & Ellis in US dealing with patent lawsuit for quantum dot patents (NDA signed 2021). Worked under tight deadlines with weekly meetings to law firm providing data and interpretation. Worked involved experimental design, synthesis, characterization, and interpretation.
- Planned and organized the GSSPC at Spring ACS, 2023, celebrating the centenary of Dr. Michael Kasha. Some of the tasks included: Organizing speakers and event schedule, planning budget fund-raising and spending, and managing the event website and social media pages.

- Presented research findings in weekly reports and at peer-refereed conferences.
- Significant experience troubleshooting within group research ranging from day-to-day fixes to experimental design, and to help navigate research projects from fellow graduate student.
- Provided guidance and feedback on experimental design and data analysis for undergraduate students in the research lab through Undergraduate Research Opportunity Program (UROP).

Graduate Student Teaching Assistant **August 2018-December 2022**
Florida State University – Tallahassee, FL

- Courses Taught: Chemistry 1045L, 1046, 2211L, 3217, 3120L, NMR Tech
- Responsibilities were to facilitate discussion and laboratory periods as well as proctor lecture exams. Met with students upon request and graded all quizzes and exams in recitation or discussion. Graded all laboratory reports following a finished experiment.
- Chemistry 1045L – General Chemistry I Lab
- Chemistry 1046 – General Chemistry II
- Chemistry 2211L – Organic Chemistry Lab
- Chemistry 3217 – Organic Chemistry (Combined I & II)
- Chemistry 3120L – Analytical Chemistry Lab: Introduction to Analytical Chemistry
- NMR Tech – Tasks entailed: running hundreds of samples by solution ^{1}H NMR for the organic laboratory every week. Weekly liquid N_2 refills for the NMR instruments in the chemistry department. Troubleshooting common hardware and software errors while operating NMR instruments.

College Tutor **April 2017 – August 2018**
Palm Beach State College – Boca Raton, FL

- Courses Tutored: Chemistry 1045, 1046, 2210, 2211 (with corresponding laboratory components), math courses up to MAC 2311, and all levels of Spanish up to SPN2241.
- Responsibilities: Had one-on-one tutoring sessions with students from different backgrounds and career paths where homework and class problems were critically assessed.
- Chemistry 1045/1046 – General Chemistry I & II
- Chemistry 2210/2211 – Organic Chemistry I & II
- Math 2311 – Calculus with Analytical Geometry
- Spanish 2241 – Intermediate Conversational Spanish II

Undergraduate Student Researcher **May 2016 – December 2017**
Florida Atlantic University – Boca Raton, FL
Advisor – Dr. Daniel T. de. Lill

- Project – Synthesis and Sensing Studies of Erbium MOF based on 2-2'bithiophene-5,5'-dicarboxylic acid
- Details – Utilizing solvothermal methods, a new rare-earth metal organic framework (MOF) was synthesized using erbium as the metal center, and dithiophene dicarboxylate (DTDC) as a ligand. The sensing capabilities of nitroaromatic molecules was explored by utilizing this novel MOF.

Publications

1. **Ortega, R.E.**; J.E.; Fabiano, C.J.; Smith, R.; Schurko, R.; Strouse, G.F. "Defect Evolution in Cd-Sn-O Plasmonic Semiconductor Nanocrystals"; *in preparation*.
2. **Ortega, R.E.**; Kuszynski, J.E.; Strouse, G.F. "Hot carrier Dynamics of Fluorinated Cd_2SnO_4 Nanocrystals"; *in preparation*.
3. Smith, R ; **Ortega, R.E.** ; Schurko, R.; Strouse, G.F. "Investigation of Metallic Carriers in Cd_2SnO_4 Nanocrystals Through ^{113}Cd and ^{119}Sn Solid-state NMR"; *in preparation*.
4. **Ortega, R.E.**; Smith, R.; Kuszynski, J.E.; Bayles, A.; Schurko, R.; Halas, N. J.; Strouse, G.F. "Evidence of Fermi Level Carriers in Highly Faceted Plasmonic Cd_2SnO_4 Inverse Spinel Nanocrystals"; *Adv. Optical Mater.* 2024.**DOI**:10.1002/adom.202400388
5. Tigaa, R.A. ; **Ortega, R.E.**; Xinsong, L.; Strouse, G.F. "A Versatile Tripodal Ligand for Sensitizing Lanthanide (Ln^{III}) Ions and Color Tuning"; Chemistry, 2021, 3(1), 138-145; **DOI**:10.3390/chemistry3010011
6. Hardy, D.A.; Tigaa, R.; McBride, J.; **Ortega, R. E.**; Strouse, G.F. "Breaking Latva's Rule by Energy Hopping in a Tb(III):$ZnAl_2O_4$ Nanospinel"; J. Phys. Chem. C 2019, 123, 51, 31175–31182; **DOI**:10.1021/acs.jpcc.9b08685
7. Hardy, D.A.; Tigaa, R.; McBride, J.; **Ortega, R. E.**; Strouse, G.F.; "Structure–Function Correlation: Engineering High Quantum Yields in Down-Shifting Nanophosphors". J. Am. Chem. Soc. 2019, 141, 51, 20416–20423; **DOI**:10.1021/jacs.9b11045
8. Einkauf, J.; **Ortega, R.E.**; Mathivathanan, L.; de Lill, D.T.; "Nitroaromatic Sensing With a New Lanthanide Coordination Polymer $[Er_2(C_{10}H_4O_4S_2)_3(H_2O)_6]_n$ Assembled by 2,2'-bithiophene-5,5'-dicarboxylate"; New J. Chem. 2017, 41(19), 10929-10934; **DOI**: 10.1039/c7nj01677h

Presentations

Oral Presentations

1. "Investigating Fermi level carriers in highly faceted plasmonic Cd_2SnO_4 inverse spinel nanocrystals". ACS Spring 2024. New Orleans, LA. March 17, 2024.
2. "Design and Investigation of Optical Properties in Cd_2SnO_4 Nanocrystals". Florida State University Department of Chemistry and Biochemistry Fourth Year Presentation. Tallahassee, FL. February 24, 2022.
3. "Tuning phosphor emission for solid-state lighting by manipulation of Ln(III) photophysics" Florida State University Department of Chemistry and Biochemistry Candidacy Examination. Tallahassee, FL. December 11, 2020.
4. "Understanding the Effects of Strain on Ln(III) Luminescence in $ZnAl_2O_4$ Phosphors". Florida State University Department of Chemistry and Biochemistry Second Year Presentation. Tallahassee, FL. January 9, 2020.
5. "Understanding Structure Properties Relationship in Tb(III) $ZnAl_2O_4$ Phosphor "American Chemical Society 71st South Eastern Regional Meeting. Savannah, Georgia. October 23, 2019.
6. "Synthesis, Structure, and Sensing Ability of a New Lanthanide Coordination Polymer Assembled from 2,2'- bithiophene-5,5'-dicarboxilyc acid". Florida Inorganic and Materials Symposium (FIMS). Gainesville, FL. October 2016.

Poster Presentations

1. “Design and Investigation of Optical Properties in Plasmonic Cd_2SnO_4 Nanocrystals”. Kasha Symposium. Bonding Through Chemistry, Spring ACS. March 22, 2022.
2. “Tb(III) as an Optical Probe of Lattice Disorder in Tb(III):$ZnAl_2O_4$ Nanospinels”. 2019 Florida Inorganic and Materials Symposium. Gainesville, FL. October 12, 2019.
3. “Synthesis and Sensing Studies of Erbium MOF Based on 2-2’-bithiophene-5,5’-dicarboxylic acid”. FAU OURI (Office of Undergraduate Research and Inquiry) Undergraduate Research Symposium. March 31st, 2017.
4. “Synthesis and Sensing Studies of an Erbium MOF based on 2,2'-bithiophene-5,5'-dicarboxylic acid”. Summer Undergraduate Research Fellowship (SURF) Summer Retreat, 2016. Boca Raton, FL. August 5, 2016.